

Compact High-Temperature Superconducting magnets for Laser-Plasma Accelerator beam capture and transport

Zur Erlangung des akademischen Grades eines
Doktors der Naturwissenschaften (Dr. rer. nat.)

von der KIT-Fakultät der Physik
des Karlsruher Instituts für Technologie (KIT)

genehmigte
Dissertation

von
M.Sc. Samira Fatehi
aus Teheran (Iran)

Tag der mündlichen Prüfung: 17. 02. 2023
Erste Gutachterin: Prof. Dr. Anke-Susanne Müller
Zweite Gutachterin: Prof. Dr. Tabea Arndt

I declare that I have developed and written the enclosed thesis completely by myself, and have not used sources or means without declaration in the text.

Karlsruhe, 11.01.2023

.....
(Samira Fatehi)

Abstract

Laser-plasma acceleration is a prominent candidate to drive the next-generation compact light sources and free-electron lasers (FELs). Having orders of magnitude larger electrical field gradients than RF cavities-based machines makes plasma accelerators more affordable and compact. To fully exploit the advantages of the novel accelerating technology, novel compact beam optic elements to compensate for large chromatic effects in the beam transport are required. This thesis aims at exploring the potential of designing miniaturized and high-strength, High-Temperature Superconducting (HTS) magnets and beam optics for the transport of the Laser Wakefield accelerated beams in order to match them to the input parameter requirements of given applications, especially to those of a transverse gradient undulator (TGU) light source. The designed transport lines include miniature multiplet/triplet/doublet quadrupole magnets for beam capture and compact combined-function optics for matching and beam transport. Moreover, investigating the key technology of high-temperature superconductivity (HTS) in designing accelerator magnets can lead to the future application of a plasma accelerator as an injector for a compact storage ring. In this thesis, I targeted magnet designs for HTS miniaturized iron and coil-dominated magnets. For a cos-theta coil-based geometry and an iron-based periodic geometry compact, well-controlled, high-energy transport lines have been developed in which the beam properties are matching the geometrical and dynamical acceptance of, e.g., the transverse gradient undulator, TGU. Finally, for the periodic iron-based quadrupole, a prototype using HTS ReBCO tape has been optimized and built in close collaboration with KIT Institute for Technical Physics (ITEP) and Technik-Haus.

Zusammenfassung

Laserplasmabeschleuniger haben das Potential, eine neue Generation kompakter Lichtquellen und Freie-Elektronen-Lasers (FEL) zu ermöglichen. Da die elektrischen Feldgradienten in Plasmabeschleunigern um Größenordnungen größer sind als in Linearbeschleunigern auf der Basis von HF-Resonatoren, sind sie kompakter und potentiell kostengünstiger. Um die Vorteile der neuartigen Beschleunigungstechnologie voll ausschöpfen zu können, sind neuartige kompakte Strahloptiken erforderlich, die große chromatische Effekte beim Strahltransport kompensieren. Ziel dieser Dissertation ist es, miniaturisierte hochtemperatursupraleitende (HTS) Magnete mit hohen Feld- bzw. Multipolstärken für die Laser-Wakefield-beschleuniger Elektronenpakete zu entwerfen, welche am Ende der Transportstrecke die Anforderungen an die Eingangsparameter bestimmter Anwendungen zu erfüllen, insbesondere die einer Transversalgradient-Undulator-Lichtquelle (TGU). Diese Transportlinie umfasst Miniatur-Multiplett/Triplett/Dublett-Quadrupole für den Strahleinfang und kompakte Optiken mit kombinierten Funktionen für die Anpassung und den Strahltransport. Darüber hinaus kann die Erforschung der Schlüsseltechnologie der Hochtemperatur-Supraleitung (HTS) für Beschleunigermagnete neue Möglichkeiten zur Anwendung eines Plasmabeschleunigers als Injektor für einen kompakten Speicherring eröffnen. In dieser Arbeit habe ich mich auf Magnetdesigns für HTS-miniaturisierte Eisen- und spulendominierte Magnete konzentriert. Für eine auf Cos-Theta-Spulen basierende Geometrie und eine auf Eisen basierende periodische Geometrie wurden kompakte, gut kontrollierbare Hochenergie-Transportlinien entwickelt, bei denen die Strahleigenschaften der geometrischen und dynamischen Akzeptanz von beispielsweise dem Transversalgradient-Undulator-Lichtquelle (TGU) entsprechen. Schließlich wurde für den periodischen Quadrupol auf Eisenbasis ein Prototyp unter Verwendung von HTS ReBCO-Tape optimiert und in enger Zusammenarbeit mit dem KIT-Institut für Technische Physik (ITEP) und dem Technik-Haus gebaut.

Acknowledgments

Herewith I would like to express my gratitude to all the people who supported me during these years of doing my Ph.D. thesis in spite of the difficult situation due to the COVID-19 crisis and closures.

My special thanks to my supervisor Prof. Dr. Anke-Susanne Müller who gave me a chance to follow up on my interest in a highly prestigious academical environment. I am so grateful to Dr. Erik Bründermann, head of the department of accelerator research and development, for his continued support and encouragement and to Dr. Axel Bernhard, who leads the advanced accelerator concepts group and created an informative, friendly environment. I learned a lot from him and I am thankful for his technical support and his wise hints that always sped up the work.

Also, I am so grateful to Prof. Dr. Tabea Arndt for the very fruitful discussions we had during the fabrication of the HTS demonstrator and also for proofreading my thesis on short notice.

I'd also like to thank my colleagues Dr. Christina Widmann and Dr. Julian Gethmann for their help and hints in different aspects of the work which ease my adjusting to the new work environment and dealing with the new tasks, especially in the first year.

I really appreciate having the help of my colleagues Mr. Sebastian Richter, Dr. Andreas Grau, and Ms. Maisui Ning during the coil winding, powering, and magnetic measurement of the HTS coil demonstrator. Thanks to them for sharing their knowledge and time with me!

Many thanks go to my former colleagues Ms. Nafise Khosravi from the Iranian Light Source Facility (ILSF) and Ms. Mina Akhyani from École Polytechnique Federale de Lausanne (EPFL) for the constructive discussions on the beam dynamics concepts.

Moreover, I appreciate the support and advice of my former technical supervisors, Prof. Dr. Dieter Einfeld, Prof. Dr. Helmut Wiedemann, and P. Eng. Reza Aslani, which were a great motivation for me to do a Ph.D. in accelerator physics.

Last but not the least, I heartily appreciate the support and love that I continuously received from my family specially my parents, my beloved husband Satar, and my son Aryan. Words cannot express how much they mean to me, they have my deepest thanks.

.....To my son Aryan.....

Contents

Abstract	iii
Zusammenfassung	v
Acknowledgments	vii
1. Introduction	1
2. Fundamentals	5
2.1. Motion of charged particles in electromagnetic fields	5
2.1.1. Equation of motion	6
2.1.2. Phase-space and Twiss parameters	9
2.2. Iron-core magnets	12
2.2.1. Multipole Fields	14
2.2.2. Dipoles	16
2.2.3. Quadrupoles	18
2.2.4. Sextupoles	21
2.2.5. Combined-function magnets	22
2.2.6. Magnetic length	25
2.2.7. Principles of magnet design	26
2.3. Air-core magnets	29
2.3.1. Dipoles	32
2.3.2. Quadrupoles	35
2.4. Magnetic measurement	37
2.4.1. Hall probe	38
2.5. Superconductivity in magnets	40
2.5.1. Superconductors Type I and Type II	41
2.5.2. Low-temperature and high-temperature supercon- ductors	42
2.6. Laser Plasma Acceleration	49

3. HTS air-core transport line	53
3.1. Beam dynamics	54
3.1.1. Parameters and requirements	54
3.1.2. Layout and simulation results	55
3.1.3. Particle-tracking	60
3.2. Magnet design	63
3.2.1. Quadrupole design	64
3.2.2. Combined dipole design	72
3.3. Force calculation	78
4. HTS iron-core transport line	83
4.1. Periodic quadrupole	85
4.1.1. Magnet design	85
4.2. Transport line	93
4.2.1. Magnets design	96
4.3. Demonstrator fabrication	101
4.3.1. Winding body	101
4.3.2. Electrical parameters	104
4.3.3. Force calculation	105
4.3.4. Coil winding	107
4.3.5. Powering of the coils	110
4.3.6. Magnetic measurements	113
5. Fixed field alternating gradient transport line	119
6. Summary	127
Bibliography	131
List of figures	149
List of tables	152
List of Abbreviations	153
A. Appendix	155
B. Conference and publications	167

C. Supervised Master Thesis	169
------------------------------------	------------

1. Introduction

Today, particles are accelerated to a speed close to the speed of light and with energies up to trillion electron volts in small and large particle accelerators. The dimensions of these accelerators range from a meter to kilometers while aiming at solving the most complex issues from fundamental particle physics to medical, industrial, environmental, and nanotechnology applications. RF-based accelerators with dimensions of several kilometers come with construction costs of billions of dollars while still suffering limitations like electrical breakdowns or, respectively, quenches in the cavities to produce high-intensity RF waves. Due to these limitations, the maximum acceleration gradient is restricted to less than 100 MeV m^{-1} . In recent years, to overcome these limitations and pursue the goal of having compact, lab-scaled accelerators, alternative acceleration methods have been explored. In fact, the lab-scaled ultra-compact accelerators give this chance to use the accelerator technology more often and easier in exploring materials and life science. One of these novel accelerating methods is particle acceleration using plasma; because plasma is an ionized medium capable of generating and handling electric field gradients up to 100 GeV m^{-1} by charge separation in a plasma wave, which is at least 3 orders of magnitude larger than in conventional accelerators. The plasma wave producing such a strong electric field can be excited using various methods which for more information one can refer to [1, 2, 3, 4], and Section 2.6.

In these small but efficient accelerators, using high power Terawatt (TW) laser pulses with femtosecond (fs) pulse length, plasma waves with high amplitude are excited with a phase speed close to the speed of light. The separation of the positive and negative charges in the plasma wave causes strong electric fields and using this electric field, an injected electron can be accelerated to very high energies of the order of GeV in cm scales. Moreover, laser-plasma accelerators (LPA) can generate ultra-short electron bunches with micrometer bunch lengths leading to high peak currents. This makes

LPAs attractive to be used as drivers for a compact radiation source or even free-electron lasers (FELs) [5]. However, one of the major disadvantages of the LPA technology compared to conventional accelerators is the broad energy distribution of the accelerated electrons with a few percent energy spread, which is decreased to less than 1% in recent years, and milliradians divergence which is orders of magnitude higher than in conventional accelerators and makes it difficult to shape and transport the LPA bunches. To overcome these difficulties and capture divergent, large-energy spread beams efficiently an effective beam transport line is required which in combination with a transverse gradient undulator (TGU) as the radiation source can generate narrow bandwidth radiation despite the high energy spread. The TGU is designed such that the electron beam entering the undulator meets a magnetic field with a gradient in the transverse direction. Electrons with different energies travel through the TGU at different transverse positions and encounter different field amplitudes. Therefore the TGU generates a narrow bandwidth radiation spectrum in spite of a relatively large energy spread of the LPA electron bunches, [6]. Using the TGU as the radiation source, different transport lines with different lengths at different energies have so far been designed and developed at KIT, like a 2.5-meter normal conducting transport line at an energy of 120 MeV designed by Christina Widmann [7] as well as an upgrade to this transport line which has the same 2.5 m length but works at 300 MeV by applying high strength magnets, [8]. The scope of this thesis was the development of reliable transport lines employing miniature magnets with high-strength magnetic fields based on high-temperature superconductor (HTS) technology. These transport lines connect the LPA electron source, like the one at the JETI laser facility at the University of Jena, and a radiation source like the TGU. The magnets' field strengths and layouts are in a way to match the beam optics parameters to the requirements of a given application, especially those of a TGU light source. In this thesis, an air-core and an iron-core transport line are proposed and in addition to the beam dynamics simulations, all magnets for these two beam transport lines were designed. These magnets are based on HTS-coated conductor coils and due to the brittle structure of these conductors, especially in case of having miniature sizes and small bending radii, minimizing stress and strains on the coils while designing the magnets is taken into account. This thesis is structured as follows:

Chapter 2 presents an overview of the fundamental theories and concepts of beam dynamics, iron-core and coil-dominated magnets, and their design principles. Also, an introduction to laser wakefield acceleration, superconductivity, and especially high-temperature superconductor ReBCO coated conductors are given in chapter 2.

In Chapter 3 the design of a 1.4 m beam transport line using air-core, miniature HTS magnets is presented. This transport line guides and controls the LPA electrons at an energy of 700 MeV while fulfilling transverse gradient undulator input parameters. This chapter closes with a detailed discussion of the magnets' design and calculation of the electromagnetic forces inserted on the cos-theta coils wound by HTS tapes.

In Chapter 4 the magnet design as well as the manufacture and test of a demonstrator of an iron-core miniature HTS quadrupole multiplet is discussed. This magnet has a periodic structure and features a simple winding scheme that is capable of providing sufficiently high field gradients to enable highly compact beam transport lines. A 1.4 m iron-core transport line at 260 MeV for this periodic quadrupole is presented in which this periodic quadrupole multiplet is substituted with the common doublet/triplet section of the beam line. Chapter 5 gives a review of Fixed Field Alternating Gradient (FFAG) accelerators as well as the first ideas for adopting FFAG optics concepts for LPA electron beams.

Finally, the summary is given in chapter 6.

2. Fundamentals

2.1. Motion of charged particles in electromagnetic fields

In particle accelerators, we employ the Lorentz force to formulate the charged particle dynamics in presence of electric and magnetic fields which are used for beam acceleration and beam guidance/focusing. The Lorentz force has two components, accounting for the interaction of the charged particle with the electric and the magnetic field

$$\vec{F}_L = q(\vec{E} + \vec{v} \times \vec{B}), \quad (2.1)$$

where q and v are particle charge and velocity and E and B are the electrical and magnetic field strengths, respectively. If we integrate the Lorentz force along the particle trajectory, ds , we can see that no work can be done by the magnetic field.

$$\Delta E_{kin} = \int q(\vec{E} + \vec{v} \times \vec{B})d\vec{s} = \int (q\vec{E}d\vec{s} + q(\vec{v} \times \vec{B})\vec{v}dt) = \int qEds \quad (2.2)$$

So magnetic fields can not change the particle energy and therefore we use electric fields for that purpose but for beam guidance both fields work. Now we come to the question of which field to use to guide the particle beam and why we use magnets in particle accelerators while electric fields are cheaper to generate. To do a comparison we may consider the relation:

$$E = vB \Big|_{v=c, B=1\text{T}} = 3 \times 10^8 \text{ V m}^{-1}. \quad (2.3)$$

For non-relativistic particles, electric fields are easier and cheaper to generate, but for relativistic particles, a magnetic field of 1 T corresponds to an electric field of 300 MV m^{-1} . So magnetic fields are the practical choice for relativistic particles. If a charged particle travels along a circular arc with radius ρ in a uniform magnetic field, according to Newton's 3rd law

the Lorentz force, F_L , is equal to the centripetal force, F_c , and for electrons/protons one can write

$$\frac{\gamma m v^2}{\rho} = e v B, \quad \frac{1}{\rho} = \frac{e B}{\gamma m \beta c} = \frac{e B c}{\gamma m \beta c^2} = \frac{e B c}{\beta E}, \quad (2.4)$$

$$\frac{1}{\rho} = 0.29956 \frac{B \text{ (T)}}{\beta E \text{ (GeV)}} \iff B \rho \text{ (Tm)} = 3.33 \beta E \text{ (GeV)}.$$

In Eq. 2.4, ρ is the radius of curvature, Larmor radius, E is the particle energy, m is the particle mass, e is the electron charge, c is the light velocity, β is the fraction of light speed at which particle moves $\beta = v/c$, $B\rho$ is the beam rigidity and γ is the Lorentz factor and is defined as,

$$\gamma = \frac{1}{\sqrt{1 - \beta^2}}. \quad (2.5)$$

This is a measure of particle energy (momentum) and expresses that particles with higher momentum are more resistant to being deflected by a magnetic field.

For a uniform field of arc length L_m , the deflection angle can be written as $\varphi = L_m/\rho$. For relativistic particles with $\beta \approx 1$, Eq. 2.4 is further simplified and can be written as,

$$\frac{1}{\rho} = \frac{\varphi}{L_{mag}} = 0.29956 \frac{B(\text{T})}{E(\text{GeV})} \quad (2.6)$$

In Beam dynamics, we are interested in particle movements and deviations with respect to the ideal path. The most appropriate coordinate system is, therefore, the one that moves along the ideal path with the origin of the coordinate moving with the reference particle, as shown in Fig. 2.1. In the above figure, x is the horizontal direction, y is the vertical direction and s is the direction along the beam path. The definitions and argumentation in this section and Section 2.1.1 are mainly following the presentation by H. Wiedemann [9].

2.1.1. Equation of motion

As it was discussed in the previous section, we use magnetic fields to guide and keep the particle beam on the desired orbit. The reference trajectory consists of straight and curved parts in which the curvatures are functions

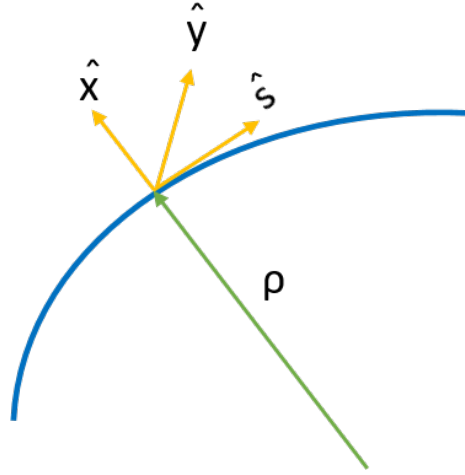


Figure 2.1.: Curvilinear coordinate system of beam dynamics.

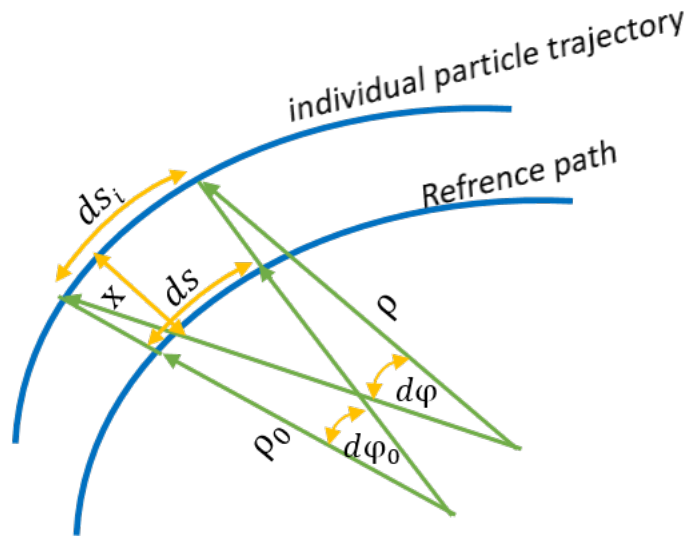


Figure 2.2.: Particle trajectories, reference path s and individual particle trajectory s_i with different bending radii.

of the coordinate s and are nonzero only where there is a constant field of a dipole magnet. To derive the equations of motion, by looking to Fig. 2.2 for the horizontal deflection we have,

$$\begin{aligned}
 ds_i &= \rho d\varphi = (\rho_0 + x)d\varphi_0, \quad ds = \rho_0 d\varphi_0 \\
 ds_i &= \left(1 + \frac{x}{\rho_0}\right) ds
 \end{aligned}
 \tag{2.7}$$

x is the deviation of an individual particle from the ideal path, and φ and φ_0 are the deflection angles for the individual and reference particles, respectively. Then for the second derivative of x with respect to s , we can write

$$\begin{aligned} x'' &= -\left(\frac{d\varphi}{ds} - \frac{d\varphi_0}{ds}\right) = \left(\frac{d\varphi}{ds_i} \frac{ds_i}{ds} - \frac{d\varphi_0}{ds}\right) \\ x'' &= -\frac{1}{\rho} \left(1 + \frac{1}{\rho_0} x\right) + \frac{1}{\rho_0} \end{aligned} \quad (2.8)$$

Also, this horizontal deflection caused by a vertical field can be written in terms of the field higher order multipoles, especially the three lowest ones, dipolar field B_{y0} , quadrupolar field gx , and sextupolar field $1/2sx^2$ (for more details on this multipole fields see Section 2.2.1)

$$\frac{1}{\rho} = \frac{e}{p} B_y = \frac{e}{p} [B_{y0} + gx + \frac{1}{2}sx^2 + \dots] \quad (2.9)$$

In real cases with momentum dispersion, δ , we have,

$$\frac{1}{p} = \frac{1}{p_0(1 + \delta)} = \frac{1}{p_0} [1 - \delta + \delta^2 + \dots] \quad (2.10)$$

where p and p_0 are individual and reference particle momentum, respectively. By inserting Eq. 2.10) into Eq. (2.9),

$$\begin{aligned} \frac{1}{\rho} &= \frac{1}{(1 + \delta)} \left[\frac{1}{\rho_0} + kx + \frac{1}{2}mx^2 + \dots \right] \\ &= \left[\frac{1}{\rho_0} - \frac{1}{\rho_0}\delta + \frac{1}{\rho_0}\delta^2 + kx - kx\delta + \frac{1}{2}mx^2 + \dots \right], \end{aligned} \quad (2.11)$$

we have

$$\begin{aligned} x'' &= -\left[\frac{1}{\rho_0} - \frac{1}{\rho_0}\delta + \frac{1}{\rho_0}\delta^2 + kx - kx\delta + \frac{1}{2}mx^2 + \dots \right] \left(1 + \frac{1}{\rho_0}x\right) + \frac{1}{\rho_0} \\ &= -\frac{1}{\rho_0} - \frac{1}{\rho_0^2}x + \frac{1}{\rho_0}\delta + \frac{1}{\rho_0^2}x\delta - \frac{1}{\rho_0}\delta^2 - kx + kx\delta - \frac{1}{2}mx^2 + \dots, \end{aligned} \quad (2.12)$$

where k and m are the quadrupole and sextupole strengths respectively which in analogy to the dipole curvature Eq. 2.6, are related to g and s as [9]

$$k = \frac{ep}{g}, \quad k(\text{m}^{-2}) = 0.29956 \frac{g(\text{T/m})}{\beta E(\text{GeV})} \quad (2.13)$$

$$m = \frac{ep}{s}, \quad m(\text{m}^{-3}) = 0.29956 \frac{s(\text{T/m}^2)}{\beta E(\text{GeV})} \quad (2.14)$$

So, the equation of motion can be finally derived as follows:

$$x'' + \left(k + \frac{1}{\rho_0^2}\right)x = \frac{1}{\rho_0}\delta - \frac{1}{\rho_0}\delta^2 + \frac{1}{\rho_0^2}x\delta + kx\delta - \frac{1}{2}mx^2 \quad (2.15)$$

In the above equation the term $(1 - \delta)\delta/\rho_0$, refers to dispersion which expresses having different deflection angles for particles with an energy deviation from the ideal design energy. $(k + 1/\rho_0^2)x\delta$ represents the chromatic aberration which means that the quadrupole focusing strength is also depending on energy. The last term, $mx^2/2$, indicates the sextupole field which can partly cancel the chromatic aberration of the quadrupoles, but it leads to geometric aberrations. Keeping the constant and linear terms and considering no energy dispersion, *i.e.* $\delta = 0$, the homogeneous linear equation of motion in the deflection plane x is given by

$$x'' + Kx = 0, \quad K = \left(k + \frac{1}{\rho_0^2}\right) \quad (2.16)$$

Moreover, as in most cases, the deflection occurs only in the horizontal plane, the equation of motion in the vertical plane can be derived in a similar way as

$$y'' + Ky = 0, \quad K = -k \quad (2.17)$$

In fact, the final aim of beam dynamics calculations is to distribute magnets along the beam transport line in such a way that the solutions to the equations of motion result in the desired beam characteristics.

2.1.2. Phase-space and Twiss parameters

Looking at equation (2.16), if the restoring force K is constant with respect to s , it is a simple harmonic equation. However, as s is the longitudinal direction along the accelerator and there are different focusing requirements along this path, K varies sharply with s and we have $K(s)$. So, equation (2.16) is Hill's equation which can be solved as follows.

One can guess the solution to this 2nd order differential equation to be

$$x = \sqrt{\epsilon\beta(s)} \cos(\phi(s) + \phi_0) \quad (2.18)$$

. Where ϵ and ϕ_0 are constants defined by initial conditions. $\beta(s)$ and $\phi(s)$ are the amplitude modulation and phase advance which are dependent on the focusing strength, K . In order to simplify Eq. 2.18 some parameters are defined as below

$$\alpha = \frac{\beta'}{2}, \beta = \omega^2, \gamma = \frac{1 + \alpha^2}{\beta}, \phi = \phi(s) + \phi_0 \quad (2.19)$$

And we have

$$\begin{aligned} x &= \omega\sqrt{\epsilon}\cos(\phi) \\ x' &= \omega'\sqrt{\epsilon}\cos(\phi) - \omega\sqrt{\epsilon}\phi'\sin(\phi) \\ x'' &= \omega''\sqrt{\epsilon}\cos(\phi) - \omega'\sqrt{\epsilon}\phi'\sin(\phi) - \omega'\sqrt{\epsilon}\phi'\sin(\phi) - \omega\sqrt{\epsilon}\phi''\sin(\phi) \\ &\quad - \omega\sqrt{\epsilon}\phi'^2\cos(\phi). \end{aligned} \quad (2.20)$$

Inserting Eq. 2.20 into 2.16 yields,

$$\begin{aligned} \omega''\sqrt{\epsilon}\cos(\phi) - \omega'\sqrt{\epsilon}\phi'\sin(\phi) - \omega'\sqrt{\epsilon}\phi'\sin(\phi) - \omega\sqrt{\epsilon}\phi''\sin(\phi) \\ - \omega\sqrt{\epsilon}\phi'^2\cos(\phi) + K\omega\sqrt{\epsilon}\cos(\phi) = 0 \end{aligned} \quad (2.21)$$

Considering the “sin” terms we have

$$\begin{aligned} 2\omega'\phi' + \omega\phi'' &= 0 \\ 2\omega'\omega\phi' + \omega^2\phi'' &= 0 \\ \beta'\phi' + \beta\phi'' &= 0 \\ (\beta\phi')' &= 0 \end{aligned} \quad (2.22)$$

The finally reached expression is correct since $\phi' = 1/\beta$ which proves that our guessed solution satisfies Hill’s equation, [10]. Now for predicting the particle trajectory using equation (2.20) and substituting ω with α , β and γ we can write

$$\begin{aligned} x &= \sqrt{\epsilon\beta}\cos(\phi) \\ x' &= -\alpha\sqrt{\frac{\epsilon}{\beta}}\cos(\phi) - \sqrt{\frac{\epsilon}{\beta}}\sin(\phi) \end{aligned} \quad (2.23)$$

If we plot x' versus x for $0 < x' < 2\pi$ we have an ellipse which is determined by the parameters α , β , and γ named “Twiss parameters” and the ellipse is called phase-space ellipse. The orientation and shape of this ellipse are

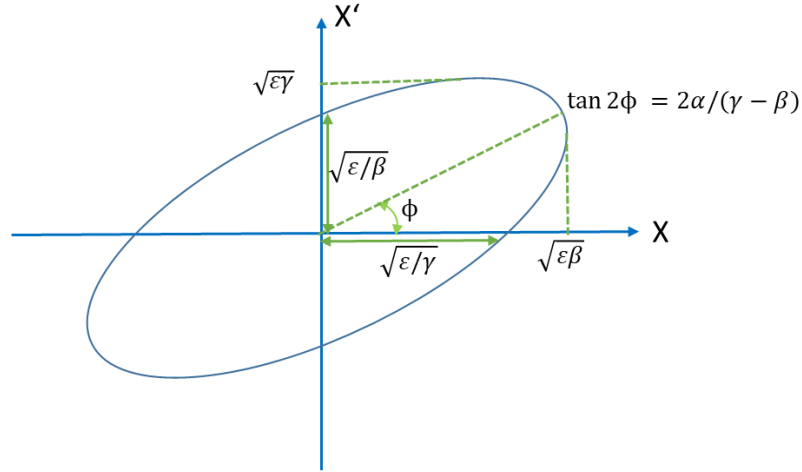


Figure 2.3.: Phase-space ellipse in the two-dimensional transverse phase space $x - x'$.

defined by the focusing properties of the magnets, whereas the area of the ellipse is an intrinsic property of the beam. As the particles go through the transport line or circulate in the ring, they encounter different magnetic elements, especially the quadrupoles which affect the β value. So the ellipse shape will be changed while the area of the ellipse remains constant for fixed particle energy and equal to $\pi\epsilon$, where ϵ is a constant of the single particle motion and is determined by initial beam parameters. Also, beam size σ_x , and beam divergence $\sigma_{x'}$ in the transverse plane can be defined as the ellipse projection on the x and x' axis, respectively.

$$\begin{aligned}\sigma_x &= \sqrt{\epsilon_x \beta} \\ \sigma_{x'} &= \sqrt{\epsilon_x \gamma}\end{aligned}\tag{2.24}$$

In fact, in a bunch of particles, every particle has its own ellipse in the phase-space and identifying the ellipse with the particle distribution is only valid if the phase-space distribution of the particles is Gaussian. Then this ellipse can be identified e.g. with the 1σ level of this Gaussian distribution. Also according to Liouville's theorem phase-space density is constant, no particle can escape the phase ellipse, any particle within the ellipse will stay within the ellipse and any particle outside the ellipse will stay outside. As discussed so far, desired particle dynamics can be obtained using specific magnetic fields which are generated by the different magnets. In the following sections, an introduction to the different types of magnets and their design concepts is presented.

2.2. Iron-core magnets

Electromagnets are magnets based on the creation of a magnetic field by an external current in normal conducting or superconducting coils. In these magnets, the field is amplified and the flux is guided using an iron core.

In this thesis, the main focus is on the magnet design and beam dynamics calculations in which ferromagnetic materials, which will be described later, are used for the HTS iron-core magnets to shape the field lines. So, general definitions and relations are given and for more details on the solid-state concepts, one can refer to the reference books like "foundations of electromagnetic theory" by J. R. Reitz et al. ([11]).

Using the current carrying coils and applying an external magnetic field H to a material, magnetic flux density B can be defined as a response of the medium magnetized by H . There is a relation between B and H which depends on the nature of the materials. To look through this concept, one should see how materials respond to an external magnetic field.

The magnetization M represents all the magnetic effects due to the material properties and is almost zero in unmagnetized status. But in the presence of an external magnetic field, M gets nonzero values depending on the applied magnetic field H

$$M = \chi_m H \quad (2.25)$$

the dimensionless quantity χ_m is magnetic susceptibility and indicates the response of the material to the external field. Paramagnetic materials like aluminum or platinum, with $\chi_m > 0$, align with the applied magnetic field and strengthen the field while diamagnetic materials like Gold, Water, and copper, with $\chi_m < 0$, are anti-aligned and weaken the magnetic fields. In both Paramagnetic and diamagnetic materials, the magnetic susceptibility χ_m is much smaller than one. Ferromagnetism, in contrast, refers to materials (such as iron and nickel) that can retain their magnetic properties when the magnetic field is removed. If a ferromagnetic substance is heated, then at a definite temperature, the Curie temperature, the ferromagnetic property of the substance disappears and the substance becomes paramagnetic. Writing Ampere's law, including current density from the current carrying coils J and atomic currents with magnetization current density J_m , one can

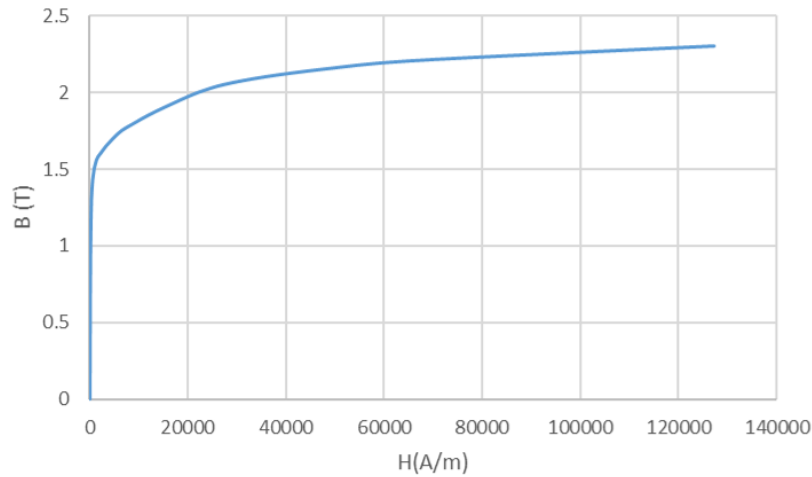


Figure 2.4.: XC-06 magnetic steel magnetization curve using the data from [12], the author permission is granted.

write,

$$\begin{aligned}\nabla \times B &= \mu_0(J + J_m) \\ \nabla \times M &= J_m, \quad \nabla \times H = J\end{aligned}\tag{2.26}$$

inserting equation(2.25) in (2.26)

$$\begin{aligned}B &= \mu H \\ \mu &= \mu_0(1 + \chi_m)\end{aligned}\tag{2.27}$$

In the above equations, H and M have the dimension of $A\ m^{-1}$ and B is in T, using the SI unit system. μ is the magnetic permeability and for ferromagnetic materials is not constant but depends on the value of H , *i.e.* $\mu = \mu(H)$. Also, depending on the material chemical properties and contents, see sub-section 2.2.7.1, magnetic permeability is different for an applied magnetic field for different materials and can be, for example, as large as $10^5\mu_0$ in Permalloy that is a nickel-iron magnetic alloy.

In ferromagnetic materials by increasing the applied magnetic field H , the magnetic flux density B increases until the material reaches its highest magnetization M which is named saturation. After reaching saturation, a further flux density increase is due to the term $\mu_0 H$ only and the material can no more play a role in strengthening the field. The magnetization curve, $B - H$ curve, of a common type of magnetic steel XC-06, from Industeel supplier, [12], is plotted in Fig. 2.4. Since the iron core is saturated about 2 T and normal conducting copper coils can tolerate current densities up

to 10 A mm^{-2} depending on the cooling technique (optimum 5 A mm^{-2} in direct current applications), these magnets are usually used to generate field up to 2 T. But also in the case of superconducting coils generating much higher flux densities, iron cores can be used to guide and shape the field even if fully saturated. Magnets in most of the storage and booster rings in accelerator facilities have iron cores and are powered by direct current or low-frequency alternating currents. Also, fast-ramped magnets such as septa and kickers which are used to inject and extract beams at the beginning and end of transport lines have the same structure and can fall into this category. In the following, we will introduce the common types of magnets used in accelerators and express the relationships that govern them.

2.2.1. Multipole Fields

In order to have the required beam dynamics a variety of magnets is needed. Bending magnets or dipoles with a constant field are used to guide the beam, Quadrupoles are mainly used to focus the beam, and sextupoles are to correct the chromatic effects. As was discussed before, to investigate the beam dynamics and particle movements and deviations with respect to the ideal path, the curvilinear coordinate system is usually used which moves together with the reference particle. Magnets and the related magnetic fields are usually described with the Cartesian coordinate system located at each magnet center in which x, y , and z represent horizontal, vertical, and longitudinal directions, respectively. For beam dynamics, we are primarily interested in the field around the beam, between the iron poles, and away from the excitation currents. So according to the Maxwell equation, we have

$$\nabla \times B = 0 \quad , \quad \nabla \cdot B = 0 \quad (2.28)$$

And such a magnetic field can be derived from a scalar potential function $\psi(x, y, z)$ which is a solution to Laplace's equation

$$\nabla^2 \psi = 0 \quad , \quad \vec{B} = -\nabla \psi \quad (2.29)$$

To simplify the derivation of the multipole fields we may use cylindrical symmetry and rewrite Laplace's equation for the scalar potential in a

cylindrical coordinate system (r, φ, z) .

$$\nabla^2 \psi = \frac{\delta^2 \psi}{\delta r^2} + \frac{1}{r} \frac{\delta \psi}{\delta r} + \frac{1}{r^2} \frac{\delta^2 \psi}{\delta \varphi^2} + \frac{\delta^2 \psi}{\delta z^2} = 0 \quad (2.30)$$

So the solution is in the form of a Taylor expansion with respect to the reference path and can be written as

$$\psi(r, \varphi, z) = -\frac{cp}{e} \sum_{n>0} \frac{1}{n!} A_n(z) r^n e^{in\varphi} \quad (2.31)$$

For any higher-order multipole *i.e.* any arbitrary n the scalar potential in the middle plane, $z = 0$, is given as follows

$$\psi_n(r, \varphi) = -\frac{cp}{e} \frac{1}{n!} A_n r^n e^{in\varphi} \quad (2.32)$$

which, in Cartesian coordinates becomes

$$\psi_n(x, y) = -\frac{cp}{e} \frac{1}{n!} A_n (x + iy)^n \quad (2.33)$$

where real and imaginary terms represent two basic field orientations and only the imaginary solution fulfills the mid-plane symmetry in which there are no horizontal field components in the midplane, $y = 0$, and $\text{Im}(\psi_n(x, y)) = -\text{Im}(\psi_n(x, -y))$ or $B_{ny}(x, y) = B_{ny}(x, -y)$. The family of scalar equipotentials is orthogonal to the vector equipotentials and can represent possible pole shapes. If we write down the potential terms up to $n = 3$, the pole shape for dipole ($n = 1$), quadrupole ($n = 2$) and sextupole ($n = 3$) can be derived.

$$\begin{aligned} -\frac{e}{cp} \psi_1(x, y) &= A_1 x + i A_1 y \\ -\frac{e}{cp} \psi_2(x, y) &= \frac{1}{2} A_2 (x^2 - y^2) + i A_2 x y \\ -\frac{e}{cp} \psi_3(x, y) &= \frac{1}{6} A_3 (x^3 - 3xy^2) + i \frac{1}{6} A_3 (3x^2 y - y^3) \end{aligned} \quad (2.34)$$

In the above equation, magnets' pole shapes defined by the imaginary solution are called upright magnets, and real solutions of scalar potential are defined as the so-called rotated magnets. So the upright multipole magnetic fields can be derived from the imaginary solution of the Laplace equation.

Replacing the coefficients A_n with the multipole strength parameters, [9], the three first magnetic field multipoles are compiled in Table 2.1 Therefore the general magnetic field equation includes only the most commonly used upright multipole elements in the horizontal midplane, where $y = 0$, are given by

$$B_y = \sum_{n=1}^{\infty} B_n = \sum_{n=1}^{\infty} b_n x^{n-1} = \text{constant} + gx + \frac{1}{2}sx^2 + \dots \quad (2.35)$$

A pure multipolar field has only one nonzero B_n for a given value of n , which is called the main order of the field. As an example, $n = 1$ is a pure dipole and $n = 2$ is a quadrupole. Nonzero B_n for n other than the main order are usually referred to as field harmonics or field errors. Allowed higher order multipoles, which comes from the finite transverse length of the pole profile, in dipole magnet are $n = 3, 5, 7, 9, \dots, (2n+1)$ which are sextupole, tenth-pole, fourteenth-pole, and $2(2n+1)$ pole components. For quadrupoles the allowed higher order harmonics are $n = 6, 10, 14, \dots$ (12 pole, 20 pole, etc.) and for sextupoles are $n = 9, 15, 21, \dots$ (18 pole, 30 pole, etc.).

2.2.2. Dipoles

In circular accelerators or curved transport lines, dipoles are the main magnets. Dipole magnets have two iron poles and two current-carrying coils, and by creating a uniform magnetic field (perpendicular to the beam path) between the two magnetic poles, they are responsible for bending the beam in a circular path. In any ideal dipole magnet, the pole profile points and the magnetic field as a function of the horizontal direction obey Eq.

Table 2.1.: Upright multipole fields.

Magnet type	B_y
Dipole	$\frac{e}{p}B_1 = \text{constant}$
Quadrupole	$\frac{e}{p}B_2 = kx$
Sextupole	$\frac{e}{p}B_3 = \frac{1}{2}m(x^2 - y^2)$

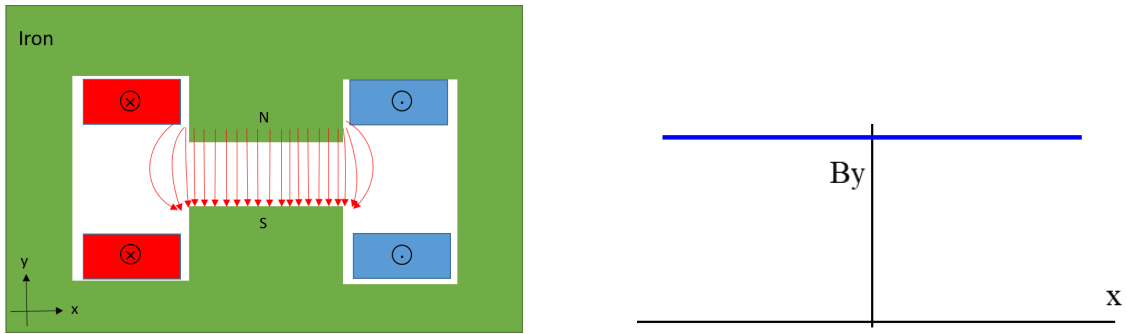


Figure 2.5.: Dipole magnet cross-section (left) and magnetic field distribution in the horizontal direction (right).

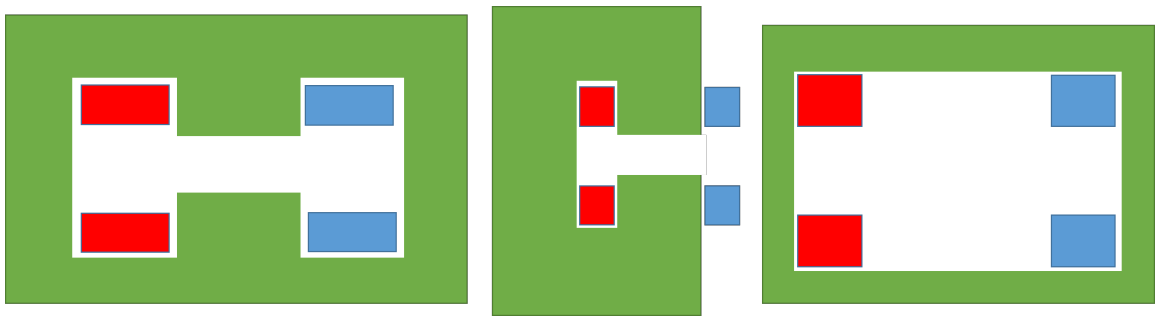


Figure 2.6.: Standard shapes of dipole magnet; H shape (left), C-shape (center) and O-shape (right). The green color represents the iron yoke, and the blue/red color is used to show the current carrying coils.

(2.36).

$$y(x) = \pm \frac{h}{2} \quad (2.36)$$

$$B_y(x) = \text{constant}$$

h is the magnet's full gap. Dipole magnets are usually designed and fabricated in three standard shapes, H shape, C shape, and O shape or window frame, Fig. 2.6. To select between these shapes, one needs to consider the required conditions. In C-shape dipoles, access to the magnet gap and therefore vacuum chamber alignment and installation is easier. Also if a beamline is needed to be extracted from the dipole magnet, C-shape ones are usually used. In H-shape dipole magnets we have symmetry in both transverse planes and it provides a higher rigidity whereas access to the gap is more difficult. In order to derive the relation of the central magnetic field to the applied current, looking at Fig. 2.7 and using Ampere's law, we have,

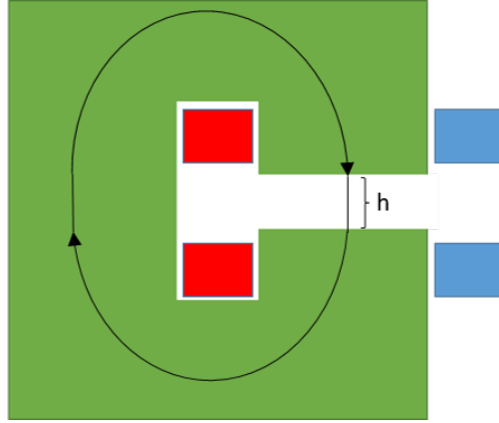


Figure 2.7.: Integration path in a dipole magnet.

$$\begin{aligned}
 \oint_C H \cdot dl &= NI \\
 \int_{gap} H \cdot dl + \int_{iron} H \cdot dl &= NI \\
 \int_{gap} H \cdot dl = \frac{Bh}{\mu_0}, \quad \int_{iron} H \cdot dl &= \frac{B\lambda}{\mu_{iron}} \\
 \frac{Bh}{\mu_0} \gg \frac{B\lambda}{\mu_{iron}} \Rightarrow NI_{per\ pole} &= \frac{Bh}{2\mu_0}
 \end{aligned} \tag{2.37}$$

In Eq. (2.37) H is the magnetic field created by the coils, μ_0 is the vacuum permeability, μ_{iron} is the iron permeability which is larger than $10^3\mu_0$, h is the magnet full gap and λ is the average length of the integration path in the iron yoke.

2.2.3. Quadrupoles

Quadrupole magnets are the second most common type of magnets that are used in accelerators and are responsible for focusing the particles on the central beam path. Each iron-core quadrupole magnet has four iron poles with a hyperbolic profile and four coils. These magnetic lenses impart a transverse momentum kick, ΔP , to the particle beam with momentum P . For a field that increases linearly with x , the resulting kick, ΔP , will also increase linearly with x . Figure 2.8 shows the quadrupole magnet cross-section and the field shape. Particles traveling in an accelerator have to be kept as close as possible to the reference orbit by means of focusing forces acting perpendicularly to the reference orbit. This is achieved by a

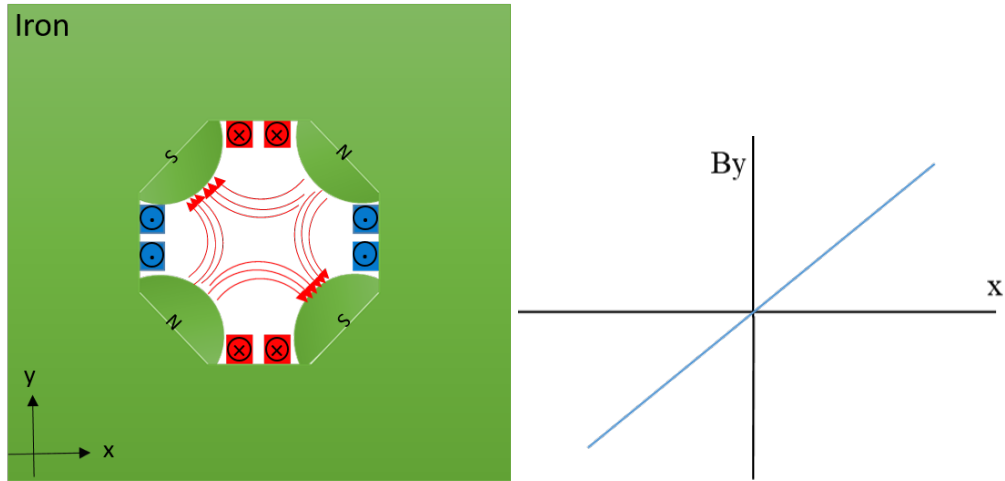


Figure 2.8.: Quadrupole magnet cross-section (left) and magnetic field distribution in the horizontal direction (right).

combination of focusing and defocusing quadrupoles and a non-focusing element which could be either a dipole or a drift space. The focusing quadrupoles focus the beam in one plane but defocus it in the other plane, and inversely for the defocusing ones. In any ideal quadrupole for the area around the mid-plane, pole profile coordinates and magnetic field as a function of the horizontal direction obey the Eq.(2.38).

$$xy = \frac{R^2}{2} \quad (2.38)$$

$$B_y(x) = gx, \quad B_x(y) = gy, \quad g = \frac{dB}{dr}$$

In Eq. 2.38, R is the magnet aperture radius and g is the quadrupole gradient. Quadrupoles are mainly designed in three common shapes which are shown in Fig. 2.9, Each of these quadrupole shapes has its advantages and disadvantages, which should be used according to the application requirements. For example, Collin quadrupoles provide free space for beamlines, however at the cost of reduced mechanical stability, a more complicated assembly, and therefore a more expensive fabrication. Using Ampere law and considering the closed integration path in Fig. 2.10 the relation between the magnetic field and current in quadrupole magnets can be derived as follows,

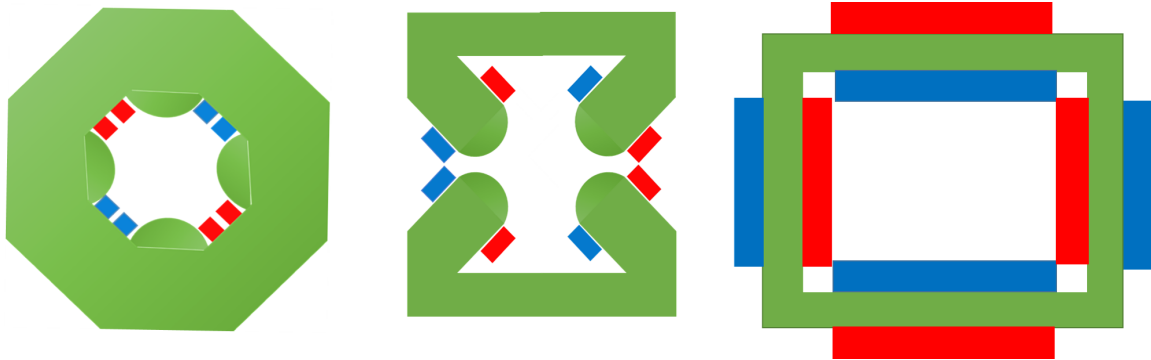


Figure 2.9.: Standard (left), Collin (center), and Panofsky (right) quadrupoles. The green color represents the iron yoke, and the blue/red color is used to show the current carrying coils.

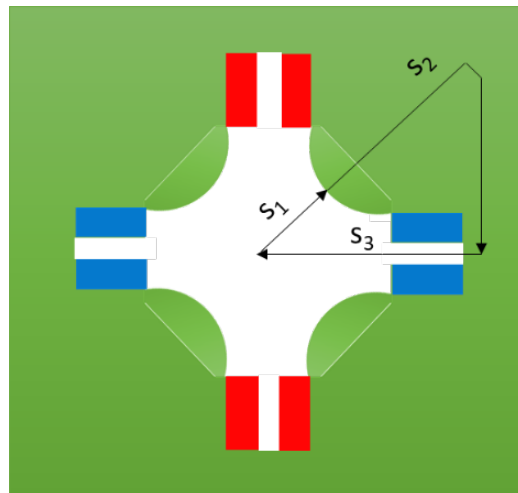


Figure 2.10.: Integration path in a quadrupole magnet.

$$\begin{aligned}
 \oint_C H \cdot dl &= NI \\
 \int_{S_1} H \cdot dl + \int_{S_2} H \cdot dl + \int_{S_3} H \cdot dl &= NI \\
 \int_{S_1} H \cdot dl = \int_{S_1} \frac{gr}{\mu_0} dr, \int_{S_2} H \cdot dl \approx 0, \int_{S_3} H \cdot dl &= 0 \\
 \Rightarrow NI_{per\ pole} &= \frac{gR^2}{2\mu_0}
 \end{aligned} \tag{2.39}$$

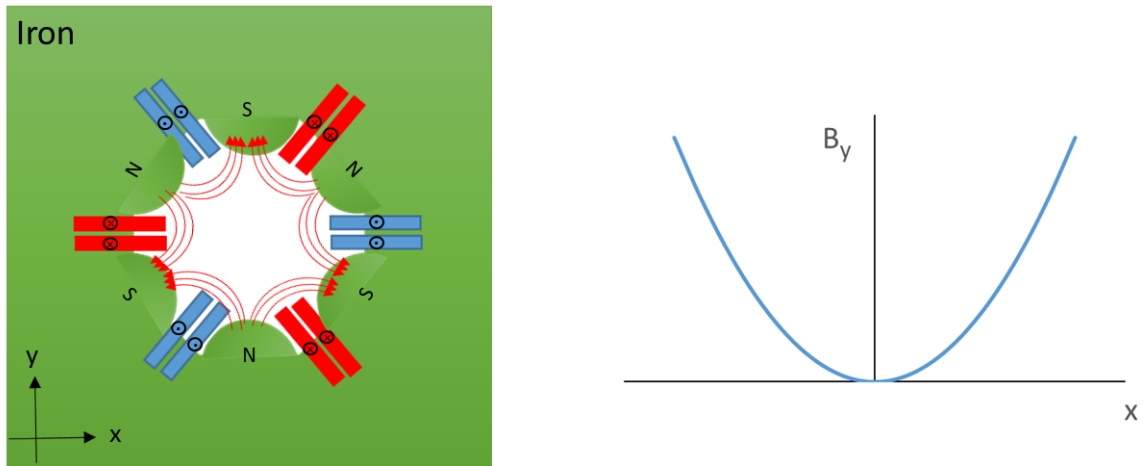


Figure 2.11.: Sextupole magnet cross-section (left) and magnetic field distribution in the horizontal direction (right).

2.2.4. Sextupoles

Sextupole magnets are mostly used in circular accelerators to correct chromatic aberrations. In fact, particles with different energies are focused to different points when they reach quadrupole magnets and sextupole magnets are used to prevent this scattering of the particles. These multipole magnets can also be used to compensate for the six-pole component caused by dipole magnets, *i.e.* the first allowed error of dipole magnets. In any ideal sextupole, pole profile coordinates and magnetic field versus horizontal direction can be obtained by Eq. 2.40.

$$\begin{aligned}
 3x^2y - y^2 &= \pm R^2 \\
 B_y(x) &= \frac{1}{2}sx^2, \quad s = \frac{d^2B}{dr^2},
 \end{aligned}
 \tag{2.40}$$

where R is the magnet aperture radius and s is the sextupole component. Using Ampere's law, one can calculate the magnetic field in terms of magnet coil current, Fig. 2.12 and equation (2.41).

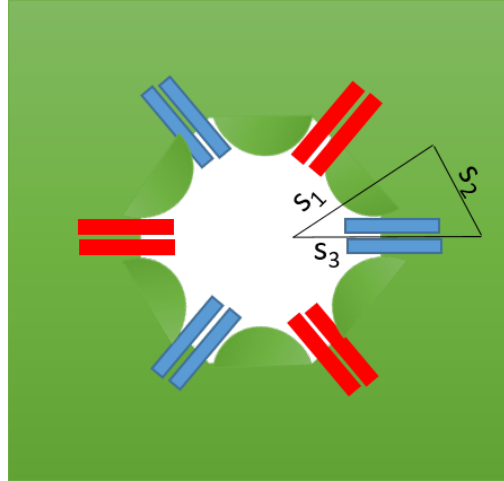


Figure 2.12.: Integration path in a sextupole magnet.

$$\begin{aligned}
 \oint_C H \cdot dl &= NI \\
 \int_{S_1} H \cdot dl + \int_{S_2} H \cdot dl + \int_{S_3} H \cdot dl &= NI \\
 \int_{S_1} H \cdot dl &= \int_{S_1} \frac{sr^2}{2\mu_0} dr, \int_{S_2} H \cdot dl \approx 0, \int_{S_3} H \cdot dl = 0 \\
 \Rightarrow NI_{per\ pole} &= \frac{sR^3}{6\mu_0}
 \end{aligned} \tag{2.41}$$

2.2.5. Combined-function magnets

Combined-function magnets combine several different functions together in one magnet. These magnets can save energy, space, and cost and are of great interest in compact accelerators in spite of design and fabrication complications. For example, a combined dipole with a superimposed quadrupole, both guides and focuses the particle beam, or a quadrupole magnet that also acts as a sextupole and is a common type of magnet in many accelerators [13, 14]. In these magnets, combined fields are usually created by applying changes to the pole equation, Fig. 2.13 and Table 2.2, or by placing additional coils, Fig. 2.14.

Looking at the bottom side of Fig. 2.13, to have an integrated sextupole component in the quadrupole magnet, here 3.22 T m^{-2} , the pole profiles are rotated by 0.467° clockwise. But this rotation causes an unwanted dipolar component in the center, in order to eliminate this component two different

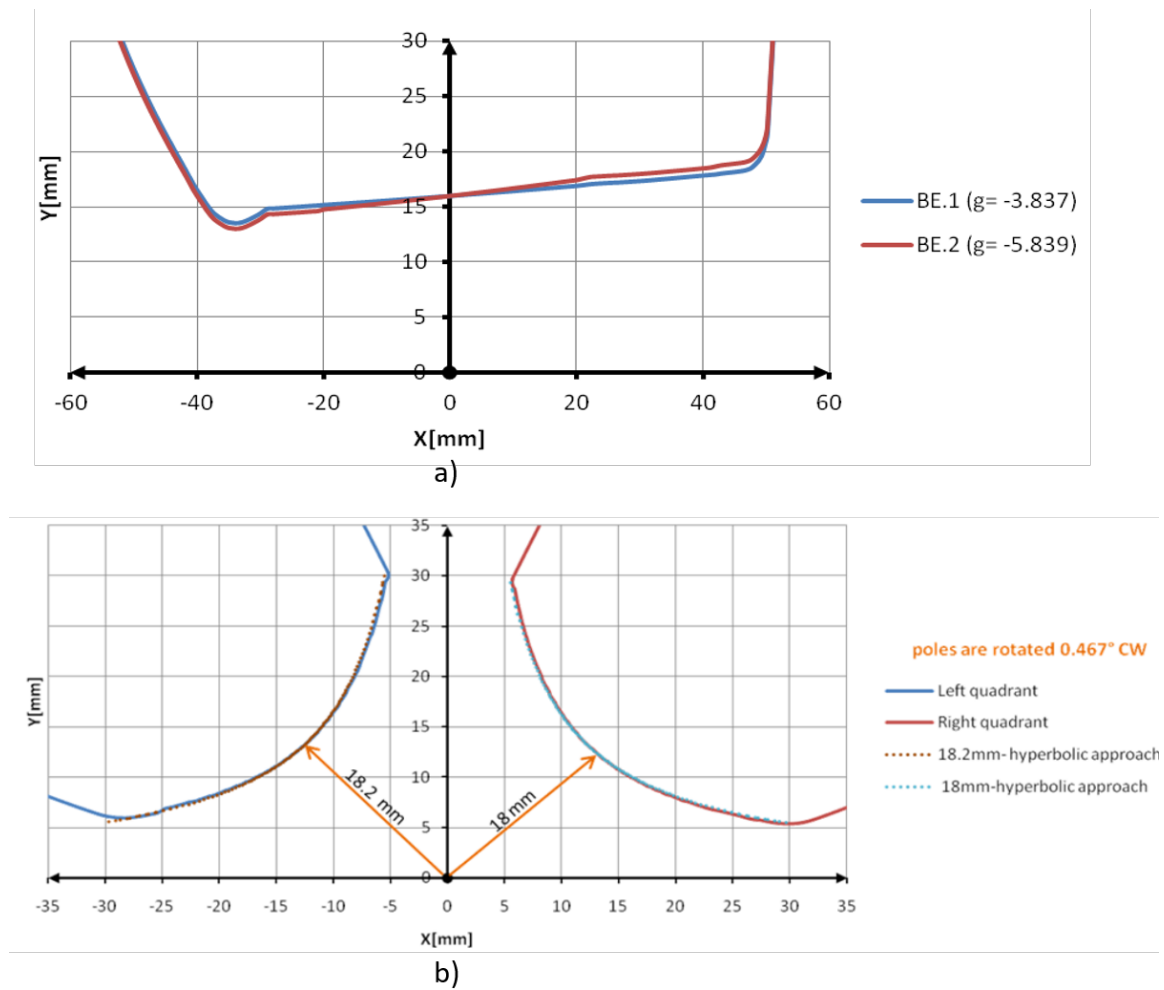


Figure 2.13.: Designed pole profiles for; combined function dipole with the dipole field of $B = 1.42$ T and two different quadrupole components (top) [15] and combined function quadrupole with sextupole component (bottom) [16], both these designs were done by S. Fatehi for the ILSF magnets.

Table 2.2.: Pole profile equation for the common combined-function magnets.

Magnet type	Pole equation
Dipole+Quadrupole	$y = h(0)/(1 + \frac{gx}{B_0})$
Dipole+Quadrupole+sextupole	$y = h(0)/(1 + \frac{gx}{B_0} + s\frac{x^2}{2B_0})$
Quadrupole+sextupole	$gxy + s(x^2y - \frac{y^3}{3}) = cte$

apertures, 18 mm and 18.2 mm, are imposed on the left and right poles. Figure 2.14 shows a sextupole magnet with combined dipole and skew

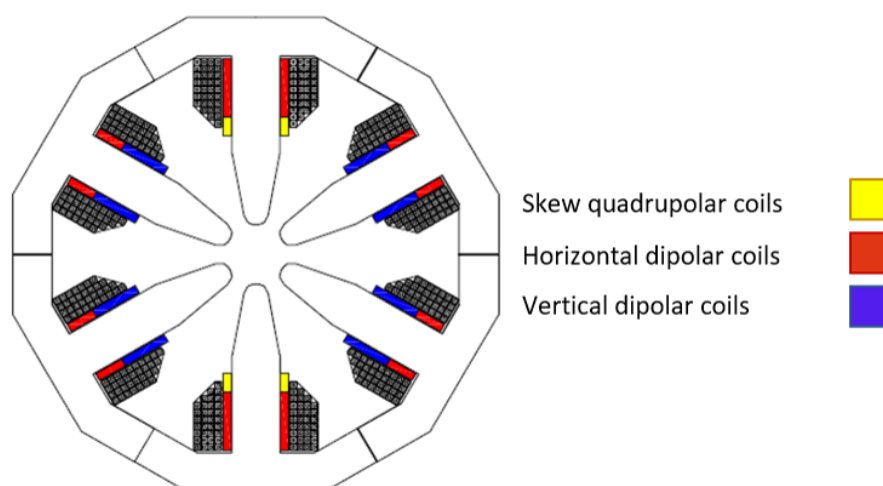


Figure 2.14.: Sextupoles magnet with superimposed dipolar and quadrupolar fields.

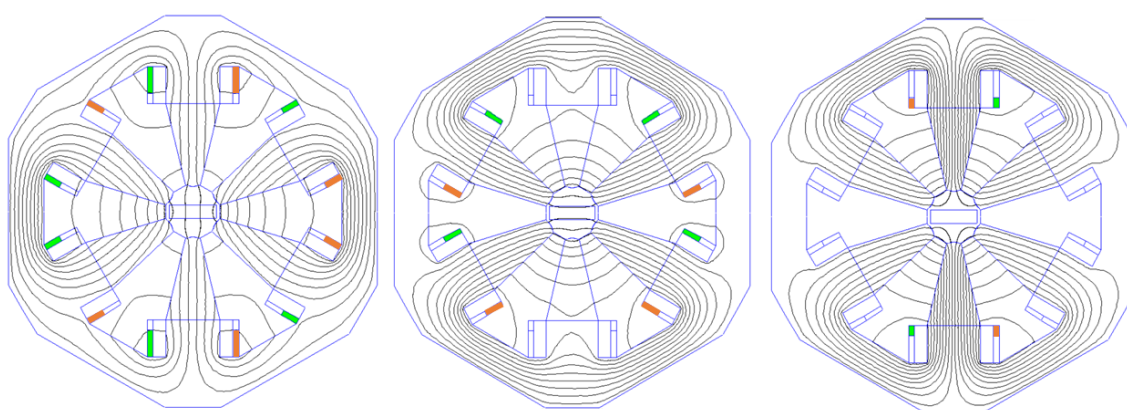


Figure 2.15.: Field lines inside a combined function sextupole, when the sextupole coils are off and horizontal correction (left), vertical correction (center), and skew quadrupole coils are on. In Steering coils, green and orange represent, the positive and negative current flux in each coil respectively, this design is developed by S. Fatehi and published in ILSF conceptual design report [17].

quadrupole components, in which the additional fields are created using extra, independently powered coils. Skew quadrupolar auxiliary windings are energized with the same polarity, while for the horizontal steering windings the polarity at the poles 30° , 90° and 150° is opposite to that of poles 210° , 270° , and 330° . Vertical steering is generated when the polarity at poles 150° and 210° is opposite to that of 30° and 330° , which leads to the field lines as shown in Fig. 2.15.

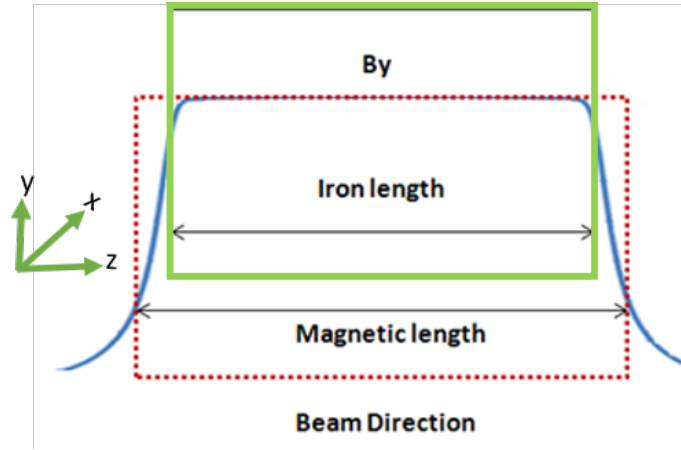


Figure 2.16.: Schematic view of magnetic length.

2.2.6. Magnetic length

If we approach a magnet with a measuring probe in the longitudinal direction, the measuring device detects the presence of a magnetic field adjacent to the two ends of the magnet. The field increases slowly by approaching the magnet ends and remains constant in the gap space in the center of the magnet. By integrating the magnetic field on the beam path, it can be seen that this value is always greater than the multiplication of the field and the mechanical length of the magnet. Therefore, the quantity of "magnetic length" is defined as follows[18]

$$L_{\text{mag}}(x) = \int \frac{B(x, y, z)}{B_0} dz \quad (2.42)$$

where B_0 is the field at the magnet center *i.e.* at $x = y = z = 0$.

In the special cases where the mechanical length is much larger than the size of the magnetic gap, the following approximate relations are valid.

$$\begin{aligned} \text{Dipole} \quad L_{\text{mag}} &= L_{\text{iron}} + 2hK \\ \text{Quadrupole} \quad L_{\text{mag}} &= L_{\text{iron}} + 2RK \end{aligned} \quad (2.43)$$

h is the full gap length in dipoles, R is the aperture radius in quadrupoles, L_{iron} is the mechanical length of the magnet and K is the geometry-specific constant which is equal to 0.54 and 0.45 for dipoles and quadrupoles respectively. Although the exact value of K should be calculated by numerical calculations for each magnet [19].

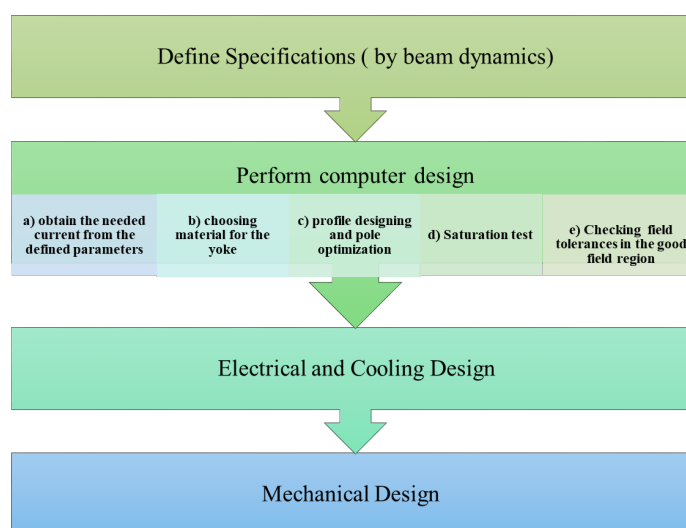


Figure 2.17.: Schematic view of the magnet design procedure.

2.2.7. Principles of magnet design

The purpose of designing the magnets is to have a system with reliable operation and a high safety factor at a reasonable price in a reasonable time. Since the particle beam goes through the magnets, single turn or several turns, achieving the desired quality for the magnetic field and low field errors is very important. Therefore, keeping the required field tolerances must be considered at every stage of design. This section describes methods that can be applied in magnet design to fulfill the required tolerances and conditions. In Fig. 2.17, the common design steps are given.

2.2.7.1. Determining the iron core material

One of the most important design steps is to determine the type of iron, which varies according to the type of application. For example, ferromagnetic blocks can be used in DC current magnets, while in the magnets with AC current (up to several kHz) to prevent eddy current, it is necessary to use sheets of non-oriented electrical steel with a thickness of less than 1 mm [18].

In order to improve the magnetic and mechanical properties of the iron sheet, it is annealed in the presence of a low-carbon atmosphere. Carbon percentage is one of the important factors in choosing yoke material as

increasing the carbon percentage causes saturation in lower fields and increases the hardness. Therefore lower carbon percentage is preferred.

Using silicon in addition results in higher punch ability, fewer burrs, and less hysteresis loss. In the production of electric steels, it is necessary for the magnetic properties to be constantly uniform throughout the length of the sheet and from sheet to sheet. For further reduction of eddy current, the sheets are covered by insulating materials on both sides. The most common type of electrical steel is AISI1010 (maximum 1% carbon 0.3% silicon) and one of the best quality ones is M1200-100A (maximum 0.003% carbon 1.3% Silicon) from ThyssenKrupp Steel Europe AG. [20]. AISI1010 is named after American Iron and steel standards and is equivalent to DIN EN 1.0032 in Europe.

2.2.7.2. Pole profile design and optimization

One of the most important and influential parameters in the design of the magnets is "having good field quality in the good field region (GFR)", which is defined and determined by beam specifications during the lattice design. In the GFR the field quality, $\Delta B/B_0$, needs to be kept such that higher-order multipoles do not affect the beam dynamics. Therefore, after determining the main parameters of the magnet, including field strength, magnet length, and magnet aperture size using existing design codes such as Opera [21], poisson[22], FEMM [23], magnetic design begins. The main steps in designing magnets, to achieve the required field quality, are given in the following.

Shimming and tapering In the magnets, due to limited space and the need to locate the coils, the pole profile cannot continue indefinitely and must be cut somewhere. Limiting the size of the magnetic pole disturbs the quality of the field and increases the values of the higher-order components of the field. The first step is to determine a cut-off point according to the needed GFR, then, a shim, as shown in Fig. 2.18, is added to the pole profile from this cutting point, which causes the concentration of the magnetic field at this edge. To reduce the accumulation of field lines, some iron is reduced from the profile and since the sharp points are unattainable during construction, these corners are chamfered and rounded with a small radius. Moreover, in order to avoid saturation at upper excitation levels of the magnet, the pole root is usually tapered slightly outwards [18, 24].

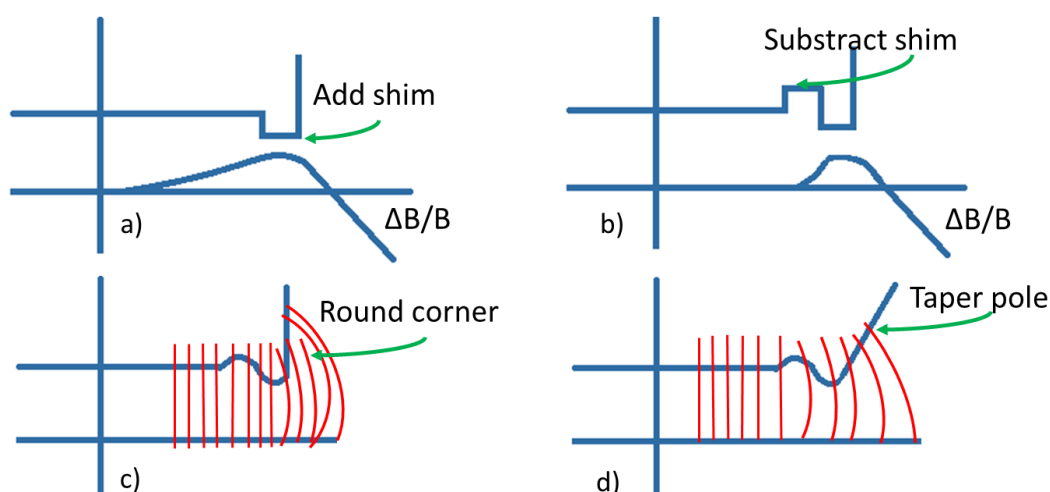


Figure 2.18.: Schematic of the shimming process according to the explanations in [24].

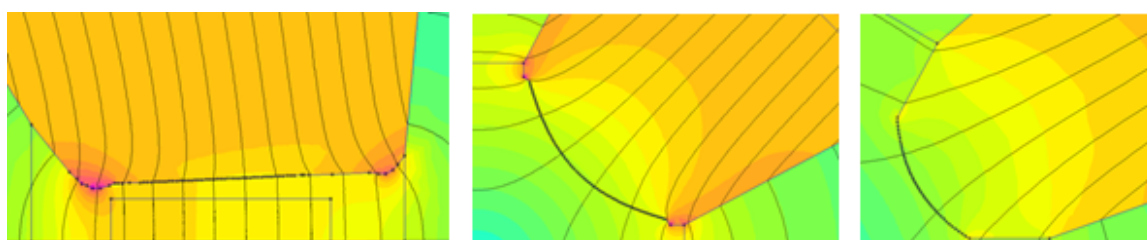


Figure 2.19.: Pole profile and shim shapes designed by FEMM for combined function dipole (left), quadrupole (center) and sextupole (right) magnets [26], designs were done by S. Fatehi.

Figure 2.19 shows some examples of pole profile and shim shapes designed by FEMM software for dipole, quadrupole, and sextupole magnets are given.

2.2.7.3. Field quality

After the shimming process, in order to finalize the shape of the pole and the shim, it is necessary to check the quality of the field and test the required quality value which is usually of the order of 10^{-4} in the good field region. The field quality for the three common magnets; dipole, quadrupole, and



Figure 2.20.: Chamfers on H-type dipole magnet (left) and quadrupole magnets (right).

sextupole is obtained from the following equations [25],

$$\begin{aligned}
 \text{Dipole} \quad \frac{\Delta B}{B_0} &= \frac{B - B_0}{B_0} \\
 \text{Quadrupole} \quad \frac{\Delta g}{g_0} &= \frac{g - g_0}{g_0} \\
 \text{Sextupole} \quad \frac{\Delta s}{s_0} &= \frac{s - s_0}{s_0}.
 \end{aligned} \tag{2.44}$$

2.2.7.4. Chamfering

In order to study the end fields of the magnet due to the limited length of the iron core and the coil, it is necessary to examine the magnets in three dimensions. In the three-dimensional design, which can be done by codes such as Opera[21], RADIA [27], MERMAID [28], etc. The two ends of the magnet are cut to a certain angle and depth so that the quality of the field integral and the integrated higher-order multipoles do not exceed the permitted values. The field integral quality is obtained by integrating the relations in equation (2.44). In other words, the best chamfer is the one that keeps the magnetic length, see sub-Section 2.2.6, constant in the good field region. Figure 2.20 shows two samples of chamfers on H-type dipole magnets and quadrupole magnets of the Iranian Light Source Facility (ILSF) booster ring.

2.3. Air-core magnets

Magnets play a key role in accelerators and maintain the particle beam with the required characteristics on the desired path by applying a fixed field

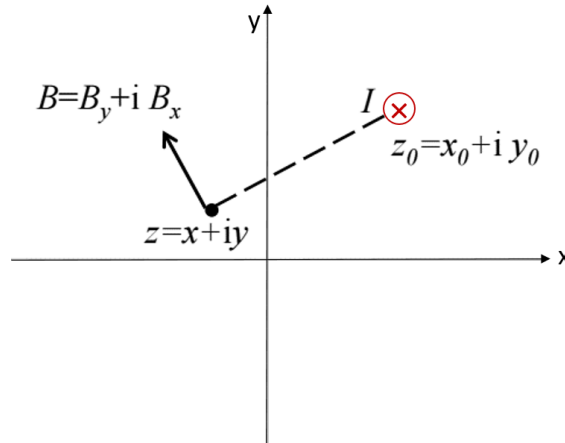


Figure 2.21.: Magnetic field generated in z by an infinitely thin current line placed at z_0 , geometric plane represented by complex plane.

(dipole magnet) or a radial field (quadrupole, sextupole, etc.), perpendicular to the path of the beam. Although magnets have no role in particle acceleration, in the relativistic relationships the final beam energy is directly proportional to the dipolar field, B , and the bending radius R , as it was discussed in Section 2.1.

$$E(\text{GeV}) = 0.3B\rho(\text{Tm}) \quad (2.45)$$

ρ is the radius of curvature, Larmor radius, B is the magnetic field and E is particle energy. In air-core magnets, compared to iron-core magnets, the magnetic field is determined by the spatial distribution of the winding currents. For this reason, the shape of the coil must be optimized to achieve the highest field and the best field quality. In air-core magnets, especially the superconducting ones, because of the required high magnetic field, forces of several ten/hundred kilonewtons are exerted on the coils. So, to maintain mechanical stability and magnet rigidity a non-magnetic mechanical structure is also required. Moreover, the use of iron cores in these types of magnets is generally for shielding purposes to block the generated high-strength magnetic field from surrounding devices. Starting with the Biot–Savart law, one can derive how to make a ‘good’ dipole or quadrupole field with current carrying lines independent of the specific features of superconductivity. This is the main building block that can be used to construct the so-called cos-theta layout. Using Biot–Savart law for the magnetic field generated by a current line, Fig. 2.21, one can obtain:

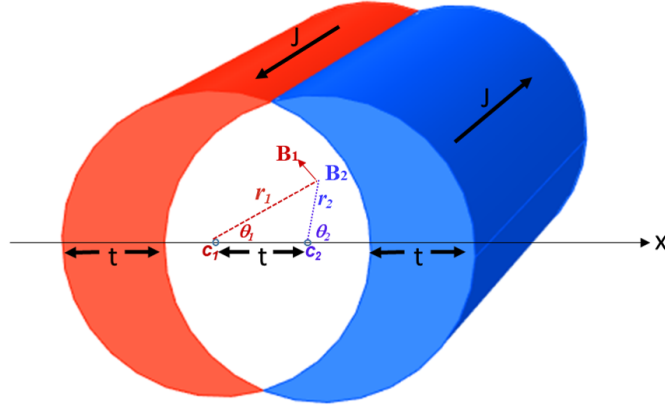


Figure 2.22.: Two overlapping cylinders with current density J , the center points C_1 and C_2 separated in x direction by a distance t .

$$\begin{aligned}
 B &= \frac{\mu_0 I}{2\pi(z - z_0)} \\
 &= \frac{-\mu_0 I}{2\pi z_0} \frac{1}{\left(1 - \frac{z}{z_0}\right)} \\
 &= \frac{-\mu_0 I}{2\pi z_0} \sum_{n=1}^{\infty} \left(\frac{z}{z_0}\right)^{n-1}
 \end{aligned} \tag{2.46}$$

Comparing equations 2.46 and 2.35, we obtain the multipoles of a current line,

$$B_n + iA_n = \frac{-\mu_0 I}{2\pi z_0} \left(\frac{R_{ref}}{z_0}\right)^{n-1}. \tag{2.47}$$

Where the reference radius R_{ref} has no physical meaning, it is just a choice of units to express the multipoles and is usually chosen to be $2/3$ of the magnet aperture, [29]. Moreover, using the Ampere law and considering two overlapping cylinders with current density J which flow in opposite directions, one can show that it gives a perfect dipole field in the aperture, where the currents cancel out each other,[30]. The magnetic field inside a cylinder carrying uniform current density can be derived as

$$\begin{aligned}
 \oint_C B \cdot dl &= \mu_0 I \\
 2\pi r B &= \mu_0 J \pi r^2 \\
 B &= \mu_0 \frac{Jr}{2}
 \end{aligned} \tag{2.48}$$

Now using Eq. 2.48, looking at Fig. 2.22 and combining the effect of the two cylinders we have

$$\begin{aligned} B_x &= \mu_0 \frac{J}{2} (r_1 \cos \theta_1 + r_2 \cos \theta_2) = 0 \\ B_y &= \mu_0 \frac{J}{2} (-r_1 \sin \theta_1 + r_2 \sin \theta_2) = \mu_0 \frac{Jt}{2} \end{aligned} \quad (2.49)$$

Obtaining the vector potential from the Eq. 2.46, a pure dipole field can be also created using a cos-theta current distribution with a current density that varies as a function of the azimuthal angle θ , [31].

$$J = J_0 \cos \theta. \quad (2.50)$$

This means that there is a maximal current on the mid-plane, with the opposite signs on the left and right sides of the aperture, and zero current at 90° and 270° . This can be realized by sector coils with a uniform current density that are separated with wedges, see sections 2.3.1 and 2.3.2.

This form of current density not only creates a dipole field but is also the most optimal form of current distribution that generates the most flux and magnetic energy [29]. This means that the number of Ampère turns required to create a given field, in this case, is less than any other distribution. This is especially important in superconducting magnets, where the cost of the wire is an important part of the expenditure. Like dipoles, quadrupolar fields can also be obtained by a constant-thickness current shell t in which the current density depends on the following relation,[31],

$$J = J_0 \cos 2\theta. \quad (2.51)$$

In fact, any spherical current distribution with current density $J = J_0 \cos n\theta$ forms a multipolar field of order n . In practice, superconducting magnets are composed of shells with a constant current density that is arranged by spacer components in such a way as to create a $\cos\theta$ current distribution, [29, 31].

2.3.1. Dipoles

As discussed in the previous section, a $\cos\theta$ current distribution can create a good dipolar field and can be approximated and realized by sector coils,

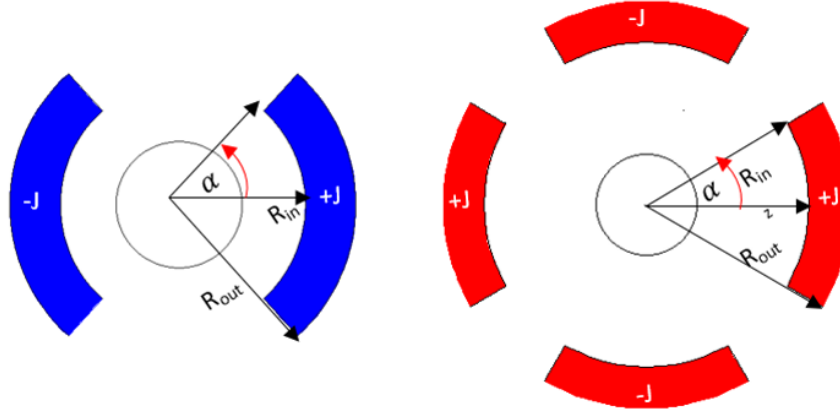


Figure 2.23.: Sector coil dipole (left), and quadrupole (right).

Considering Fig. 2.23 and Eq. 2.47 for $n = 1$ we can write

$$B_1 = \frac{-\mu_0 I}{2\pi} \Re\left(\frac{1}{z}\right), \quad z = r e^{i\theta} \quad (2.52)$$

$$B_1 = \frac{-\mu_0 I \cos \theta}{2\pi r}$$

In cylindrical coordinates, we have $I = Jr dr d\theta$ so

$$dB_1 = \frac{-\mu_0 Jr dr d\theta \cos \theta}{2\pi r}$$

$$B_1 = \frac{-\mu_0 J}{2\pi} 2 \int_{-\alpha}^{\alpha} \cos \theta d\theta \int_{R_{in}}^{R_{out}} \frac{r dr}{r} \quad (2.53)$$

$$B_1 = \frac{-2\mu_0 J}{\pi} (R_{out} - R_{in}) \sin \alpha$$

In the above relations α is half of the angular width of the sector coils, R_{out} is the outer radius, and R_{in} is the inner radius where the difference of these radii is the radial width of the sector coil and is important for estimating the volume, mass, and cost of copper used in the coil. As can be seen from Eq. 2.53, for a dipole magnet the main field B_1 is proportional to the current density and the radial width of the coil and is independent of its internal radius. We know from Section 2.2.1 the allowed higher order multipoles for dipoles are $n = 3, 5, 7, \dots, (2n+1)$ and we can calculate these terms starting

by Eq. 2.47 as follows.

$$\begin{aligned}
 B_n &= \frac{-\mu_0 I}{2\pi} R_{ref}^{n-1} \Re\left(\frac{1}{z_0}\right)^{n-2} \\
 dB_n &= \frac{-\mu_0 J r dr d\theta}{2\pi} R_{ref}^{n-1} \Re\left(\frac{e^{-i\theta}}{z_0}\right)^{n-2} \\
 B_n &= \frac{\mu_0 J R_{ref}^{n-1}}{\pi} \frac{2 \sin n\alpha}{n} \frac{(R_{out}^{2-n} - R_{in}^{2-n})}{2-n} \\
 B_n &= \frac{2\mu_0 J R_{ref}^{n-1}}{\pi} \frac{(R_{out}^{2-n} - R_{in}^{2-n})}{n(2-n)} \sin n\alpha
 \end{aligned} \tag{2.54}$$

Considering $\alpha = 60^\circ$, the sextupolar field B_3 is zero, and the first multipolar error is related to the ten-pole field B_5 , which is almost a hundred times larger than the allowable limit. As can be seen from Eq. 2.54, coils with a width much larger than the inner radius $R_{out} \gg R_{in}$, naturally have small multipolar errors. Therefore, in order to optimize the field quality, more degrees of freedom should be considered. For this purpose, two layers of segmental windings with the same width and different angular widths α_1 and α_2 are used to zero the sextupole and tenth-pole components at the same time, see Fig. 2.24, left. Superimposing the fields of these two layers, considering $R_{in} = r$, $R_{out} = r + w$ for the first layer and $R_{in} = r + w$, $R_{out} = r + 2w$ for the second layer, using Eq. 2.54 one can write the sextupole and tenth-pole field components as follows,

$$\begin{aligned}
 B_3 &\propto \sin(3\alpha_1) \left(\frac{1}{r+w} - \frac{1}{r}\right) + \sin(3\alpha_2) \left(\frac{1}{r+2w} - \frac{1}{r+w}\right) = 0 \\
 B_5 &\propto \sin(5\alpha_1) \left(\frac{1}{(r+w)^3} - \frac{1}{r^3}\right) + \sin(5\alpha_2) \left(\frac{1}{(r+2w)^3} - \frac{1}{(r+w)^3}\right) = 0
 \end{aligned} \tag{2.55}$$

Also by adding one wedge to the first layer and having three free parameters α_1 , α_2 and α_3 one can diminish the fourteenth-pole component too, (see Fig. 2.24, right and [29]).

In order to better understand and compare the intensity of the magnetic field caused by coils with the same radial width(w) and different layout (number of layers, angles, and number of wedges), the coefficient γ_0 for each layer is defined according to the following relation:

$$B = \gamma_0 w J, \tag{2.56}$$

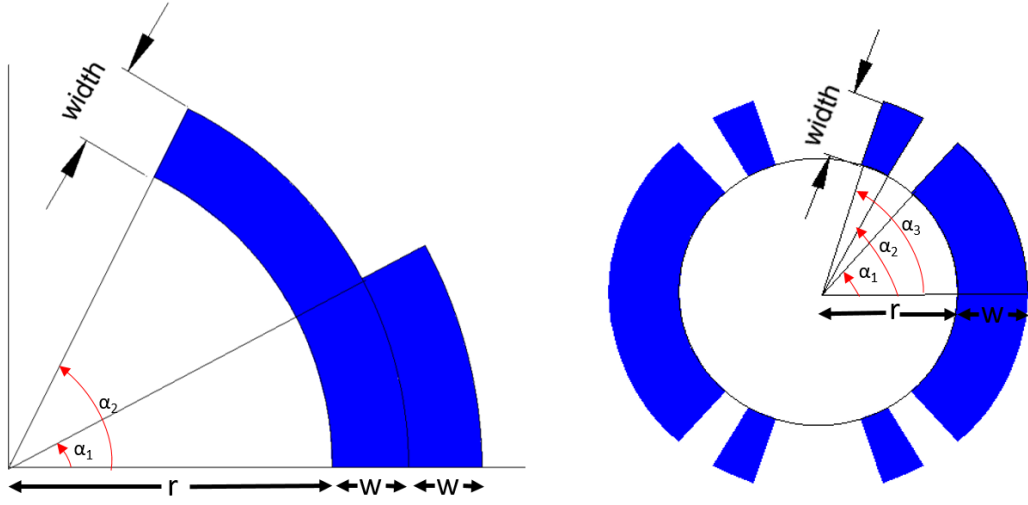


Figure 2.24.: Layout of dipolar coils, one-layer with one wedge (right) and two-layer with no wedges (left).

where for one layer coil with angular width $\alpha = 60^\circ$,

$$\gamma_0 = \frac{2\mu_0}{\pi} \sin \frac{\pi}{3} \approx 6.9 \times 10^{-7} \text{ T.m.A}^{-1} \quad (2.57)$$

In order to find the coefficient γ_0 for different configurations of coil sectors and wedges, the resulting fields for individual sectors using Eq. 2.52 should be calculated and added up. Then by comparing the field with Eq. 2.56, the coefficient γ_0 and specifications for different common coil layouts can be summarized in Table 2.3.

2.3.2. Quadrupoles

Considering the sector coil layout for an air-core quadrupole, as shown in Fig. 2.23 and Eq. 2.47 for $n = 2$ we can define the field gradient g as follows

$$B_2 = \frac{-\mu_0 I R_{ref}}{2\pi} \Re\left(\frac{1}{z^2}\right), \quad z = r e^{i\theta} \quad (2.58)$$

$$g = \frac{B_2}{R_{ref}} = \frac{-\mu_0 I \cos 2\theta}{2\pi r^2}$$

Switching to the polar coordinates, $I = J r dr d\theta$; considering R_{in} as the sector coil inner radius and $R_{out} = R_{in}(r) + w$ (coil width), field gradient can be

Table 2.3.: Different angular layouts for air-core dipole, canceling the first allowed harmonics.

Layout	No.wedges	Angular width	γ_0	Zero harmonics
$[0^\circ - 60^\circ]$	0	60°	6.928E-7	B_3
$[0^\circ - 48^\circ, 60^\circ - 72^\circ]$	1	60°	6.625E-7	B_3, B_5
$[0^\circ - 24^\circ, 36^\circ - 60^\circ]$	1	48°	5.480E-7	B_3, B_5
$[0^\circ - 36^\circ, 44^\circ - 64^\circ]$	1	56°	6.335E-7	B_3, B_5
$[0^\circ - 43.2^\circ, 52.2^\circ - 67.3^\circ]$	1	58.3°	6.535E-7	B_3, B_5
$[0^\circ - 33.3^\circ, 37.1^\circ - 53.1^\circ, 63.4^\circ - 71.8^\circ]$	2	57.7°	6.411E-7	B_3, B_5, B_7

derived by integrating over the sector coil;

$$\begin{aligned}
 dg &= \frac{-4\mu_0 J r dr d\theta \cos 2\theta}{2\pi r^2} \\
 g &= \frac{-4\mu_0 J}{2\pi} \int_{-\alpha}^{\alpha} \cos 2\theta d\theta \int_{R_{in}}^{R_{out}} \frac{r dr}{r^2} \\
 g &= \frac{-2J\mu_0}{\pi} \ln \frac{R_{out}}{R_{in}} \sin 2\alpha = \gamma_0 J \ln \frac{R_{out}}{R_{in}} \\
 g &= \gamma_0 J \ln \frac{r+w}{r} = \gamma_0 J \ln \left(1 + \frac{w}{r}\right)
 \end{aligned} \tag{2.59}$$

Where

$$\gamma_0 = \frac{-2\mu_0}{\pi} \sin 2\alpha \tag{2.60}$$

Therefore, the gradient is proportional to the current density and to the natural log of one plus the ratio of the coil width and the magnet aperture [29]. Also, the higher-order multipoles can be obtained in the same way as

dipoles.

$$\begin{aligned}
B_n &= \frac{-\mu_0 I}{2\pi} R_{ref}^{n-1} \Re\left(\frac{1}{z_0}\right)^{n-2} \\
dB_n &= \frac{-\mu_0 J r dr d\theta}{2\pi} R_{ref}^{n-1} \Re\left(\frac{e^{-i\theta}}{z_0}\right)^{n-2} \\
B_n &= \frac{\mu_0 J R_{ref}^{n-1}}{\pi} \frac{4 \sin n\alpha}{n} \frac{(R_{out}^{2-n} - R_{in}^{2-n})}{2-n} \\
B_n &= \frac{4\mu_0 J R_{ref}^{n-1}}{\pi} \frac{(R_{out}^{2-n} - R_{in}^{2-n})}{n(2-n)} \sin n\alpha
\end{aligned} \tag{2.61}$$

Looking at the Eq. 2.61, for $\alpha = 30^\circ$ multipole corresponds to the B_6 , $n = 6$, is zero and the first allowed multipole is B_{10} , the twentieth-pole field. Therefore, in this case, it is also necessary to consider more degrees of freedom in order to suppress the higher-order multipoles. For this purpose, methods such as multi-layer winding layout and adding wedges, which were discussed in detail in the dipole Section 2.3.1, are used. Adding layers and wedges to diminish B_6 and B_{10} yields similar results as dipoles which means any angular solution for a dipole canceling the first n allowed harmonics will also cancel the first n allowed quadrupolar harmonics, provided that angles should be divided by a factor of 2, [31]. The coefficient γ_0 and specifications for different common coil layouts can be summarized in Table 2.4

2.4. Magnetic measurement

To determine the validity of the magnet design and ensure the qualified operation of the magnets, usually it is recommended to do a magnetic measurement for a prototype magnet before going to the series production. Then according to the obtained measurement results, the necessary changes will be applied to the design or fabrication procedure of the magnet. There are several magnetic measurement methods, like the Hall probe, Nuclear Magnetic Resonance (NMR), stretched wire, and rotating coil method which is an accurate method for measuring multipole components, especially in magnets with circular apertures like quadrupoles and sextupoles, [32]. The best method for an application is selected depending on parameters such as the size of the magnet aperture, field intensity, field homogeneity, and required accuracy. In this thesis, a Hall sensor was used to measure the

Table 2.4.: Different angular layouts for air-core quadrupole, canceling the first allowed harmonics.

Layout	No.wedges	Angular width	γ_0	Zero harmonics
$[0^\circ - 30^\circ]$	0	30°	6.928E-7	B_6
$[0^\circ - 24^\circ, 30^\circ - 36^\circ]$	1	30°	6.625E-7	B_6, B_{10}
$[0^\circ - 12^\circ, 18^\circ - 30^\circ]$	1	24°	5.480E-7	B_6, B_{10}
$[0^\circ - 18^\circ, 22^\circ - 32^\circ]$	1	28°	6.335E-7	B_6, B_{10}
$[0^\circ - 21.6^\circ, 26.1^\circ - 33.7^\circ]$	1	29.2°	6.535E-7	B_6, B_{10}
$[0^\circ - 16.7^\circ, 18.6^\circ - 26.6^\circ, 31.7^\circ - 35.9^\circ]$	2	28.9°	6.411E-7	B_6, B_{10}, B_{14}

magnetic field in the experimental work so in the following the Hall probe measurement method is reviewed in more detail.

2.4.1. Hall probe

A Hall probe is a semiconductor suitable for point-to-point field measurements. If no magnetic field is applied, the charge carriers in the semiconductor move parallel to the external electric field. Under the influence of the external magnetic field, the charge carriers are separated from each other and the Hall voltage is produced according to the applied current and magnetic field, Fig. 2.25. The Hall generator is mainly sensitive to a component of the magnetic field that is perpendicular to the plane of the probe (shown as the x-y plane), This generator is usually made of n-type semiconductors such as InSb (Indium Antimonide), and InAs (Indium Arsenide) with high electron mobility. To derive the relation between the Hall voltage and applied magnetic field it should be noticed that by applying an external magnetic field to a current-carrying Hall sensor, the electrons with the velocity v_e encounter the Lorentz force F_L

$$\vec{F}_L = -e(\vec{E} + \vec{v}_e \times \vec{B}), \quad (2.62)$$

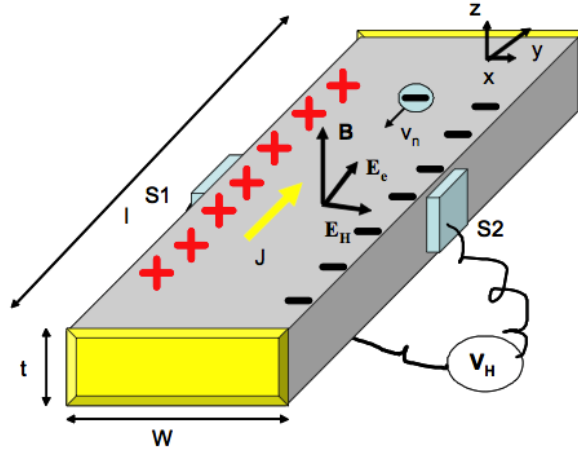


Figure 2.25.: Sketch of a Hall generator, consists of a thin semiconductor plate of length l , width w , and thickness t .

Under this Lorentz force, the electrons are pushed by the magnetic force toward the edge of the semiconductor plate. As a consequence of this charge separation, an electric field is induced across the plate which is defined by

$$\vec{E}_H = \vec{v}_e \times \vec{B} \quad (2.63)$$

Therefore, the Hall voltage V_H across the width of the semiconductor plate, w , can be calculated by the integral of the electric field as follows

$$V_H = \int_{S_1}^{S_2} \vec{E}_H dw = \frac{-J}{n_e} Bw \quad (2.64)$$

where the current density is $J = I/wt$, n_e is the density of electrons and t is the thickness of the plate. So, the Hall voltage can be defined as a function of the current and the magnetic field

$$V_H = \frac{R_H}{t} IB \quad (2.65)$$

where $R_H = -1/n_e$ is the Hall coefficient, [33]. The main limitation to the accuracy of the Hall probe is the temperature dependence of the Hall voltage. This problem can be reduced by temperature control or by calibrating the sensor. Other limitations include the sensitivity to the field components in the Hall plane, often referred to as the planar Hall effect, and the non-linearity of the calibration curve, [34]. The Hall probe is a useful tool for local mapping of the magnetic field. However, field mapping is time-consuming, and not accurate enough when field integrals are required. For

Table 2.5.: Critical temperatures for Various Superconductors.

Material	T_c (K)
Zn	0.88
Al	1.14
Sn	3.72
Pb	7.9
Nb-Ti	9.46
Nb ₃ Sn	18.05
Nb ₃ Ge	23.20
YBa ₂ Cu ₃ O ₇	92
Bi-Sr-Ca-Cu-O	105
Tl-Ba-Ca-Cu-O	125
HgBa ₂ Ca ₂ Cu ₃ O ₈	134

this reason, integral measurement methods like stretched wire or rotating coil are used.

2.5. Superconductivity in magnets

Superconductivity is a physical property of a material that manifests itself in vanishing electrical resistivity as well as the expulsion of the magnetic field at temperatures below a certain cryogenic temperature T_c . This phenomenon was first discovered in 1911 by Heike Kammerlingh Onnes when he passed a current through a very pure mercury wire and measured no resistance at temperatures less than 4.2 K. Using coils wound of superconducting wires leads to very high current densities, up to 2000 A mm^{-2} , and strong magnetic fields up to 20 T, whereas normal conducting magnets due to ohmic loss and cooling issues can tolerate only up to 10 A mm^{-2} current density and generate usually up to 2 T magnetic fields. To make use of these benefits, long-term research has led to finding superconductivity in many elements and compounds with different critical temperatures, T_c . Table 2.5 shows critical temperatures for various superconductors [35] and [31].

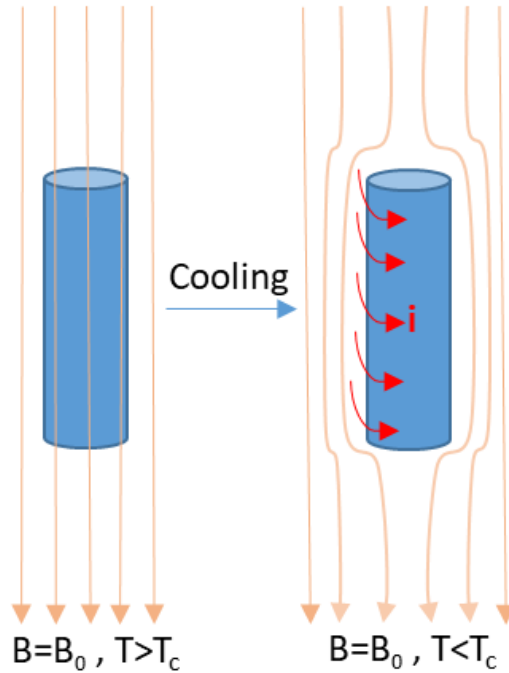


Figure 2.26.: Meissner effect: the expulsion of the magnetic flux inside a superconductor due to the induced surface current at $T < T_c$ and non-changing external field.

2.5.1. Superconductors Type I and Type II

Expelling an external magnetic field at temperatures below the critical temperature is one of the main characteristics of superconducting materials and is called the Meissner effect. To understand the Meissner effect, one can see what happens to a perfect conductor when it is cooled down to temperatures less than its critical temperature, starting with Ohm's law

$$I = \frac{\Delta V}{R} \quad (2.66)$$

In a perfect conductor with $R \approx 0$, the potential difference and thus the electric field E inside the material is zero. Also according to Faraday's law, Eq. 2.67, since E is zero everywhere inside the material and the integral of E over any closed path inside is zero, $d\Phi_B/dt = 0$.

$$\begin{aligned} \Delta \times E &= -dB/dt \\ \text{Stokes' theorem } \oint_C E \cdot dl &= -d\Phi_B/dt \end{aligned} \quad (2.67)$$

This indicates that the magnetic flux in any cooled perfect conductor cannot change and therefore magnetic field, $B = \Phi_B/A$, must remain constant inside. It also means that if the perfect conductor is cooled down in the presence of an external magnetic field, the field is trapped inside even for $T < T_c$. For superconductors, however, in contrast to an ideal conductor, at $T < T_c$, there is always a surface current that makes the magnetic field inside zero even if the external field has been applied before cooling the material. This surprising characteristic of the superconductors cannot be explained by the law of induction due to having a constant magnetic field before and after the cooling and is the so-called Meissner effect, Fig. 2.26.

Superconductors that exhibit the complete Meissner effect like mercury, lead and aluminum are named Type I or soft superconductors while those which exhibit an incomplete Meissner effect, which in other words admit a partial penetration of magnetic flux, such as Nb-Ti, Nb₃Sn, and ReBCO (Rare earth Barium Copper Oxide), are called Type II or hard superconductors [35].

Type II superconductors have two critical magnetic fields B_{c1} and B_{c2} . For temperatures well below the critical temperature and at external fields lower than the B_{c1} , the material stays completely in the superconducting state and shows the complete Meissner effect as Type I superconductors. At external fields between B_{c1} and B_{c2} , a mixture of normal conducting and superconducting states appear, the so-called Shubnikov phase, which is characterized by the formation of magnetic field vortices. The vortex density increases with increasing field strength. At fields higher than the critical field B_{c2} superconductivity is destroyed, Fig. 2.27.

In spite of zero resistivity below the critical temperature, superconductors can carry only a limited amount of current, I_c which also depends on the temperature T and magnetic field B . This current can even become zero if the critical magnetic field or the critical temperature is reached. Figure 2.28 depicts the phase diagram for the superconducting phase of type II superconductors.

2.5.2. Low-temperature and high-temperature superconductors

The type-II superconductors are categorized further into Low-Temperature Superconductors (LTS), like Nb-Ti and Nb₃Sn, and High-Temperature Super-

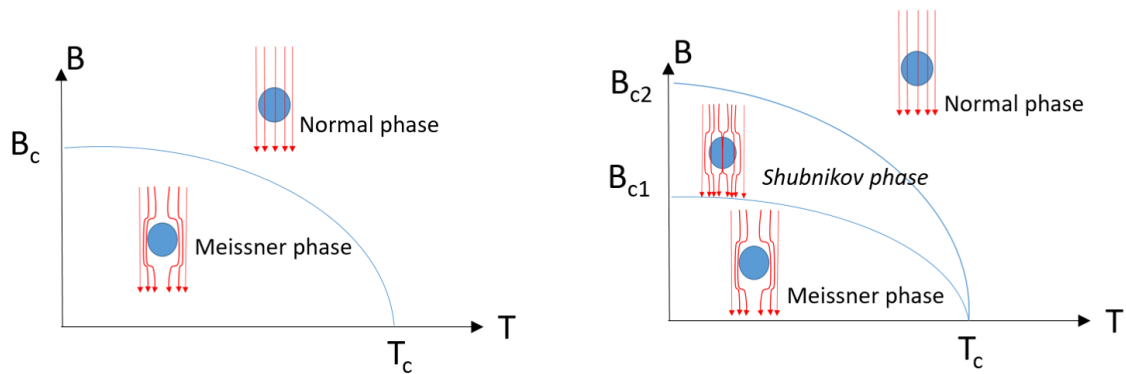


Figure 2.27.: Superconductors Type I (left) and Type II (right).

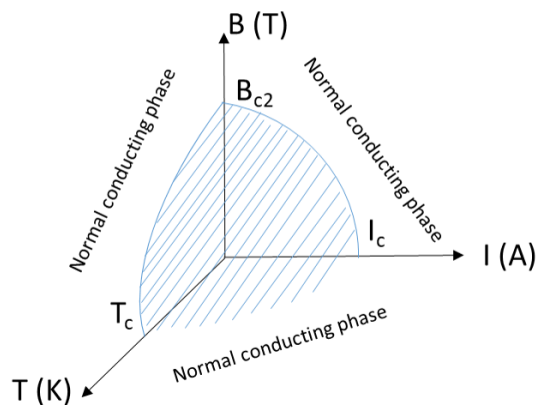


Figure 2.28.: Superconductors type II critical surface given by critical magnetic field B_c , critical temperature T_c , and the critical current I_c forms the limit between the superconducting and normal phases.

conductors (HTS), like ReBCO (rare earth barium copper oxide) or Bi-2212 ($\text{Bi}_2\text{Sr}_2\text{CaCu}_2\text{O}_{6+x}$), based on their critical temperature value with respect to the boiling point of liquid nitrogen, 77 K. The first high-temperature superconductor was discovered in 1986, by IBM researchers Bednorz and Müller, who were awarded the Nobel Prize in Physics in 1987 "for their important breakthrough in the discovery of superconductivity in ceramic materials". All other materials discovered before this were superconducting with critical temperatures near the boiling points of liquid helium or hydrogen (4.2 K and 20 K, respectively), which are both more expensive

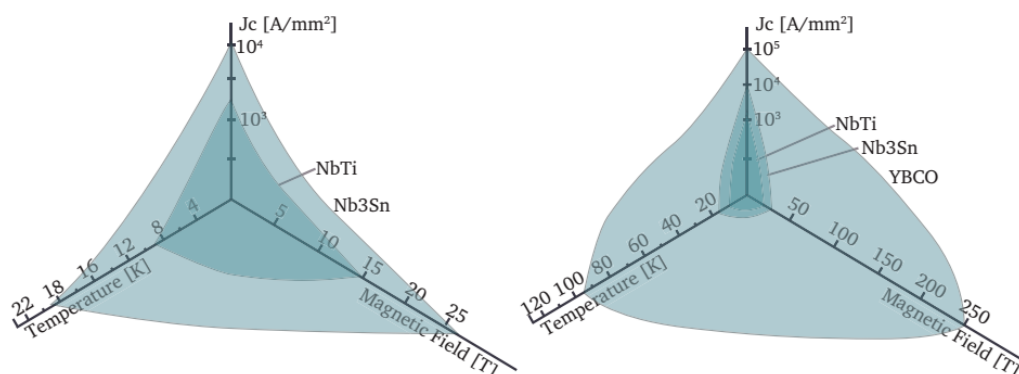


Figure 2.29.: Comparison of the critical surfaces of Nb-Ti and Nb₃Sn, both LTS conductors and ReBCO, HTS conductor [29].

and difficult to obtain than liquid nitrogen. A substance with a critical temperature above the boiling point of liquid nitrogen, together with a high critical magnetic field and critical current density, would greatly benefit technological applications. Figure 2.29 shows the critical surfaces for two common LTS in comparison to high-temperature superconductor ReBCO.

Superconducting coils in accelerators are frequently wound using low-temperature superconductors like Nb-Ti and Nb₃Sn. Nb-Ti is a ductile alloy that makes it easy to deform, while Nb₃Sn is a brittle solid-state compound that makes the fabrication, winding, and handling of wires and coils more complex. Therefore, Nb₃Sn wires are usually applied only if the magnetic fields exceed 9 T and Nb-Ti wires cannot carry the required amount of current. In LTS accelerator magnets, flattened helical cables called Rutherford cables are commonly used. The majority of high-temperature superconductors are ceramic materials and due to the anisotropy and production process of the ceramics, round-wire cabling techniques cannot be used for HTS coils, except for Bi-2212 wires. The conductors are usually in form of flat tapes consisting of a metallic substrate on which a thin film of these ceramics is deposited. In addition to the higher critical temperature, the HTS materials exhibit very high critical magnetic fields and critical current densities, particularly when cooled to lower temperatures. At 4.1 K and fields above 20 T, they perform much better than even the best Nb₃Sn wires. A chart with the current carrying capacity of some practical superconductors is published by P. Lee [36] and shown in Fig. 2.30.

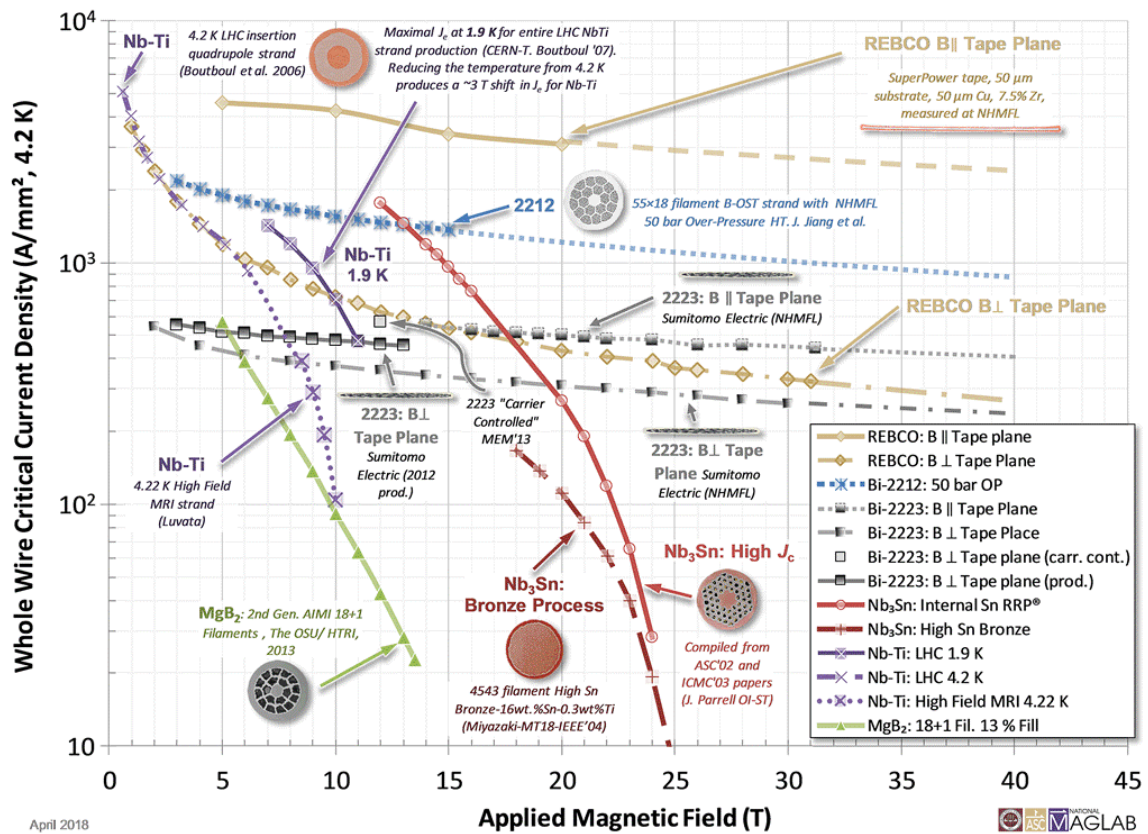


Figure 2.30.: Current carrying capacity of some practical superconductors vs. magnetic field published by P. Lee [36], the author's permission is granted.

2.5.2.1. ReBCO tapes

High-temperature superconductors offer performance advantages and operating space and margins that do not exist with low-temperature superconductors. They are of great interest, especially, in high-field applications (for $B > 23$ T) such as particle accelerators, magnetic confinement fusion, and nuclear magnetic resonance. Indeed, the maximum achievable magnetic field with low-temperature superconductors (LTS) is limited to a value of 23.5 T at 2 K, [37], while using HTS ReBCO coated conductors reaching a magnetic field of 45.5 T was reported for using an HTS insert coil in a resistive magnet, [38]. One of the main characteristics of HTS materials is their anisotropy: the dependency of the critical current on the field orientation with respect to the tape face (angle α), in addition to being a function of temperature and magnetic field *i.e.* $I_c(T, B, \alpha)$. The highest critical current is obtained when the applied magnetic field is parallel to the tape face ($B_{||}$) and the critical current is lowest when the field is perpendicular to the tape

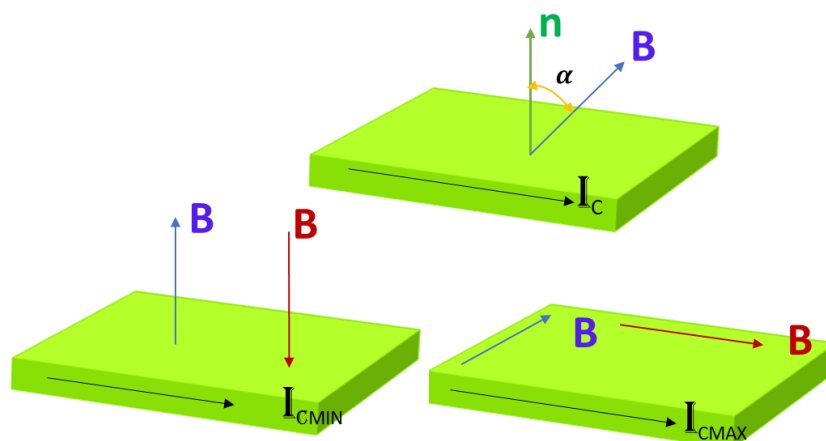


Figure 2.31.: A schematic of the critical current (I_c) dependency to the relative direction of the magnetic field B with respect to the tape face in an HTS tape; field direction has an angle α with the tape face normal (top), perpendicular field (B_{\perp}) to the tape face (bottom-left), and parallel field (B_{\parallel}) with the tape (bottom-right).

face (B_{\perp}), Fig. 2.31. ReBCO tapes in comparison to Bi-2212 have higher J_e , better mechanical robustness, and are more available, especially in Europe. ReBCO tapes are commercially available in different widths of 12, 6, 4, 3, or 2 mm (1.5 mm under development). Figure 2.32 shows the multi-layer structure of a ReBCO-coated conductor. The HTS layer consists of single-crystalline grains coated on a substrate with a thickness of 25 to 100 μm that is commonly made of stainless steel, nickel, or nickel alloy. To improve the epitaxial growth and to provide a chemical barrier between the substrate and the superconducting layer, a stack of buffer layers is deposited on the substrate by various methods like magnetron sputtering, pulsed laser deposition (PLD), and ion-beam-assisted deposition (IBAD) or a combination of these methods, [40]. Superconducting ReBCO is deposited on the buffer layers with a thickness from 1 to 5 μm . This can be done using various deposition methods like MOCVD (Metal-Organic Chemical Vapor Deposition) which is a technology that is used to apply ultra-thin, single-crystal layers to a semiconductor wafer [41]. Using sputtering a few μm layer of silver is coated on top of the ReBCO layer to prevent the chemical reaction of the ReBCO with copper, while this coating also provides an interface to enable copper deposition. Depending on the application, a copper layer of 10 to

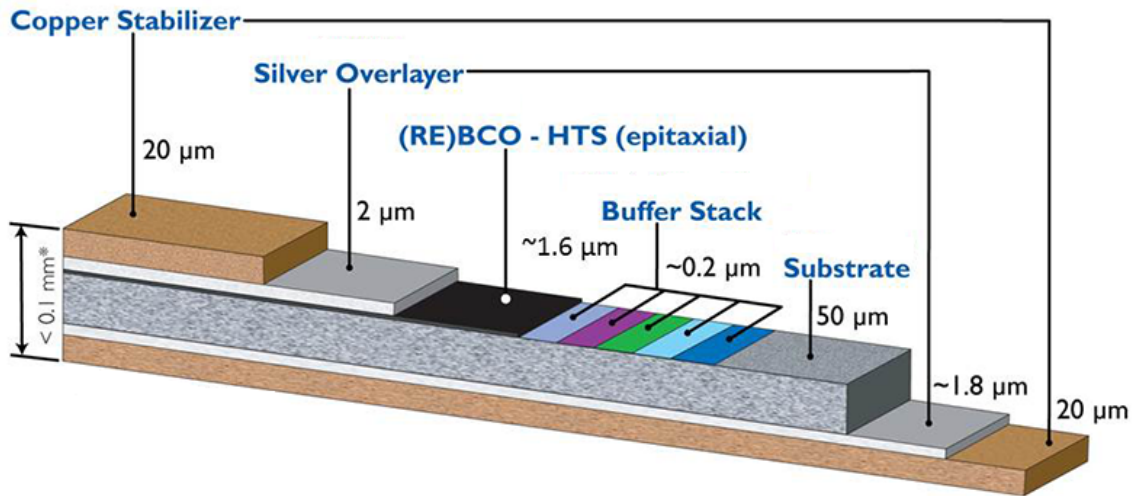


Figure 2.32.: Multi-layer structure of a ReBCO coated- superconducting tape developed by Superpower Inc. [39].

100 μm thickness (5 μm to 55 μm per side) can also be added for additional stabilization. This copper layer can either be soldered onto the tape or formed by electro-deposition. The total conductor thickness is usually kept to be less than 100 μm but in some cases is up to 300 μm .

Long-length production of high-quality HTS has been a challenge for years because the production quality usually decreases exponentially with tape length. In recent years, single-piece REBCO coated conductors have been produced in lengths exceeding 1000 m by Superpower Inc. in the US, [42]. These days, in addition to Superpower Inc., many more companies supply high-quality long-length coated conductors like THEVA Dünnschichttechnik GmbH, Germany [43], Fujikura Ltd, Japan [44], Shanghai Creative Superconductor Technologies, China [45] and SuperOx Japan LLC, [46]. In this thesis, we used 4 mm and 12 mm ReBCO tapes, SCS4050 and SCS12030, from Superpower Inc. for the design and fabrication of the HTS air-core and iron-core magnets, respectively. For more information see chapters 3 and 4.

In order to find the minimum achievable bending radius in ReBCO HTS tapes, different coated conductors from different manufacturers have been tested at 77 K. I_c of each sample was determined by measuring the voltage by ramping up the current until the criterion was reached, using an electric field criterion of 100 $\mu\text{V m}^{-1}$. It was obtained that these tapes behaved

Table 2.6.: Tested samples at 77 K and their parameters, measured critical current I_c , and measured minimum bending radius R_{min} . The minimum bending radius is defined as the smallest radius for which the critical current degrades less than 5%, [47].

Supplier	Reference name	Tape width	Tape thickness	Substrate thickness	Measured I_c	R_{min}
Bruker	-	4 mm	105 μm	50 μm	91 A	10 mm
THEVA	TPL4120	4 mm	80 μm	50 μm	167 A	4 mm
ShanghaiSCT	ST19911-78	10 mm	95 μm	50 μm	360 A	7 mm
ShanghaiSCT	ST1910-19	4 mm	95 μm	50 μm	159 A	2.5 mm
SuperOx	942-R	4 mm	76 μm	60 μm	127 A	5 mm
SuperPower	SF12050-AP	12 mm	55 μm	50 μm	428 A	4 mm
SuperPower	SCS4050-AP	4 mm	100 μm	50 μm	135 A	4 mm
SuperPower	SCS4030-AP	4 mm	42 μm	30 μm	130 A	2 mm
SuperPower	SCS4025-AP	2 mm	36 μm	25 μm	65 A	2 mm

mainly according to their substrate thickness. Overall, a thinner substrate decreases the minimum bending radius, Table 2.6 and [47].

2.5.2.2. Roebel cable

In the investigations to reduce the AC losses in large generators, a low-loss assembled copper cable was designed by Ludwig Roebel in 1914 [48]. His design was based on segmenting the conductor into insulated strands that are transposed along the cable direction. Because of the good ductility of Nb-Ti, the first superconducting Roebel cable was made from Nb-Ti insulated strands in EURATOM project magnet [49] and later at CERN [50]. The first high-temperature superconducting Roebel cable was developed at Siemens AG, Germany, using 13 strands of Bismuth strontium calcium copper oxide (BSCCO) coated conductors [51]. Because of the restricted in-plane bending capability of the material, the transposition length was as long as 3 m which was long enough for the rotating machines. Developments in the coated conductors technology years after led to a meander-like shaping of the coated conductors first patented by Martino Leghissa from Siemens AG. in

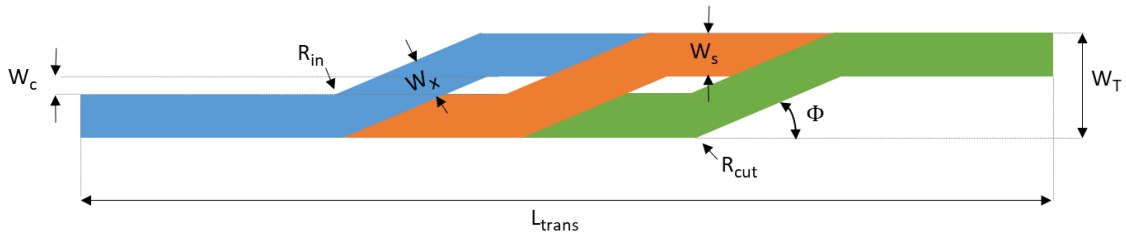


Figure 2.33.: Roebel cable geometrical parameters of the punched meandering pattern.

2002 [52] and later presented and realized by Wilfried Goldacker in 2005-2006 at Karlsruhe Institute of Technology, KIT [53, 54]. In this, the Roebel cables are prepared by precise punching of the ReBCO-coated conductors in a meandering shape. The geometrical parameters of the punched pattern are depicted in Fig. 2.33. In the above figure, W_T is the tape width, L_{trans} is the transposition length that is a full period of the meander, W_s is the strand width, W_c is the strand-edge clearance, W_x is the crossover width, Φ is the crossover angle, R_{cut} the cut-off fillet radius and R_{in} and the inner radius [55]. Due to its high current density and full transposition, Roebel cables have been recently used in the EuCARD2 project. In this project dipole magnets using an aligned block coil (CERN) [56] and the cos-theta coil (CEA) [57] have been designed and realized to work at 5 T and liquid helium temperature, 4.2 K.

2.6. Laser Plasma Acceleration

As it was discussed before, in this thesis the focus is on designing the miniature HTS magnets for capturing the Laser-Plasma generated electron beams. So far the required general concepts for designing iron-core and air-core magnets and considerations of using superconducting coils, especially the HTS ones, were discussed. Now to cover all the aspects of the project a brief overview of the Laser Plasma acceleration concept is also given in this section. Particle acceleration in Plasma was first proposed by Tajima and Dawson In 1979 [58] for laser-driven wakefields (LWFA) and in 1985 by P Chen, J M Dawson et al. [59] for Particle driven wakefields (PWFA). Plasma accelerators are steadily matured by developments in generating ultrashort duration high-current electron bunches and high-power, ultrashort-pulsed

lasers [60, 61, 62, 63]. In accelerators the drive beam, whether a laser or particle beam, generates a plasma ‘wake’ with a phase velocity close to the speed of light. This wake separates the electrons and ions in the plasma through a ponderomotive force, Eq. 2.68, and leads to strong longitudinal electric fields that accelerate trapped charged particles to relatively high energies of several hundred MeV to a few GeV in a few centimeters. The ponderomotive force is given by

$$F_{pon}^{\vec{}} = \frac{-m_e c^2}{2} \nabla(a^2), \quad (2.68)$$

where a is the laser strength parameter, defined as the peak amplitude of the normalized vector potential of the laser field, $\vec{a} = e\vec{A}/m_e c^2$, and m_e is the electron rest mass, [64]. The ponderomotive force, which is proportional to the gradient of the laser strength parameter pushes plasma electrons outward and separates them from the ions. The associated electrostatic field pulls electrons back, resulting in electron oscillations with the plasma frequency behind the laser pulse, Eq. 2.69, as schematically depicted in Fig. 2.34.

$$\omega_p = \sqrt{\frac{4\pi n_0 e^2}{m_e}}, \quad (2.69)$$

where n_0 is the plasma density.

Moreover, the electric field which can be endured in ionized plasma is

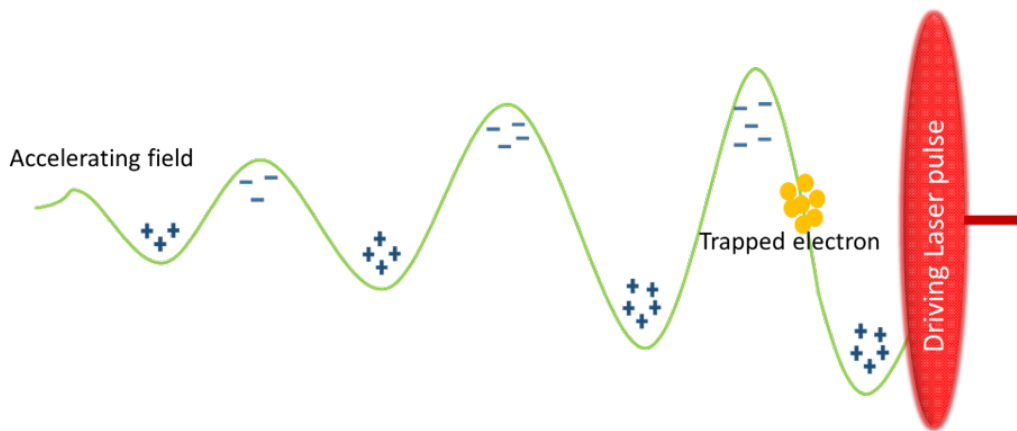


Figure 2.34.: Schematic sketch of an LPA acceleration process.

proportional to the plasma density and can be approximated by [64, 65]

$$E_0\left(\frac{V}{m}\right) = \frac{cm_e\omega_p}{e} = 96\sqrt{n_0(cm^{-3})}. \quad (2.70)$$

Thus, for a plasma density of $n_0 = 10^{18} \text{ cm}^{-3}$, the plasma electric field will be $E_0 = 96 \text{ GV m}^{-1}$, which is approximately three orders of magnitude greater than that obtained in conventional linear accelerators. In addition to the high accelerating gradients, LPAs can produce short electron bunches, as the length of the accelerating wave is approximately the plasma wavelength

$$\lambda_p(\mu\text{m}) = \frac{2\pi c}{\omega_p} = \frac{3.3 \times 10^{10}}{\sqrt{n_0(cm^{-3})}} \quad (2.71)$$

So, for the previous case of $n_0 = 10^{18} \text{ cm}^{-3}$ we have $\lambda_p = 33 \mu\text{m}$ which leads to the bunch length of $\tau_b < 100 \text{ fs}$.

One of the main aims of the LPA research is to make these accelerators capable of feeding free electron lasers (FELs). To increase the FEL gain and shorten the wavelength of operation, it is needed to have an excellent beam quality for the hard x-ray domain (nC charge level, 0.01% energy spread, $1 \pi\text{mm mrad}$ emittance). Although using concepts like TGU and/or using decompression/slice energy spread reduction can help in spite of not having that perfect beam quality in LPAs. Recently, FEL amplification with LWFA beams has been proven experimentally at Shanghai [66]. Also at COXINEL in Paris, a proper transport of LPA-generated beams was reported in 2021 by using strong permanent quadrupoles to handle the electron beam divergence, a magnetic chicane to reduce the energy spread, and set of quadrupoles for adjusting the focusing inside the undulator [67].

3. HTS air-core transport line

Laser plasma accelerators can generate several GeV electron beams in few cm length. This high energy, but large-energy spread and fairly divergent beams, need to be transported in a well-controlled way through the undulators to generate high-quality, short wavelength radiations. so we require short focal length focusing elements like high-strength quadrupoles which also should be short in length to provide focusing in both transverse planes over a small distance. After capturing the electron beam through the quadrupole triplet/doublet, it is necessary to transport the beam in a dispersive section that can match the beam properties to the geometrical and dynamical acceptance of, e.g., a transverse gradient undulator, TGU. To achieve this goal, an air-core transport line with compact, high-temperature superconducting (HTS) magnets is planned to be designed. In this transport line, the magnets are based on the $\cos \theta$ coils using ReBCO tapes, see Section 2.3.1, 2.3.2 and 2.5.2.1. These magnets can produce much higher fields than iron-core ones and make it possible to capture and guide the electron beams at higher energies. The main disadvantage of using cos-theta HTS coils in air-core magnets is the limited mechanical properties of HTS ceramic-structured superconductors which leads to many manufacturing issues during the coil winding process. Although in this thesis it is tried to minimize the strain and stresses on the coils by modifying the coil ends, Section 3.2.1.2.

So, by using cos-theta high-strength quadrupoles and combined dipoles and implying high current densities to the HTS coils at liquid Helium temperature, the 700 MeV electron beam is caught in a short distance while achieving the transverse gradient undulator input requirements at the end of the transport line, see Section 3.1.1. In this chapter beam dynamics simulation as well as air-core magnets' design is discussed.

Table 3.1.: Start parameters for the beam transport line design.

Parameter	Unit	Value
Source size	μm	4.0
Source divergence	mrad	2.5
Bunch length	μm	1.0
Geometrical emittance	$\pi\text{nm rad}$	10.0
$\beta_{x,y}$	mm	1.6
$\alpha_{x,y}$	-	0.0
Total charge	nC	1.0

3.1. Beam dynamics

Due to extremely high accelerating gradients in LPAs, electron bunches can gain sufficient energies to generate synchrotron radiation in the X-ray regime in only a few millimeters to centimeters of acceleration length. To efficiently capture and transport the LPA-generated bunches in a compact transport line, beam line designs using OPA [68], elegant(ELEctron Generation And Tracking) [69] and ASTRA [70] have been studied.

3.1.1. Parameters and requirements

To start the beam transport line design one should have the start parameters of the particle beam which are the parameters of the beam emitted by the LPA. In this thesis, I considered a Gaussian beam with the start parameters as estimated by C. Widmann [7], Table 3.1. In the above table, source size is the size of the electron bunch inside the plasma which can be measured by analysis of the emitted radiation in the plasma during the acceleration process, betatron radiation [71]. Also, emittance at the LPA can be measured using different methods like the pepper pot method [72, 73], or via a quadrupole scan [74]. Since a beam waist at the exit of the LPA is assumed, $\alpha_{x,y} = 0$, the geometrical emittance, from Eq. 2.24, is obtained by the product of the source size and the source divergence, *i.e.* $10\pi\text{nm rad}$. Moreover, the beam parameters at the end of the transport line should match the radiation source entrance parameter, here I consider the Transverse Gradient Undu-

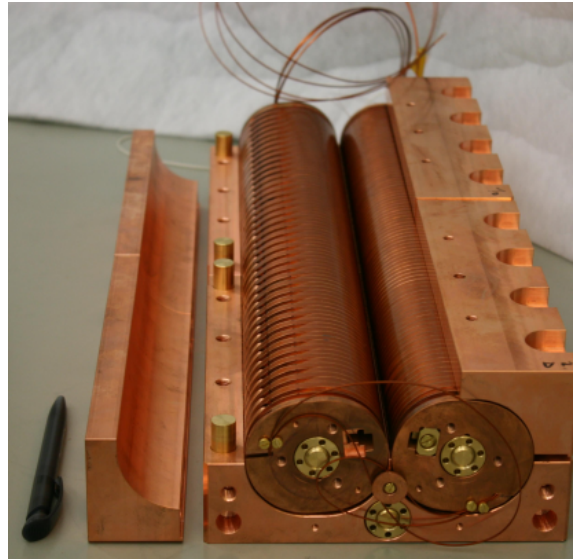


Figure 3.1.: Transverse Gradient Undulator (TGU) [6].

lator (TGU) as the radiation source. Figure 3.1 shows the TGU designed and developed at Karlsruhe Institute of Technology and as can be seen in Eq. 3.1, the magnetic field on the transverse plane has a gradient and is matched to the spatial dispersion of the electrons. So the particles with different energies oscillate at the same amplitude and frequency which leads to narrow spectrum radiation, more information can be found in [6] and [75].

$$\lambda = \frac{\lambda_u}{2\gamma^2(x)} \left(1 + \frac{K_u^2(x)}{2} \right), \quad K_u(x) = \frac{-eB_0(x)}{m_0c} \frac{\lambda_u}{2} \quad (3.1)$$

To match the beam parameters to the TGU requirements, according to the analysis of the beam shape along the TGU which has been done by C. Widmann [7], it is assumed that there is a beam waist at the center of the undulator with $\beta_x \approx 0.2$ m, dispersion D is equal to 20 mm and dispersion gradient D' is considered to be zero at the entrance and the center of the TGU.

3.1.2. Layout and simulation results

Having the start and end parameters of the particle beam, a compact beam transport line using high-strength combined function magnets was designed as a modification of the normal conducting transport line by C. Widmann [7] and M. Ning [8]. C. Widmann designed a 2.5 m long, normal conducting

3. HTS air-core transport line

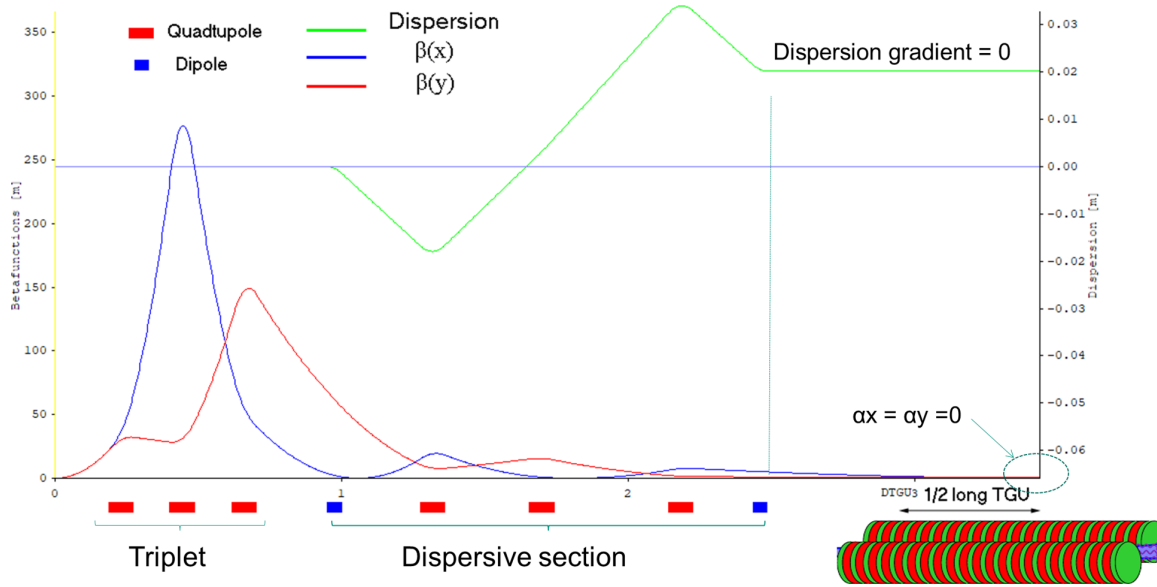


Figure 3.2.: Magnet layout and beam optic parameters along beam trajectory at 300 MeV for the normal conducting transport line, [8].

layout of magnets at 120 MeV energy. This beam transport line consists of a triplet, three quadrupoles, to capture the electron beam and a dispersive section, in which three quadrupoles are located between two dipoles with opposite bending directions, to match the beam parameters to the TGU requirements. M. Ning modified the mentioned transport line by using the same layout but higher strength normal conducting quadrupoles. Keeping the same transport line length, the energy is increased from 120 MeV to 300 MeV. The layout and the resulting optical functions are shown in Fig. 3.2, [8, 76]. In this thesis, different transport lines using HTS magnets have been studied. Inserting initial beam conditions, several layouts with different magnets' lengths and strengths as well as different drift spaces have been investigated. In the two best results, in which the transport lines are more compact and the Twiss parameters at the end of the transport lines match better to the TGU input parameters, the designed beam energy increased to 700 MeV at 1.67 m and 1.4 m length for triplet-based and doublet-based designs, respectively. Detailed information about the beam dynamic and magnet designs of these transport lines is brought in the following sections. Also, it should be noted that the magnets' given parameters, dipoles deflecting angle (φ), quadrupole strength (k), and sextupole strength (m), are based on the before-mentioned equations 2.6, 2.13

and 2.14.

Dipole fields and the field gradients of the quadrupoles are limited by the maximum current density that can be carried by the HTS coils. According to the tests and experiments which were done by C. Barth [77] on ReBCO tapes from different suppliers, the current density of 2000 A mm^{-2} can be well tolerated in most of the cases at the liquid helium temperature 4.2 K and the parallel fields below 19 T. In this thesis, for the magnet coils which are operated at 4.2 K and the field of 6 T, I chose a 4 mm wide ReBCO tape (SCS4050) from Superpower Inc., this HTS tape has a $50 \mu\text{m}$ substrate thickness and $20 \mu\text{m}$ copper stabilizer on each side. In order to be on the safe side and keep good margins, especially in air-core magnets with winding complications, I used a maximum current density of 1500 A mm^{-2} that gives a field gradient of 550 T m^{-1} for the triplet quadrupoles. So using Eq. 2.13, in case of $E = 700 \text{ MeV}$ the upper limit for k is 235 m^{-2} .

3.1.2.1. Triplet-based design

In order to design the beam transport line, I used the start parameters of the LPA source as it was discussed in Section 3.1.1. So by considering a beam waist $\alpha_{x,y} = 0$ and $\beta_{x,y} = 0.0016 \text{ m}$ at the start (the source position), I optimized a linear beam transport layout in a way to match the TGU required parameters. I started from C. Widmann's designed layout [7], considered a triplet and a dispersive section, and tried to make the transport line more compact by using combined-function magnets, reducing the number of magnets as well as lessening the magnet lengths and drift spaces between the magnets.

Magnet parameters for the designed triplet-based transport line are brought in Table 3.2. In this transport line, as is shown in Fig. 3.3, the beam from the laser plasma accelerator is collimated by passing through the three quadrupoles. The first quadrupole Q_1 is located close to the source at a distance of 16 cm, to keep the β function small. This first quadrupole is defocusing, it defocuses the beam in the x-plane and focuses it in the y-plane. So to capture the beam in the horizontal direction a focusing quadrupole Q_2 is used close to the first quadrupole. The remaining focusing task will be done by the third quadrupole Q_3 in a way that a beam waist occurred in the first dipole position. Also, the required dispersion is generated through the bending elements D_1 and D_2 in a dispersive section. These dipole magnets

Table 3.2.: Magnet specifications for the triplet-based transport line at 700 MeV.

Magnet	position(m)	Length(m)	Defl.angel(°)	k(m ⁻²)
Q_1	0.163	0.050	-	-59.94
Q_2	0.435	0.050	-	82.74
Q_3	0.692	0.050	-	-66.81
D_1	1.039	0.050	1.5	47.44
Q_4	1.307	0.050	-	-39.24
D_2	1.650	0.050	-1.5	12.85

have a superimposed quadrupole component with the same amount but opposite dipolar field directions, the bending angles of dipoles were adjusted to give the 20 mm dispersion. The lengths of the drifts and quadrupole strengths were further optimized using the built-in matching algorithm of OPA [68].

So, by applying the beam initial conditions, after the second dipole and along the TGU, dispersion is 20 mm, the dispersion gradient is zero and a beam waist at the center of the TGU is achieved. Also using high-strength HTS combined compact magnets leads to a decrease in transfer line length from 2.5 m to 1.67 m [78].

In this transport line, all the magnets have the same length of 50 mm and the highest quadrupole strength is in the second quadrupole Q_2 equal to 82.74 m^{-2} . This means a field gradient of $g = 193 \text{ T m}^{-1}$ at 700 MeV which is 2.8 times less than the considered maximum gradient ($g = 550 \text{ T m}^{-1}$). So it can be deduced that the designed 1.67 m transport line can work for beam energies up to 1.9 GeV although the betatron function in the x -direction, β_x , at the end of the transport line is one order of magnitude less than what is expected at the center of TGU, see Section 3.1.1. Although a shorter, 1.4 m, doublet-based transport line with the beam energy of 700 MeV is developed (see Section 3.1.2.2), due to the ability to serve higher beam energies, it is still worth doing more efforts to upgrade this triplet-based design in future works.

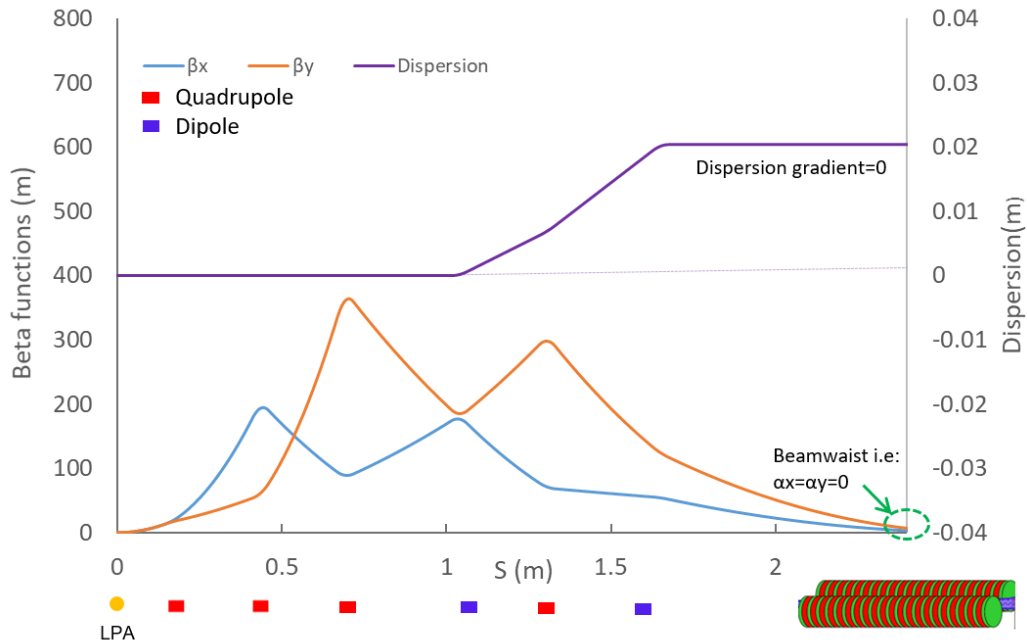


Figure 3.3.: Magnet layout and beam optic parameters along beam trajectory at 700 MeV for the triplet-based HTS transport line design.

3.1.2.2. Doublet-based design

As a modification to the triplet-based design, a transport line with a doublet quadrupole was investigated and developed. Starting from the triplet-based design and omitting the third quadrupole of the triplet, I tried to match the end optical parameters of the new transport line to the input parameters of the TGU. This leads to a decrease in transfer line length from 1.67 m to 1.4 m while fulfilling all the TGU input parameters at the energy of 700 MeV including the $\beta_x = 0.2$ m at the center of the undulator [79]. I used the built-in matching algorithm of OPA [68] and crosschecked the results with the software elegant [69]. In this transport line, as is shown in Fig. 3.4, the beam is collimating by passing through the two doublet quadrupoles. The initial beam conditions are the same as for the triplet-based transport line and the energy is set to be 700 MeV. The first high-strength quadrupole Q_1 is located at a distance of 16 cm from the LPA source, it has a large defocusing effect on the beam in y-plane which is mainly compensated using the defocusing quadrupole Q_2 in a 22 cm distance from Q_1 . There is a beam waist at the center of the first combined-function dipole D_1 which

Table 3.3.: Magnet specifications for the doublet-based transport line at 700 MeV.

Magnet	position(m)	Length(m)	Defl.angel(°)	k(m ⁻²)
Q_1	0.163	0.050	-	216.23
Q_2	0.435	0.050	-	-96.20
D_1	0.782	0.050	1.5	88.06
Q_3	1.050	0.050	-	-39.24
D_2	1.393	0.050	-1.5	12.41

has quite a large focusing quadrupolar strength *i.e.* $k_{D_1} = 88.06 \text{ m}^{-2}$. The second combined-function dipole D_2 has a much smaller superimposed focusing quadrupole component and the same amount of bending field which acts in opposite directions. The third pure defocusing quadrupole Q_3 is placed between the two dipoles, in a way that the electron beam enters the TGU with a constant dispersion of 20 mm while at the center of TGU, the alpha function tends to zero in both planes and Beta function in x direction also fulfill the TGU requirements. Magnet parameters for the designed doublet-based transport line are brought in Table 3.3. As the designed doublet-based transport line is more compact and satisfies the needed end conditions, especially β_x value, better than the triplet-based design, I have done further evaluations like particle tracking and magnet design for this transport line which are discussed in the following sections.

3.1.3. Particle-tracking

In Laser plasma accelerators, large energy spread is a dominant factor to deal with and as it was discussed in Section 3.1.2, to reduce the spectral broadening of the photon beam caused by this energy spread, TGU with a large energy acceptance of $\Delta E/E_0 = \pm 10\%$ (see [80]) has been designed and fabricated. So, the designed transport line should be able to guide the electron beam from LPA to the TGU within this energy range, properly. In the previous section, the Twiss parameters and the optical functions of the designed transport line were discussed. Now using the elegant software [69] phase space parameters x and x' for a single particle at different energies, within $\pm 10\%$ of the central energy (TGU energy acceptance), are investi-

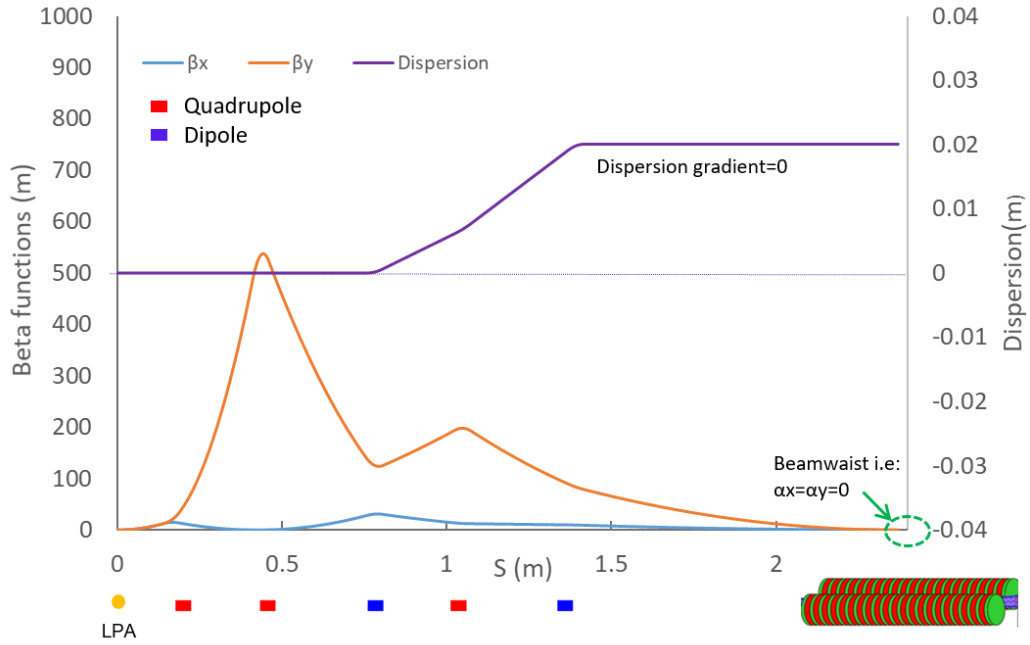


Figure 3.4.: Magnet layout and beam optic parameters along beam trajectory at 700 MeV for the doublet-based HTS transport.

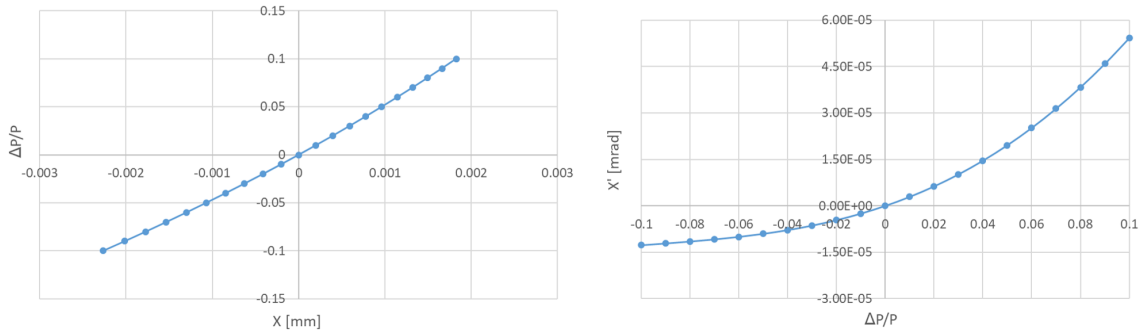


Figure 3.5.: Momentum deviation $\Delta P/P$ versus transverse positions x in mm (left) and divergence x' in mrad (right).

gated. Energy varies 21 times, in 7 MeV steps, from 630 MeV to 770 MeV *i. e.* $\pm 10\%$ energy dispersion, and x and x' versus energy variation has been studied. The results are depicted in Fig. 3.5.

It is derived that for the designed transport line, x has a linear relationship with the energy (momentum) deviations within $\pm 10\%$ and the phase x' does nearly not change with energy (momentum) variations *i.e.* $< 6 \times 10^{-5}$, which fulfills the dispersion requirements. For more detailed calculations

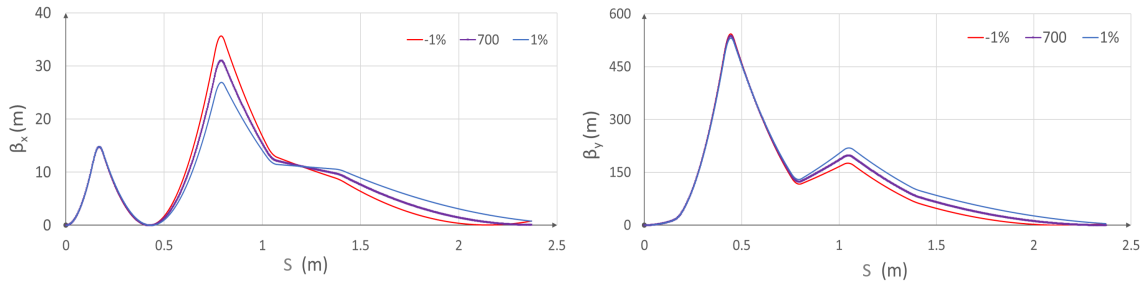


Figure 3.6.: β functions, in x (left) and y (right) planes for different energies up to $\pm 1\%$.

multi-particle tracking was done which gave the phase-space distribution in each energy and the related optical functions. In experimental cases when we power the magnets with a specific current, the field (B) and field gradient (g) are constant parameters. So, the electrons in a bunch with an energy dispersion that are passing through the magnets undergo different field strengths (ρ and k). Therefore to investigate the optical functions for different energies, I considered an electron bunch with specific central energy and zero energy dispersion, then I changed the energy E , quadrupole strength k and the bending radius, ρ , of the dipoles for each energy according to their relation with energy, see equations 2.6, 2.13 and 2.14. The results calculated by OPA software show that the designed transport line can well handle an energy spread of less than 1% using the linear beam optic elements. For an energy band of 693 MeV to 707 MeV, the end parameters satisfy the optical conditions at the center of the TGU. It means that for this 1% energy range, there is nearly a beam waist at the center of the undulator $\alpha_{x,y} \approx 0$ and the β functions remain of the same desired order. Figure 3.6 shows the obtained β functions, along the beam transport line, in both x and y plane. Also doing the Beam tracking for a bunch of particles with 5000 electrons and varying the central energy, the phase-space distribution for different energies have been obtained as shown in Fig. 3.7 it can be seen that for the bunches with lower energies, the bunch diverges while the higher energy bunches show a focusing effect. According to what has been derived by Axel Bernhard et al. [81] for a 100-period transverse gradient undulator, the accepted beam sizes are the ones less than 10^{-4} m. So for the designed doublet transport line, the beamlets with less than 1% energy dispersion can well fit the TGU requirements. These days with upgrading

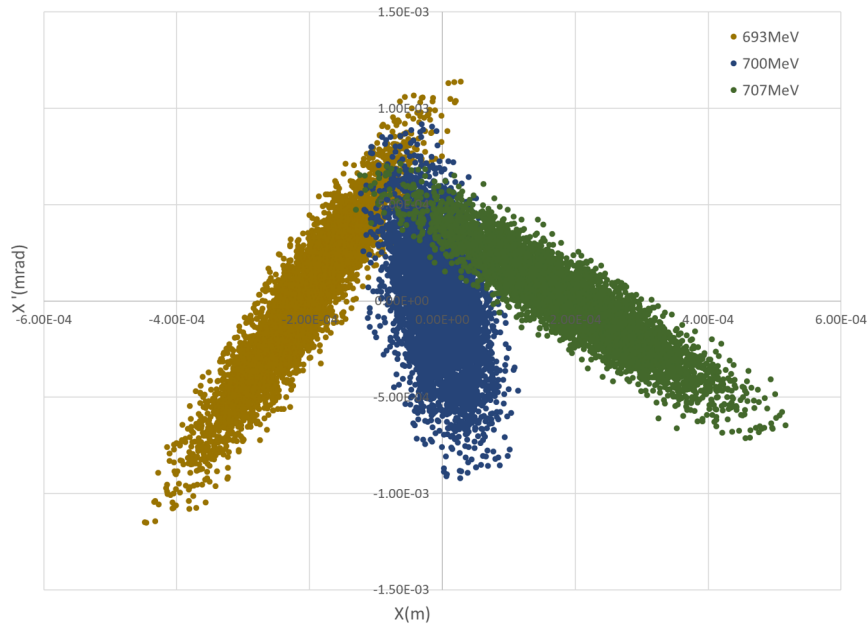


Figure 3.7.: Phase-space distribution for different energies for $\pm 1\%$ energy spread.

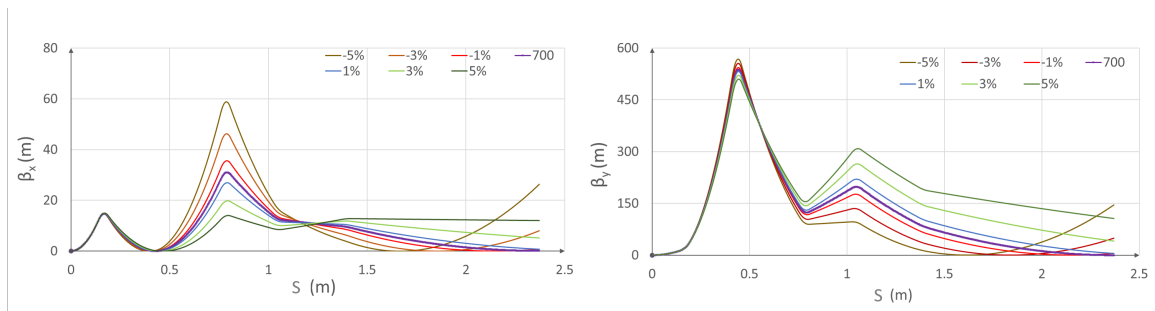


Figure 3.8.: β functions, in x (left) and y (right) planes for different energies up to $\pm 5\%$.

the LPAs an energy dispersion of less than 1% can be easily achieved and such an electron source can well serve this transport line. Investigating the behavior of the optical functions at higher energies, Fig. 3.8, seemed that for energy dispersions higher than 1% and up to $\pm 5\%$, the desired beam dynamics performance can be reached by implying nonlinear elements like sextupoles which can be a future modification of this transport line.

3.2. Magnet design

In this section, the Magnet design for the doublet-based transport line is described. As discussed in Section 3.1.2, for the design of the coils, I

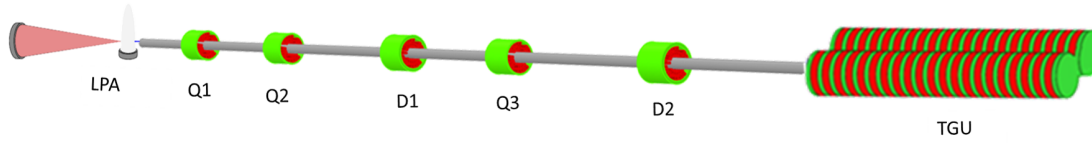


Figure 3.9.: Schematic of the HTS air-core transport line.

chose a 4 mm wide ReBCO tape (SCS4050) from Superpower Inc., this HTS tape has a 50 μm substrate and can easily carry a current density up to the 2000 A mm^{-2} at the magnetic field of 5 T and temperature of 4.2 K. Also in order to achieve high magnetic strengths in this transport line, an air-core geometry for both dipoles and quadrupoles has been considered. In the following sections, the magnet design for the whole transport line (Fig. 3.9) using Opera [21] and CST [82] software is discussed. To start the design process, it was important to determine the gap radius (inner radius of the coils). So considering the experience of winding the cos-theta coil in CEA [57], after discussions with Thibault Lecrevisse from CEA and Anna Kario from Twente university, the lowest bending diameter was found to be 20 mm to limit the risk of coil damage. Although, even at such bending diameters, it is still complicated and challenging to wind the coils [83, 84].

3.2.1. Quadrupole design

Considering magnet specifications in Table 3.3 and using Eq. 2.13, the main parameters for the doublet quadrupoles Q_1 and Q_2 and the quadrupole Q_3 in the dispersive section are specified in Table 3.4. Also as discussed in Section 2.2.7.2, magnet design should be accurate enough such that the particle beam meets a good field quality in the good field region (GFR). GFR is usually determined by the beam size, *i.e.* approximately 2-3 times bigger than the maximum beam size [85]. Referring to Fig. 3.4, β_x is very small along the transport line but the Beta function in the vertical plane, β_y , gets large at the position of the second quadrupole Q_2 , $\beta_y = 530$ m. So, the largest beam size occurs in the vertical direction and is $\sigma_y \approx 2.3$ mm.

To design the magnets I considered ± 5 mm good field region in which the magnet design carried out a field quality of $\Delta g/g_0 \leq 0.1\%$. In transport lines usually, a field quality of 1% is assumed to be enough but due to the

Table 3.4.: Quadrupole magnets specification at 700 MeV.

Magnet	Length(m)	field gradient($T\ m^{-1}$)
Q_1	0.050	504.53
Q_2	0.050	-224.47
Q_3	0.050	-91.57

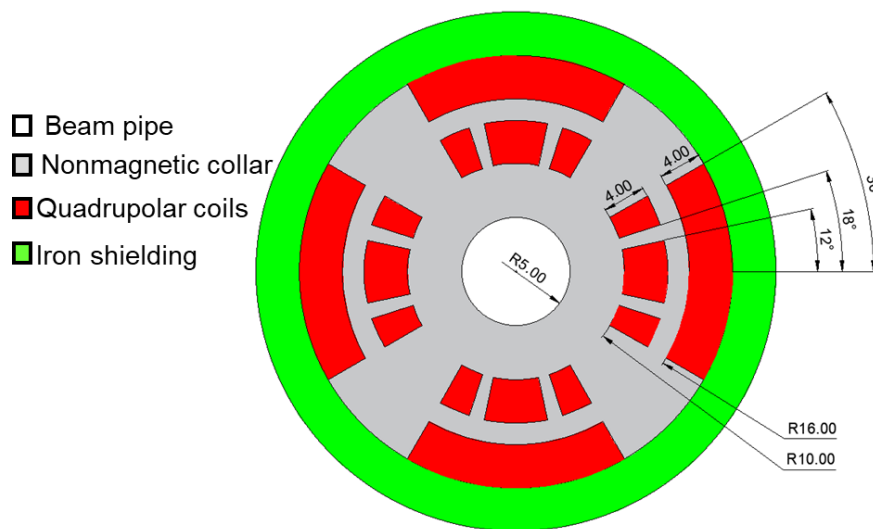


Figure 3.10.: Geometry layout and coil configuration of the quadrupole magnets.

complications in the fabrication of cos-theta magnets, fabrication errors will also be added which decreases the magnet efficiency. So, I made an attempt for smaller field qualities to keep the designs on the safe side. Although the required field quality can be more precisely obtained with the beam dynamics simulations and this can be a future task.

3.2.1.1. Geometry

Using the three-dimensional Opera Software[21], a coil configuration of sectors and wedges of 12° – 18° – 30° was developed for pure quadrupole magnets, Fig. 3.10. The four superconducting coils forming the quadrupole winding are held together by means of non-magnetic collars which are surrounded by iron yokes. The inner radius of the coils and the coil width are considered to be 10 mm and 4 mm, respectively. Coil properties are given in Table 3.5. Since using the HTS wires may come with insulation

Table 3.5.: Quadrupole Coil properties for the air-core transport line.

Parameter	unit	Value
Conductor type	-	ReBCO tape(SCS4050-AP) SuperPower Inc.
Width	mm	4
Substrate thickness	μm	50
Current density	A mm^{-2}	1460
Configuration	-	(12-18-30) / (0-30)
R_{in}	mm	10
$B_{on-coil}$	T	4.6

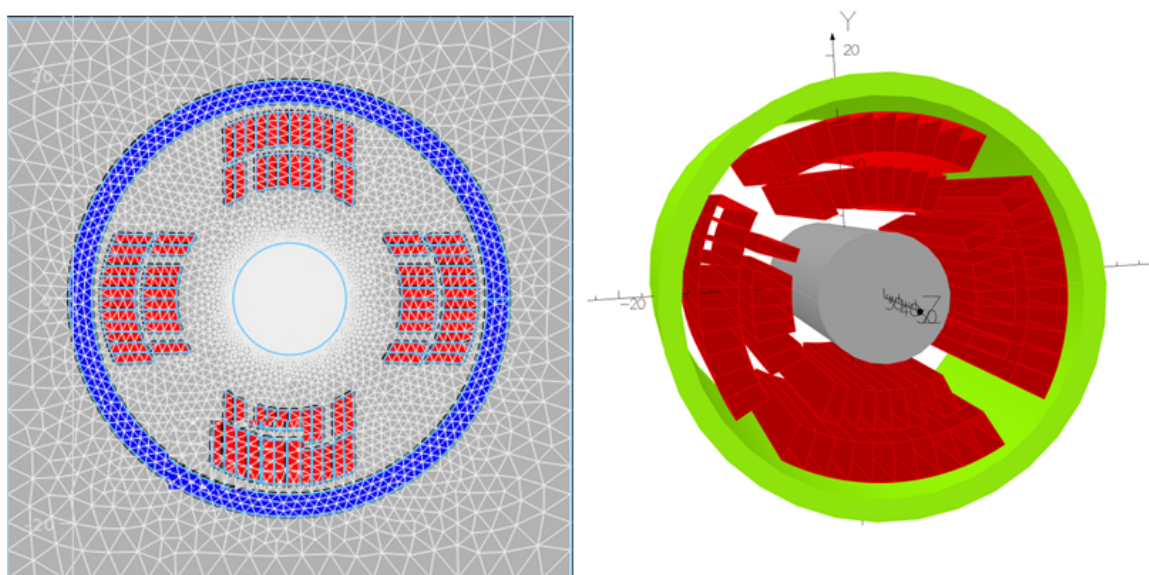


Figure 3.11.: 2D (left) and 3D (right) models of the quadrupole magnet including the beam tube with $r = 5$ mm.

issues, I come to the decision that winding with tapes looks easier to start a demonstrator. So, for winding the coils ReBCO tape (SCS4050-AP) from SuperPower Inc. is chosen.

Simulations are done for a field gradient of 504 T m^{-1} and magnetic length of 50 mm. The current density to achieve the desired field strength is taken to be 1460 A mm^{-2} which is well below the limitations of the SCS4050-AP for the applied magnetic field at 4.2 K. A 2D and 3D model of the simulated magnet including a beam tube with 5 mm radius, is illustrated in Fig. 3.11

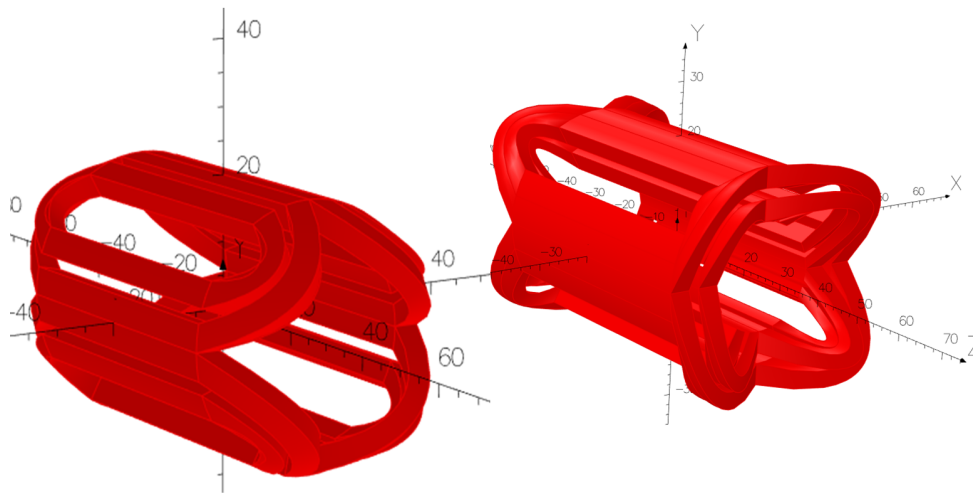


Figure 3.12.: Air-core HTS quadrupoles with (right) and without (left) coil-end design.

3.2.1.2. Coil ends

In order to come to more precise solutions and consider the end effect of the coils, the coils are closed using two other 20-nod bricks at the two ends. After closing the coils and doing the simulations, it was seen that there are unwanted end fields at the two ends of the magnets. To omit these end fields, the coil ends should be designed in a saddle shape which means giving an upward slope to the coil ends. In Fig. 3.12 and Fig. 3.13, these two designs and their related magnetic field in the longitudinal direction (beam direction) are shown and compared. So the final designed model for the magnetic simulations is depicted in Fig. 3.14.

Moreover, it is important to note that the field distribution at the coil ends is complicated and the highest field in the coil is at the return point which can be up to 10% of the central field. Therefore if the coil ends do not clamp well, there would be a Lorentz-force-induced motion which can lead to quenching. So, the windings in the coil head should be spread out using spacers like epoxy fiberglass [35].

3.2.1.3. Field calculations

The obtained field and field gradient with respect to the horizontal and longitudinal axis are shown in Fig. 3.15 and Fig. 3.16, respectively.

For calculating the field gradient at $x = 5 \text{ mm}$ versus the longitudinal direction in Opera software, the field is calculated on the circles of radius

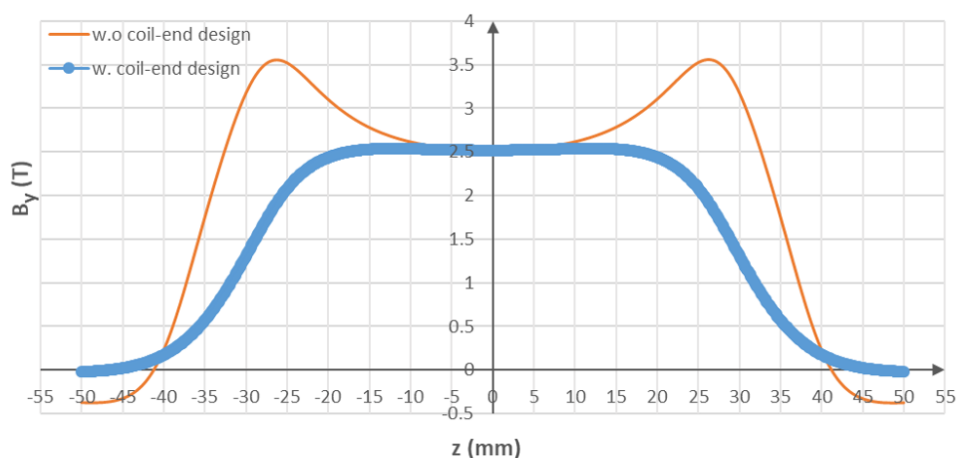


Figure 3.13.: Magnetic field versus longitudinal direction for the coils; with (blue) and without (orange) saddle coil end design.

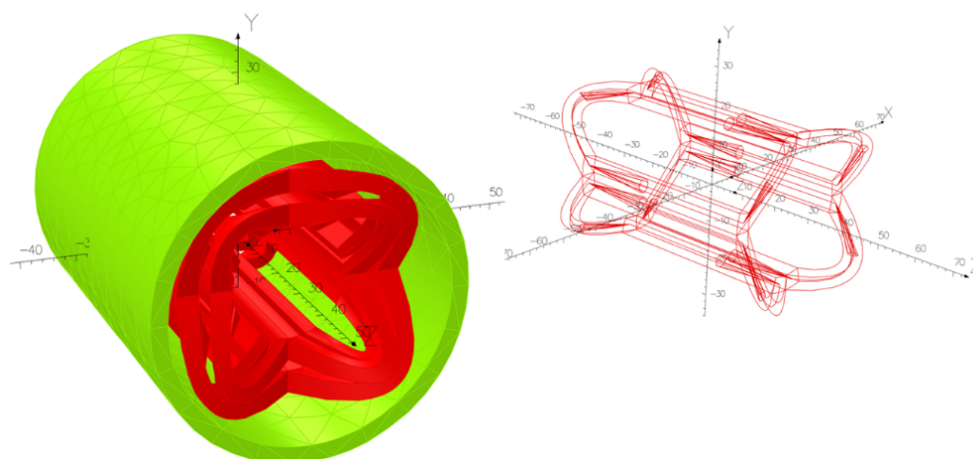


Figure 3.14.: Quadrupole magnet modeled in Opera software.

5 mm which are moved in the beam direction with steps of 2 mm. Using the Fast Fourier Transform, magnetic field, field gradient, and higher order harmonics are obtained in each location. Also, having the field gradient at different longitudinal locations, one can calculate the integrated field gradient at $x = 5$ mm.

3.2.1.4. Field quality

For field uniformity in the central plane $z = 0$, using Eq. 2.44 field gradient tolerances can be obtained as shown in Fig. 3.17: As can be seen above, field tolerance is in order of 10^{-4} in the good field region up to 5 mm.

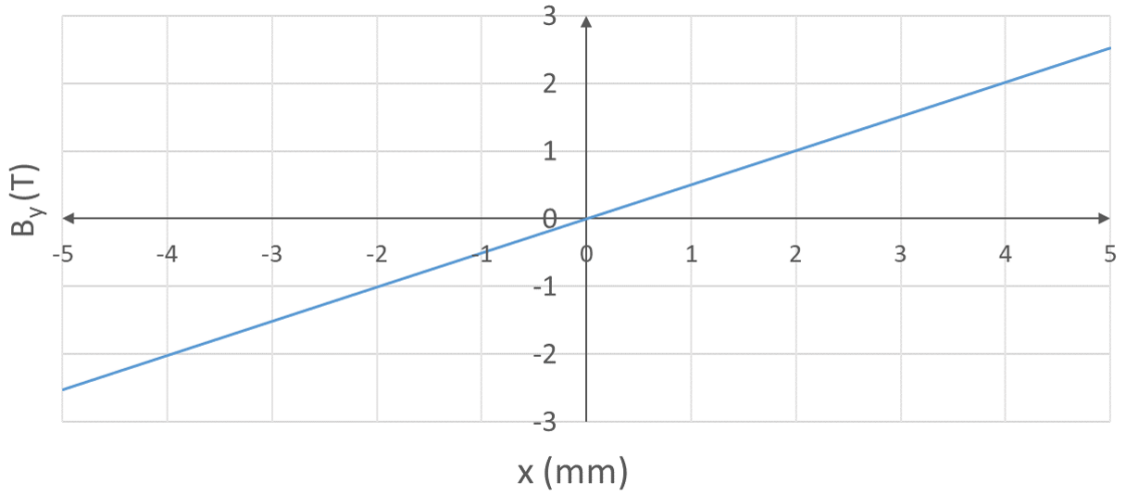


Figure 3.15.: Vertical magnetic field B_y versus horizontal direction at $y, z = 0$.

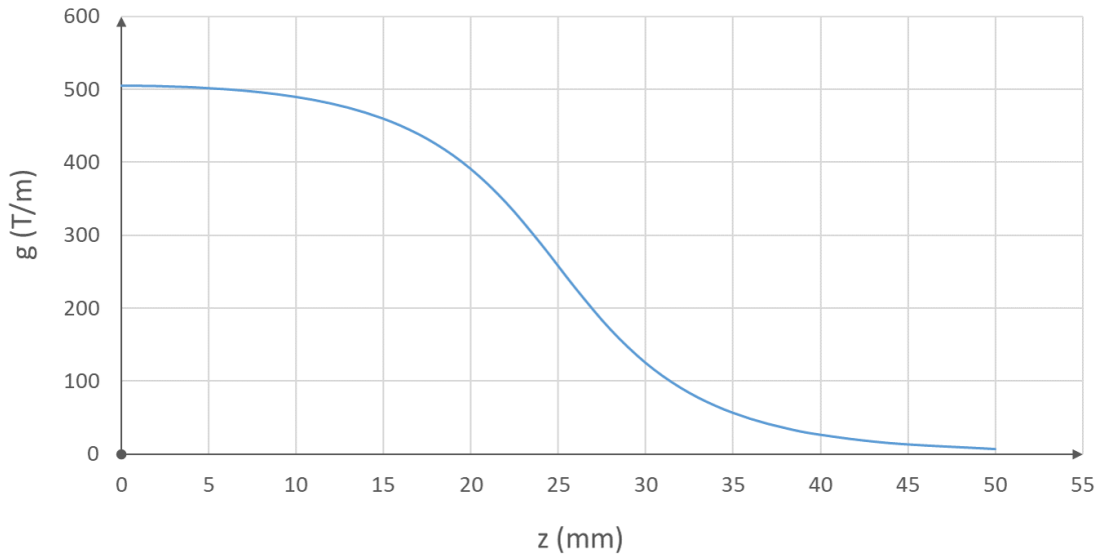


Figure 3.16.: Field gradient versus longitudinal direction on the beam path i.e. $x, y = 0$.

3.2.1.5. Integrated field quality and effective length

Integrated field quality can be obtained using the following equation

$$\frac{\Delta \int g dz}{\int g_0 dz} = \frac{\int g dz - \int g_0 dz}{\int g_0 dz} \quad (3.2)$$

In this relation, the integrals of g and g_0 are the integral of the field gradient in any desired radius and the integral of the field gradient at the center of the magnet *i.e.* the main path of the beam, respectively. To calculate the

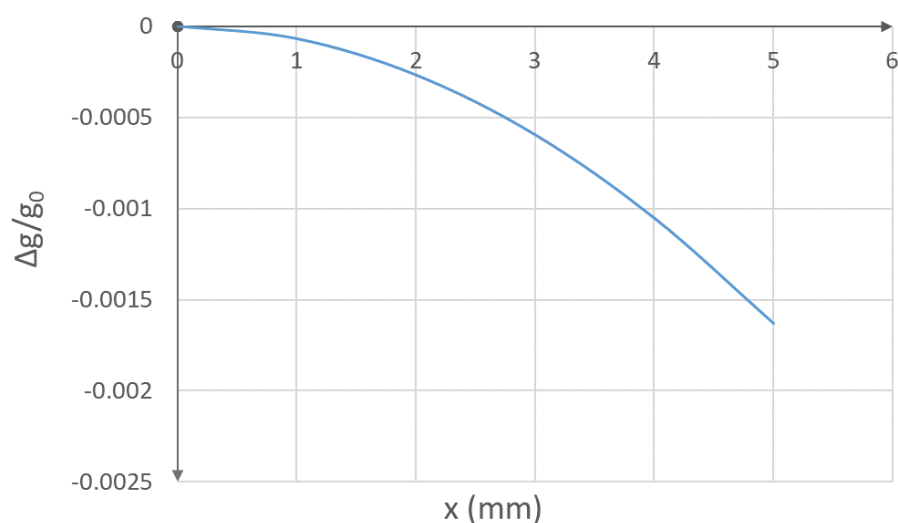


Figure 3.17.: Field gradient quality versus horizontal direction for $y, z = 0$.

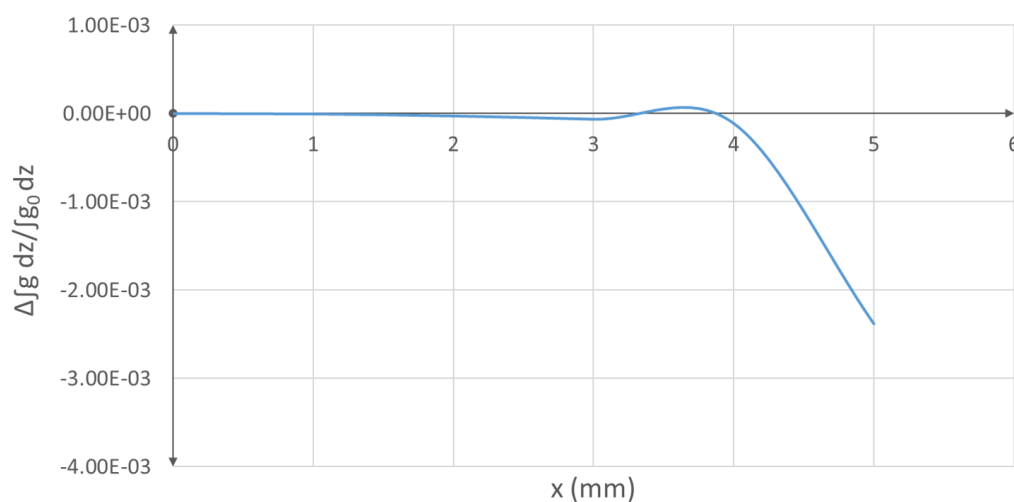


Figure 3.18.: Integrated field gradient quality versus horizontal direction for $y = 0$.

integrated field gradient quality in the good field region, six circles with radii of 0.001, 1, 2, 3, 4, and 5 were considered. These circles were moved along the path of the beam, and each time by using of Fourier transform for each circle, field components were obtained and integral of each of the field components in different radii was calculated. Therefore, the changes of the integrated field gradient in the horizontal direction are derived and shown in Fig. 3.18. As it can be seen in Fig3.18, variation of the integrated field quality within the good field region stays below 2×10^{-3} which is within the acceptable limits.

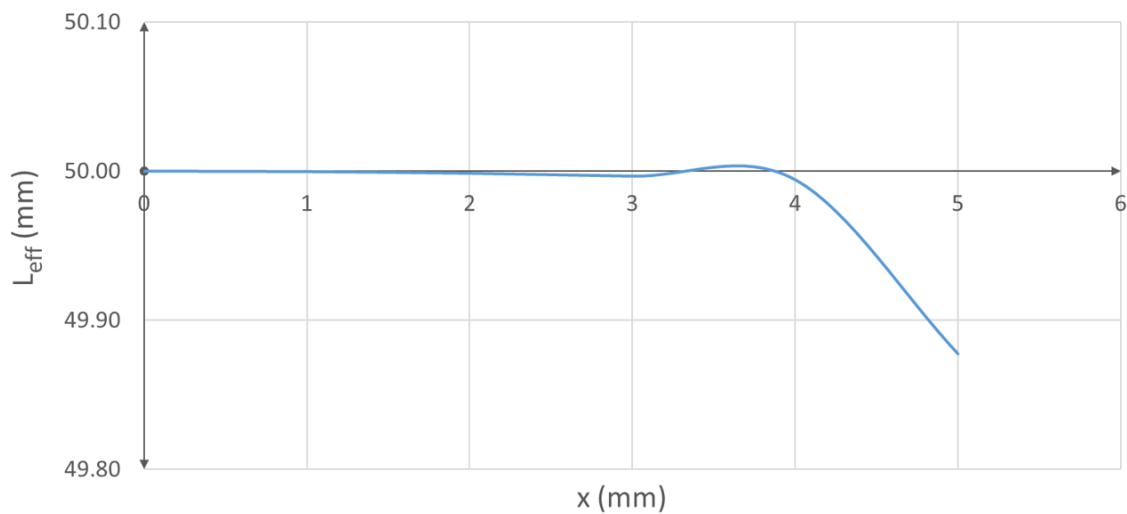


Figure 3.19.: Effective length variation in the horizontal good field region.

According to the beam dynamics calculations, quadrupole magnets should have a 50 mm magnetic length, Table 3.4. To achieve the exact value of the required magnetic length on the beam path, one should modify the length of the coils in several iterations. By applying Eq. 2.42 for the quadrupole magnets, effective length in the horizontal direction up to the limit of the good field region is calculated and the result is indicated in Fig. 3.19. Moreover, considering the experimental facts, the variation of the effective length should not get larger than 5 mm in the good field region so that the particle beam encounters quite equal to the magnetic field while passing through the magnet. The depicted results in Fig. 3.19 show that the effective length has a maximum change of 0.12 mm at the good field region of $x = 5$ mm which is also well within the applicable range.

3.2.1.6. Harmonic analysis

As was discussed in Section 2.2.1, calculating the field harmonics is one of the main steps in magnet design. So, due to the Eq. 2.35, the main field coefficients for the quadrupole magnet at the normalization radius of 5 mm are calculated and summarized in Table 3.6.

It can be seen that the two main higher-order multipoles of the quadrupole magnet field *i.e.* twelfth and twentieth fields, B_6 and B_{10} , are both of the order of 10^{-5} at the GFR radius, which is too small to affect the electron beams and from these results, one may deduce that this magnet design,

Table 3.6.: Quadrupole field coefficients in central plane at $x = 5$ mm.

n	type	B_n (T)	B_n / B_2
2	Q	2.52	1
6	Q	-1.72×10^{-5}	-7×10^{-6}
10	Q	-1.06×10^{-5}	-4×10^{-6}

including the angular configuration of the sector coils and end-coil design, can also well control the higher-order harmonics.

3.2.2. Combined dipole design

In order to have a compact transport line two combined function dipoles, with the same field strength, different signs, and same length, in the dispersive section are considered. These dipoles guide the electron beam, create the required dispersion of 20 mm, and also have a focusing effect due to the additional quadrupole coils which are added to the main coils. Dipole magnet specifications are given in Table 3.7.

3.2.2.1. Geometry

Using the three-dimensional Opera software, a coil configuration of sectors and wedges, 48° - 60° - 72° to create a dipolar field and 12° - 18° - 30° in four-fold symmetry to impose quadrupole field has been developed, Fig. 3.20. All the coils have a width of 4 mm and the smallest inner radius is considered to be 10 mm to ease the winding process. The advantage of the design in Fig. 3.20 is that the dipolar and quadrupolar components are independent of each other and changing the current in each set of sector coils can change the relevant field strength. In air-core dipole magnets like quadrupole magnets,

Table 3.7.: Dipole magnets specification at 700 MeV.

Magnet	Length(m)	Field (T)	Field gradient($T m^{-1}$)
D_1	0.050	1.22	205.48
D_2	0.050	-1.22	28.95

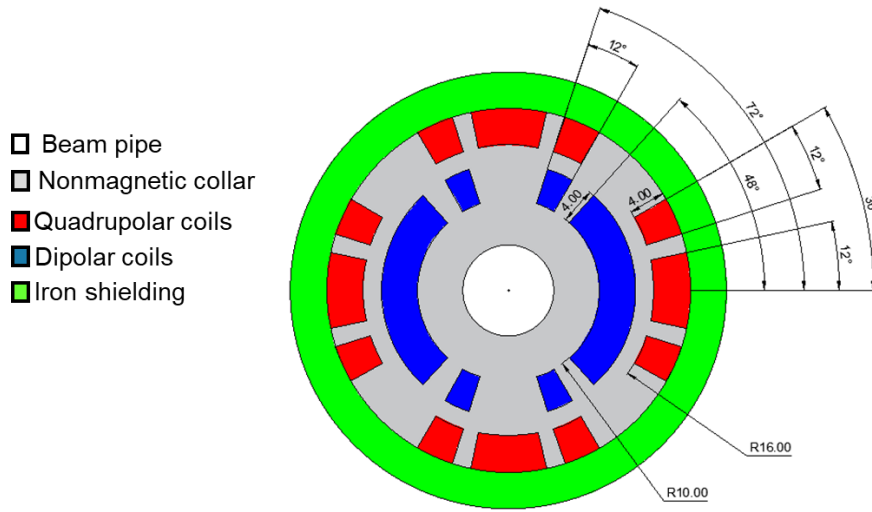


Figure 3.20.: Coil configuration of the combined function dipole magnets, blue coils indicates the dipolar coils red coils create the quadrupole field.

Table 3.8.: Combined dipoles coil parameters.

Magnet	D1	D2
Dipole coils current density ($A\text{ mm}^{-2}$)	500	500
Quadrupole coils current density ($A\text{ mm}^{-2}$)	1341	200
$R_{indipolar}$ (mm)	10	10
$R_{inquadrupolar}$ (mm)	16	16

non-magnetic collars help the winding to stay fixed and not move because of electromagnetic forces. Also, a hollow cylindrical iron yoke is mounted around the coil to shield the outer side of the magnet against possible ring fields. Additionally, an iron yoke can reduce the stored energy which assists in case of error and quench. Simulations are done for both D1 and D2 with a field of 1.22 T and field gradient of 205.5 T m^{-1} and 29 T m^{-1} . The current densities to achieve these desired field strengths are brought in Table 3.8 and the coils are designed to be wound with ReBCO tape (SCS4050-AP), as mentioned before. Also, the coil ends were designed for both dipoles and quadrupoles, The finite element simulation results for the combined dipole D1 are given in the following sections. The required field parameters for D2 can be easily obtained by inversion of the current direction in dipole

19/Mar/2022 15:16:11

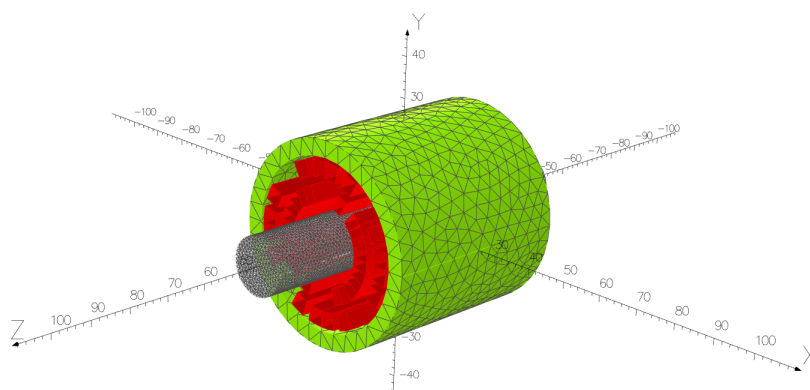


Figure 3.21.: 3D models of the combined dipole magnet including the beam tube with $r = 7$ mm.

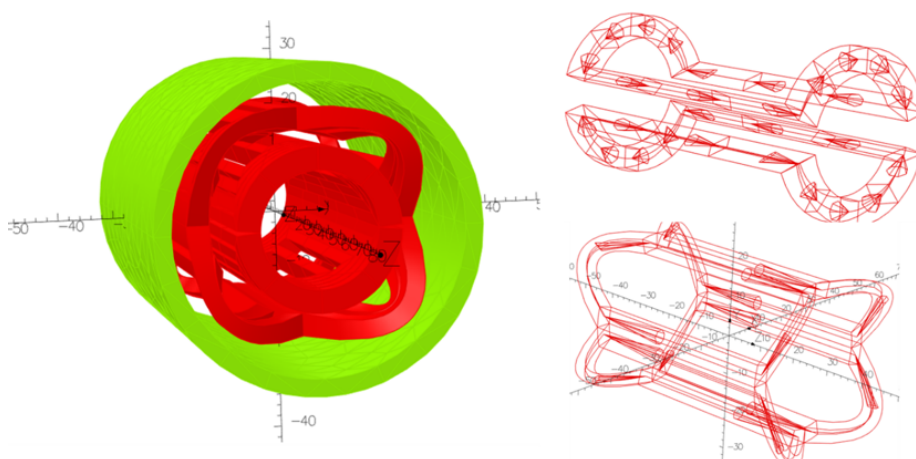


Figure 3.22.: Combined dipole magnet with end coil design, dipole coils (right-top), and quadrupole coils (right-bottom).

coils and decreasing the current of the quadrupole coils to reach the $g = 29 \text{ T m}^{-1}$.

3.2.2.2. Field calculations

The obtained field and field gradient with respect to the horizontal and longitudinal axis are shown in Fig. 3.23 and Fig. 3.24, respectively.

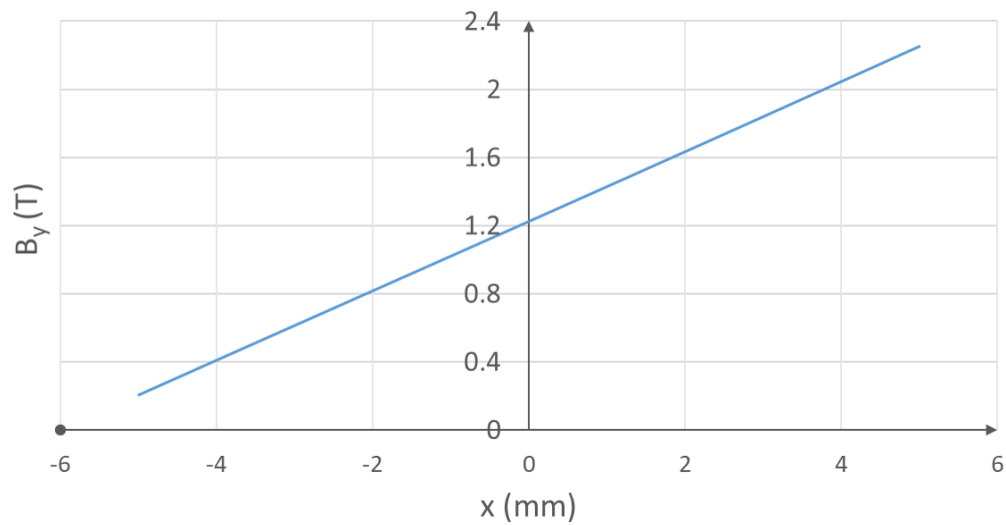


Figure 3.23.: Vertical magnetic field B_y versus horizontal direction at $y, z = 0$.

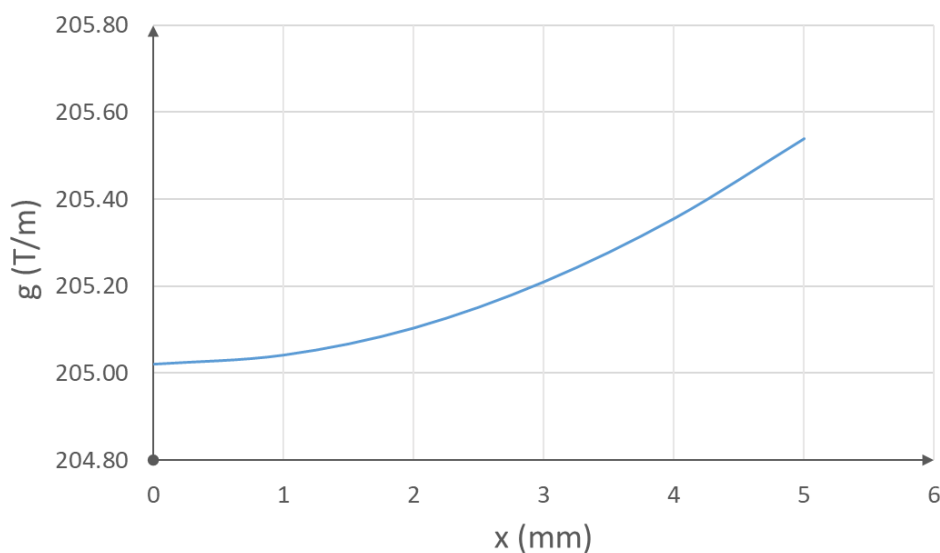


Figure 3.24.: Field gradient versus horizontal direction at $y, z = 0$.

3.2.2.3. Field quality

For field uniformity in the central plane $z = 0$, the following formula was used:

$$\frac{\Delta B}{B_0} = \frac{B - B_0 - g_0 x}{B_0 + g_0 x} \quad (3.3)$$

Therefore field and field gradient tolerances can be obtained as shown in Fig. 3.25 and Fig. 3.26. As can be seen, the obtained tolerances are of the

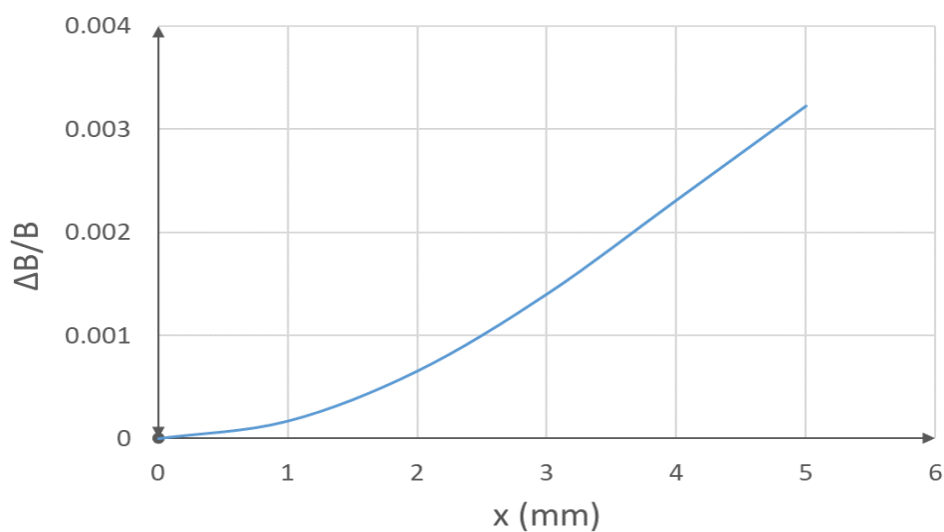


Figure 3.25.: Field quality versus horizontal direction at $y, z = 0$.

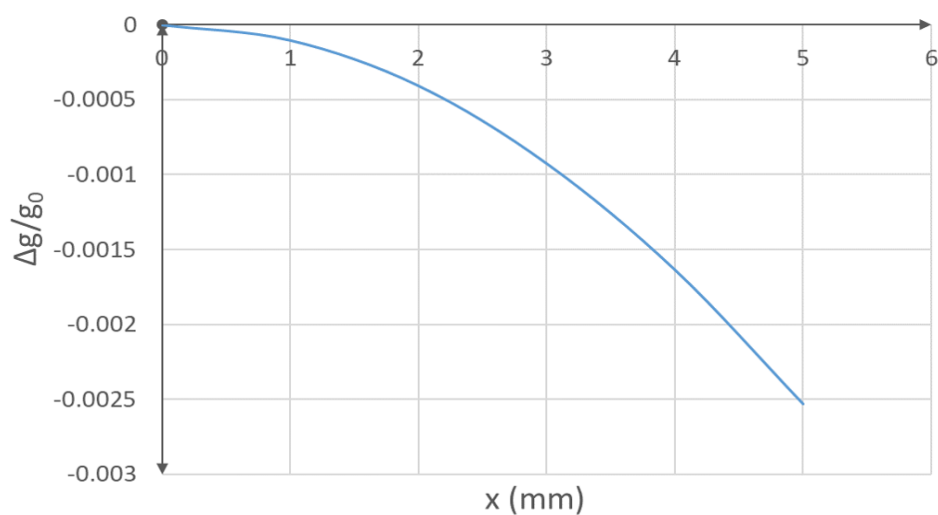


Figure 3.26.: Field gradient quality versus horizontal direction at $y, z = 0$.

order of 10^{-3} in the good field region up to 5 mm.

3.2.2.4. Integrated field quality and effective length

Integrated field quality can be obtained using the following equation

$$\frac{\Delta \int B dz}{\int B_0 dz} = \frac{\int B dz - \int (B_0 + g_0 x) dz}{\int (B_0 + g_0 x) dz} \quad (3.4)$$

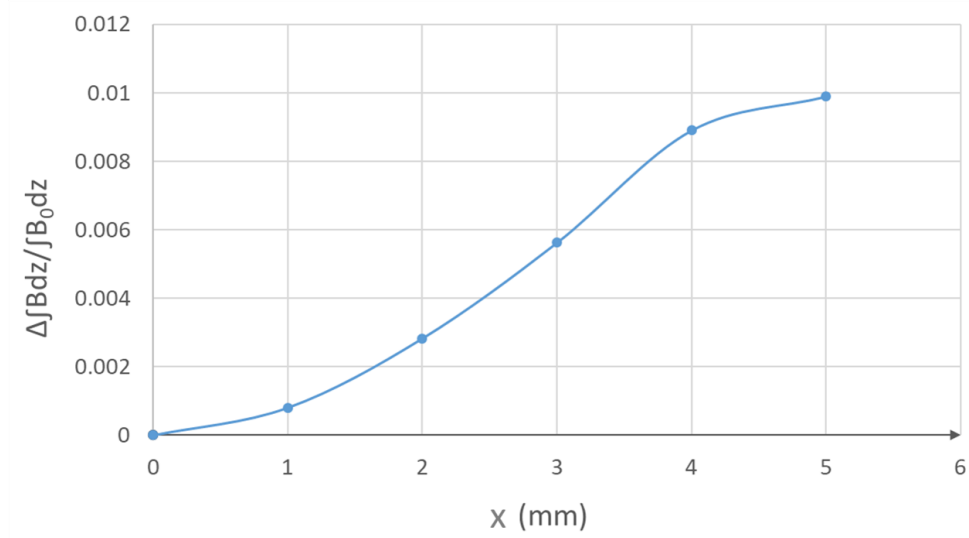


Figure 3.27.: Integrated field gradient quality versus horizontal direction at $y = 0$.

In this relation, the integrals of B , B_0 , and g_0 are the integral of the field in an arbitrary radius, the integral of the field at the center of the magnet, and the integral of the field gradient at the center of the magnet, respectively. To calculate the integrated field quality in the good field region, the same method as in the previous section is applied. Therefore, the changes of the integrated field in the horizontal direction are calculated and shown in Fig. 3.27.

3.2.2.5. Harmonic analysis

According to the discussions in Section 2.2.1, due to the finite transverse length of the magnets, higher-order multipoles always exist in the field distribution of each magnet. Calculating the field harmonics is one of the main steps to validate the magnet design. So, due to the Eq. 2.35, the main field coefficients for the combined dipole magnet at the normalization radius of 5 mm are calculated and summarized in Table 3.9. As was given in the above table, allowed field multipoles for the combined dipole are the ones for dipole and quadrupole *i.e.* 6-pole, 10-pole, 14-pole, and 18-pole together with 12-pole and 20-pole components. The most important field multipole in dipole-quadrupole combined magnets are the sextupole (6-pole) and twentieth-pole (20-pole) fields which in this magnet design turned out to be of the order of 10^{-3} and 10^{-5} , respectively. For the combined function

Table 3.9.: Combined dipole D1 field coefficients in the central plane at 5 mm.

n	type	B_n (T)	B_n / B_2
1	D	1.22	-
2	Q	1.02	-
3	D	-2.77×10^{-3}	-1.24×10^{-3}
5	D	-8.45×10^{-5}	-3.77×10^{-5}
6	Q	-6.64×10^{-5}	-2.96×10^{-5}
7	D	-8.93×10^{-4}	-3.99×10^{-4}
9	D	1.20×10^{-7}	5.36×10^{-8}
10	Q	5.77×10^{-8}	2.58×10^{-8}

dipoles these values are well-acceptable, especially in the case of a transport line in which the electrons are passing through the magnets once. Although to investigate the effect of the multipoles on the beam dynamics one can insert these values as an error to the beam dynamics simulations that can be a future step to this project.

3.3. Force calculation

As discussed in Section 2.5.2, high-temperature superconductors are ceramic-like, brittle structures often in form of the tapes. So during the winding process, especially for the complicated coil geometries, these tapes may endure stress and strains which could affect the superconducting properties and lead to high degradation. Also powering the coils to high currents can exert big electromagnetic forces on the coils. To deal with these forces and reduce the stress on the tapes a good support structure around the coils can be used to fix the coils on the place. In other words, as it was mentioned in Section 3.2.1.2, the coils should be designed such that the stress and strains on the tapes stay within an allowed limit. This limit is different for different tapes at different working conditions. In an investigation by Barth et al. [77], the strain and stress dependence of the current carrying capabilities as well as the stress and strain correlation are investigated for some commercial coated conductors including the ReBCO tape (SCS4050-AP) from

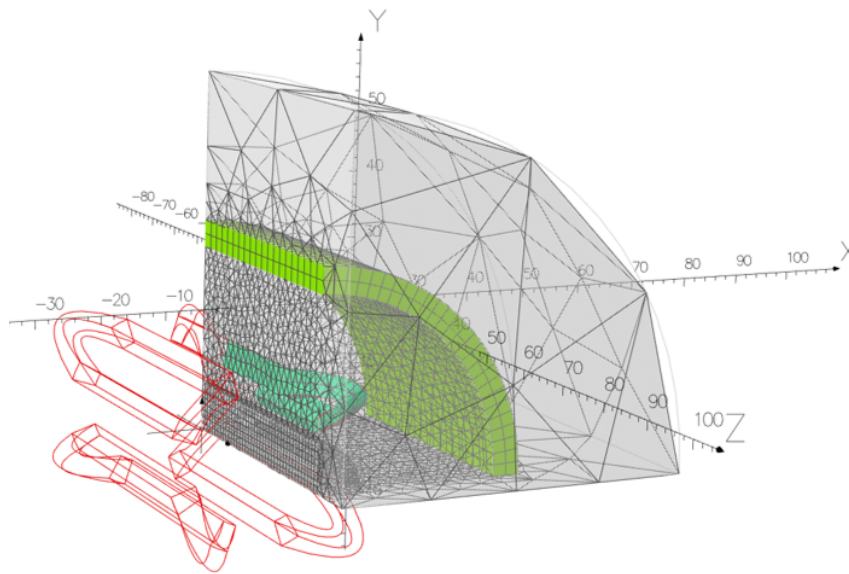


Figure 3.28.: One-fourth of the simulated quadrupole coils with mesh lines.

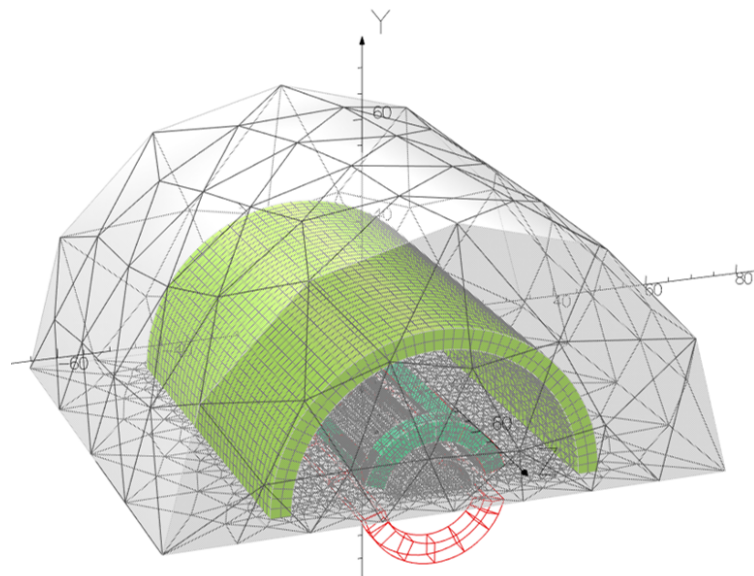


Figure 3.29.: One-half of the simulated dipole coils with mesh lines.

Superpower that is used for designing the air-core magnets.

So having the electro-mechanical properties of the ReBCO tape (SCS4050-AP) at 4.2 K, Von Mises stress for the quadrupole coils as well as the dipole coils are calculated. The simulation is done in magneto-static and static-stress modules, using Opera software [21]. For the static stress, the coils are defined as a body with a specific mesh size while the electro-mechanical

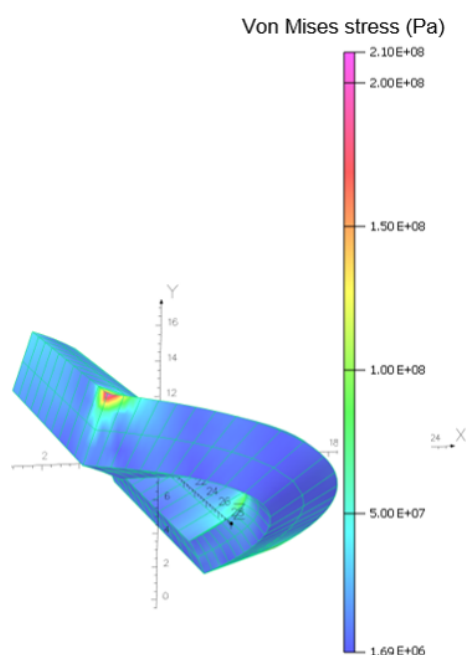


Figure 3.30.: Von Mises stress on one-fourth of the quadrupole HTS coil at 4.2 K.

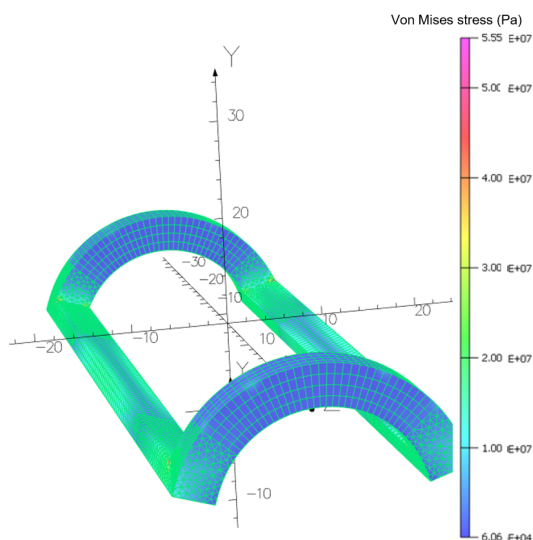


Figure 3.31.: Von Mises stress on one-half of the dipole HTS coil at 4.2 K.

properties of the ReBCO tape and the mechanical boundary conditions are also specified. As can be seen in figures 3.30 and 3.31, Von Mises stress in both coils is mainly of the order of 10^7 Pa while in the sharp turning corners it is increased to 5×10^7 and 2×10^8 Pa. According to the report by Barth et al. [77], ReBCO tape (SCS4050-AP) can tolerate stresses to the limit of 800 MPa at 4.2 K. So the stress obtained for both dipole and quadrupole

coils is well below this limit although more modifications on the coil ends can be done as a future step of this project.

4. HTS iron-core transport line

As it was discussed in the previous chapter, cos-theta air-core magnets can generate higher magnetic fields and therefore can guide and control the particle beam at higher energies. But the main disadvantage of these magnets is the complicated coil geometry which makes the coil winding difficult, especially in the case of miniature HTS-coated conductor coils. To ease this difficulty, designing iron-core magnets with simple shape HTS coils was investigated. The idea was to use simple pancake coils for which two designs were considered. Shell coil and periodic quadrupole geometries, as shown in Fig. 4.1. For the shell coil geometry, two HTS pancake coils with opposite current directions are placed parallel to the x-y plane at a distinct distance from each other, Fig. 4.2. In this model, there is a quadrupolar field in the transverse plane which can be optimized by shimming and designing the pole profile, see Section 2.2.7.2. There exists also a solenoidal field component, B_z , along the longitudinal direction, z , but the integrated solenoidal field is fully eliminated due to the opposite current directions in the two coils, Fig. 4.3. The main disadvantage of the shell coil geometry is that the field gradient raises not more than $g = 50 \text{ T m}^{-1}$, but for the low

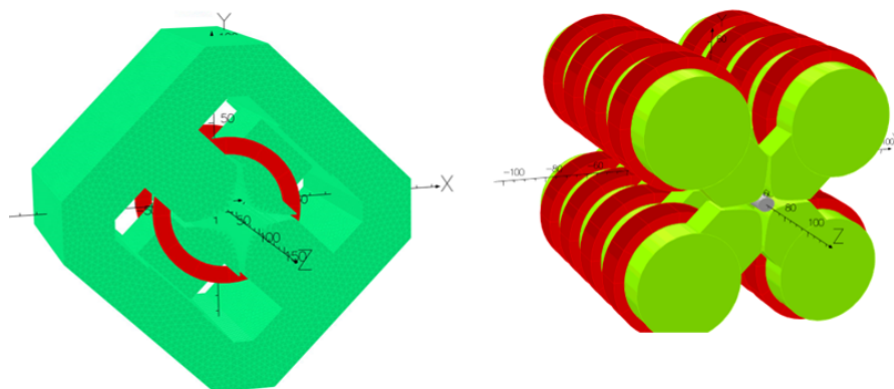


Figure 4.1.: Iron-core quadrupole designs: shell coil geometry (left) and periodic geometry (right).

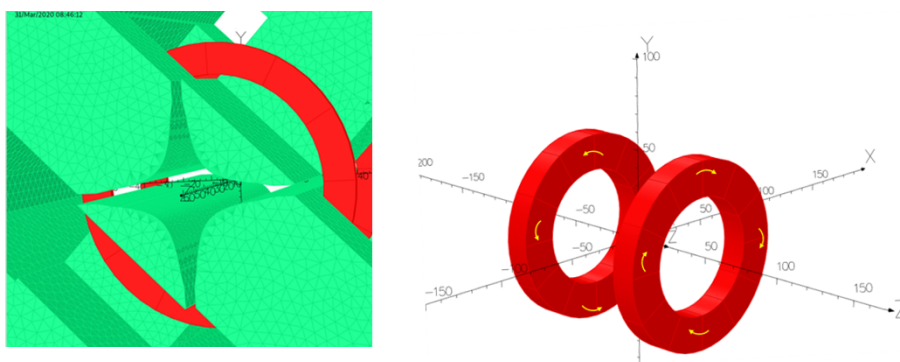


Figure 4.2.: Shell coil geometry yoke design (left) and coils with current direction (right).

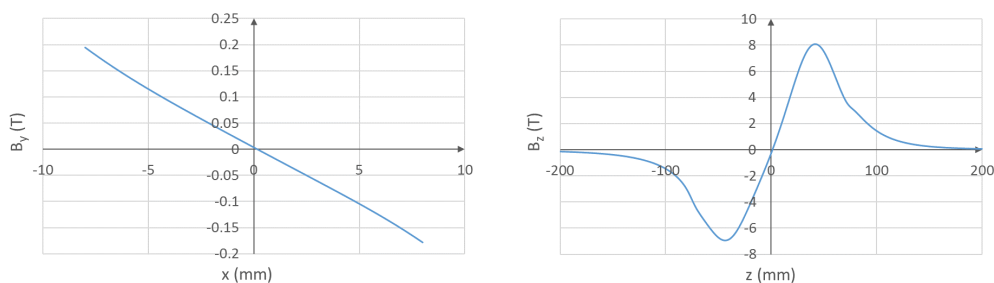


Figure 4.3.: Vertical magnetic field B_y versus horizontal direction at $y, z = 0$ (left) and longitudinal magnetic field B_z versus longitudinal direction at $x, y = 0$ (right).

field gradients and low current densities applications, this design could be a good choice as it does not have complicated coil windings [86].

The second designed model, the periodic quadrupole, is a novel magnet design (that to my knowledge is not reported before) and consists of several HTS pancake coils in which the neighboring coils have opposite current directions making a periodic structure with periodic length λ . The coils are located on a cylindrical iron yoke and the quadrupolar field shape is created by an optimized hyperbolic iron pole, Fig. 4.4. This magnet geometry gives a high-quality field in both transverse and longitudinal planes, using HTS-coated conductors and by employing current densities as high as 2000 A mm^{-2} field gradients as high as 200 T m^{-1} can be created. Moreover, by changing the periodic length λ , and/or the number of periods the magnetic field distribution in the longitudinal direction can be optimized to efficiently capture and transport the LPA-generated bunches in a compact transport line. More details are described in the following sections.

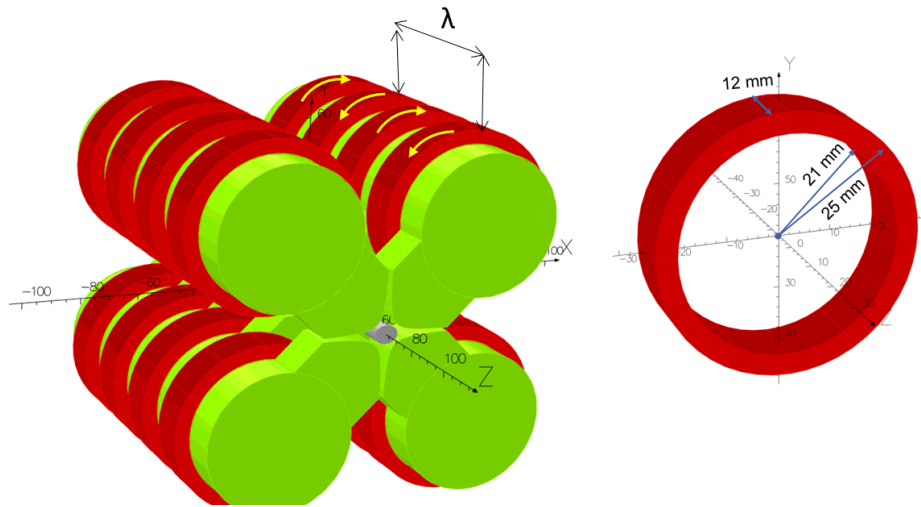


Figure 4.4.: Periodic quadrupole; pancake coil dimensions (right) and whole geometry with periodic length λ (left), green and red represent iron yoke and current carrying coils respectively.

4.1. Periodic quadrupole

4.1.1. Magnet design

Designing the periodic quadrupole magnet was done in two steps, the 2D and the 3D design. The 2D design, *i.e.* designing the hyperbolic pole profile, includes defining the proper pole width and pole shims so that a good magnetic field quality in the good field region of ± 5 mm can be achieved. The 3D design of the magnet mainly determines the number of periods and the periodic length and was done in parallel with the beam dynamics calculation leading to a multiplet quadrupole capable of effectively collimating the electron beam right after the LPA source. The Magnet design was done in 2D with Poisson [22] and in 3D with Opera [21] and CST [82]. In parallel, electron beam dynamics in this periodic magnet structure were explored using ASTRA [70]. In this section, the 2D and 3D design of the periodic quadrupole is discussed in detail.

4.1.1.1. 2D design

- **pole profile design** Using the two-dimensional, finite-element magneto-static code Poisson, a pole geometry was developed for the periodic quadrupole. The pole face had a broad low shim at the pole edge to maintain the field

Table 4.1.: Pole profile coordinates of the periodic quadrupole.

NO.	x (mm)	y (mm)	NO.	x (mm)	y (mm)
1	4.95	4.95	10	13.95	1.76
2	5.95	4.12	11	14.95	1.64
3	6.95	3.53	12	15.95	1.54
4	7.95	3.08	13	16.95	1.45
5	8.95	2.74	14	17.95	1.37
6	9.95	2.46	15	18.95	1.29
7	10.95	2.24	16	19.95	1.23
8	11.95	2.05	17	20.95	1.17
9	12.95	1.89	18	22.20	1.17

homogeneity over the good field region of ± 5 mm. The pole profile points were derived using Eq. 2.38. The shims were added to the pole ends and designed using an iterative process. The shape and coordinates of the optimized pole profile are given in Fig. 4.5 and Table 4.1 respectively.

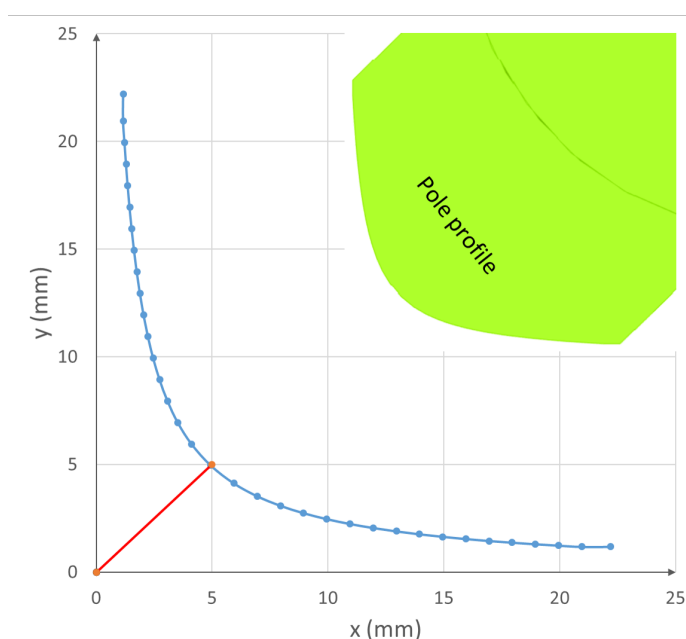


Figure 4.5.: Shape of the designed pole profile for the periodic quadrupole, the green part on the top right shows the pole profile and the pole root of the magnet modeled in Opera.

- **2D Field calculations** Using the material properties of the soft ferromagnetic material XC-06, [12], the magnetic field and field quality in the transverse

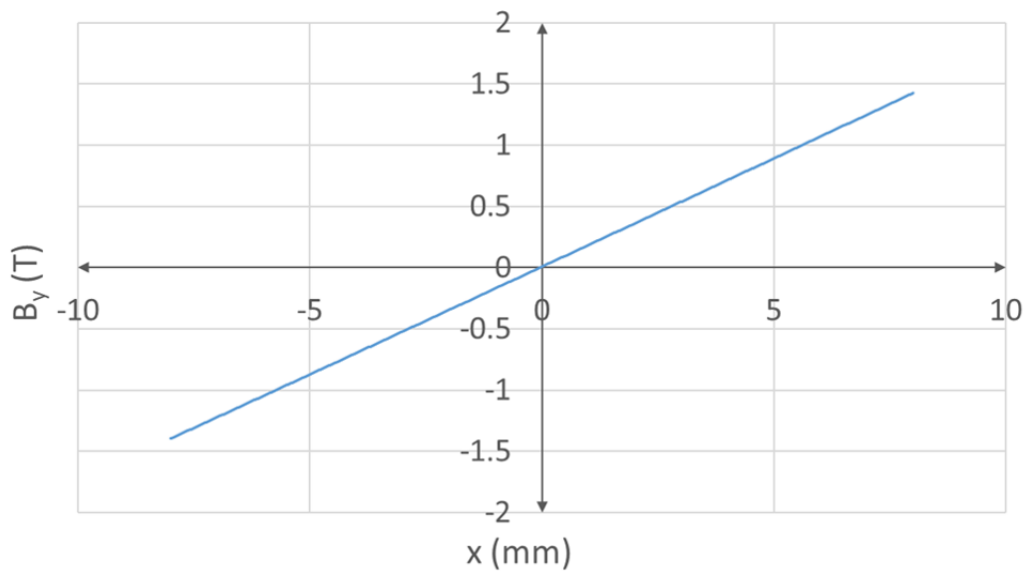


Figure 4.6.: Magnetic field B_y versus horizontal direction x at $y, z = 0$.

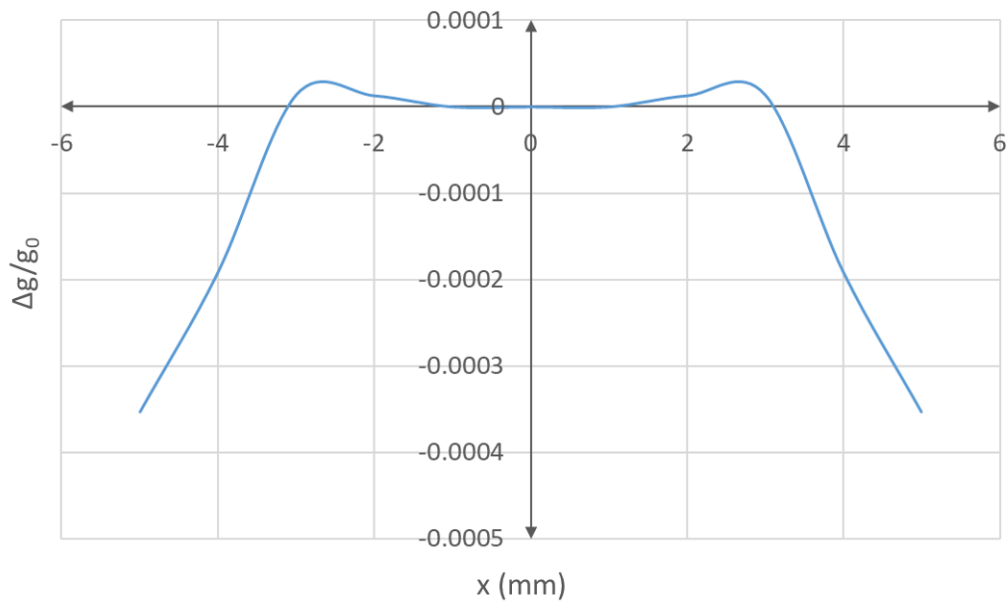


Figure 4.7.: Magnetic field quality versus horizontal direction x at $y, z = 0$.

plane were calculated. The results are shown in Fig. 4.6 and Fig. 4.7, respectively. As can be seen in Fig. 4.6, the magnetic field has a linear behavior in the horizontal direction which leads to a constant field gradient. During the magnet fabrication and assembly process, fabrication errors are always added to the design errors, making the magnetic field quality worse. Therefore I aimed to keep the higher order fields as small as possible in the

design, *i.e.* in the order of 10^{-4} in the good field region of ± 5 mm to ensure a field quality of better than 10^{-2} after fabrication.

4.1.1.2. 3D design

The main idea for designing and developing the periodic quadrupole is to substitute it with the doublet/triplet section in the transport line, see Section 3.1.2.2 and Section 3.1.2.1. Therefore magnet 3D design to determine the number of periods and the periodic length of the magnet was done in parallel to the beam dynamics calculation to ensure an efficient capture and transportation of the LPA-generated bunches. In fact, this task was a loop of magnet design and beam dynamics simulation in several iterations to reach the desired beam focusing in both transverse planes. Using the geometric characteristics of commercially available 12mm-width HTS ReBCO tape and assuming a current density of 2000 A mm^{-2} , I started the 3D design from a primary model shown in Fig. 4.4. This magnet is a 1.5-period structure with 12.6 cm magnet length and 5.9 cm periodic length. The magnetic field gradient along the longitudinal direction z , obtained from the Opera simulations is plotted in Fig. 4.8. Now that the magnetic field is calculated, it is good to see how this field affects the electron beams while passing through the magnet. In ASTRA magnets can be defined in two ways, either by their magnetic field gradient values as a function of

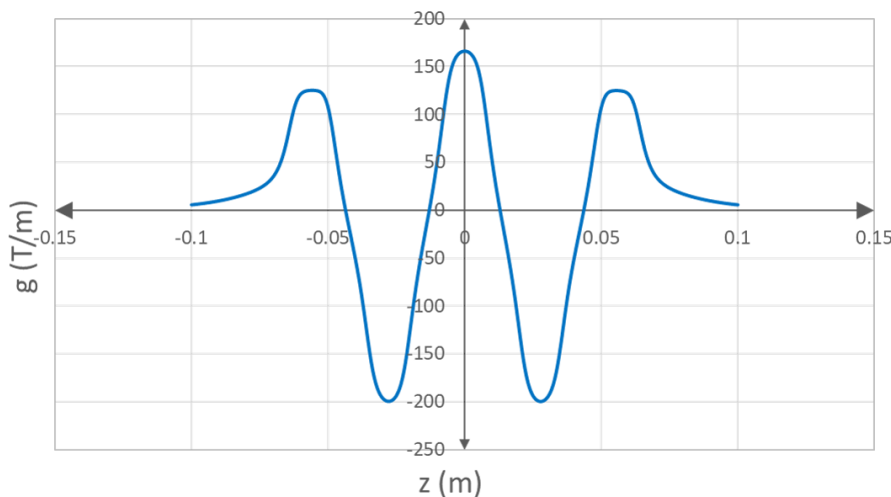


Figure 4.8.: Magnetic field gradient g along the longitudinal direction z for a 1.5-period model at $y = 0$.

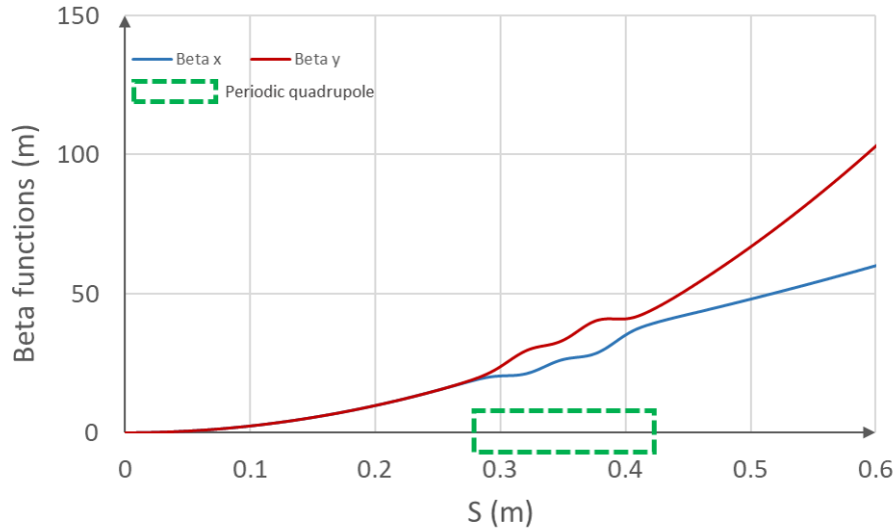


Figure 4.9.: Beta functions β_x and β_y along beam trajectory S , for 1.5-period model with $\lambda = 5.9$ cm at the energy of 260 MeV.

longitudinal position or by a magnetic field map. I extracted the magnetic field gradient from Opera and CST and defined the periodic quadrupole geometry in ASTRA with its center located at 38.4 cm from the LPA source. By inserting the beam optics parameter values of the LPA source, as previously listed in Table 3.1, the resulting beta functions were obtained for an electron energy of 260 MeV. It can be seen in Fig. 4.9 that the beam size is growing rapidly in both, x and y direction which means this periodic structure can not collimate the electron beam. In order to find the proper solution, different magnet geometries with different periodic lengths and different period numbers were investigated using a parametric magneto-static simulation in CST, Fig. 4.10 and Fig. 4.13. In parallel, the effect of such geometries on the electron beams was studied using ASTRA. For these simulations, the magnet center is located at 38.4 cm from the LPA source, electron energy is 260 MeV and coils have an inner radius of 21 mm and an outer radius of 25 mm and are wound with 12 mm width SCS12030-AP ReBCO tape from Superpower Inc. [39]. Each coil has 72 turns and at 4.2 K carries 2000 A mm^{-2} current density. There is 1333 A current per tape, *i.e.* 96 000 A.t per coil. Coils specifications are given in Table 4.2 and further details of the electrical parameters, coil winding, and connection scheme will be discussed later in Section 4.3.

The investigated periodic models shown in Fig. 4.10 have 1.5 periods but

Table 4.2.: Coil specifications for the periodic quadrupole magnet.

Parameter	Unit	Value
Conductor type	-	ReBCO tape (SCS12030-AP)
Tape Width	mm	12
Tape thickness	mm	0.055
Substrate thickness	mm	0.030
R_{in}	mm	21.00
R_{out}	mm	25.00
Radial thickness	mm	4.00
No. turns	-	72.00

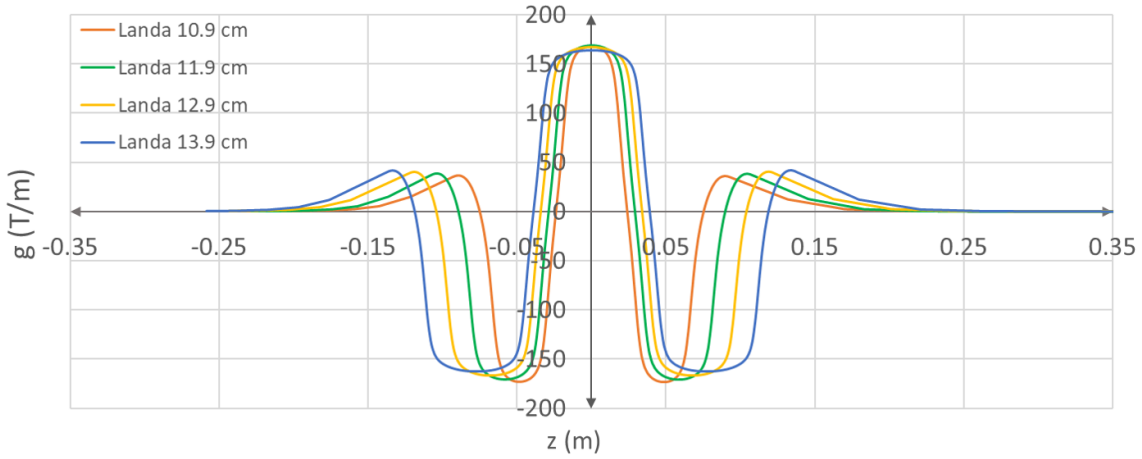


Figure 4.10.: Field gradient g versus longitudinal direction z for 1.5-periods model and different periodic length.

different periodic lengths from $\lambda = 10.9$ to 13.9 cm. It can be seen that by enlarging the periodic length, the field gradient distribution in the longitudinal direction is broadened. Using these field gradient distributions, one can do the beam tracking in ASTRA. The beta functions resulted from passing the electron beam through the 1.5-period model with $\lambda = 11.9$ cm and 13.9 cm and are plotted in Fig. 4.11 and Fig. 4.12, respectively. As can be seen, there is still an increasing trend for $\beta_y(z)$ whereas the β_x value is decreased quite well at the end of the Periodic structure. So keeping the periodic length to $\lambda = 11.9$ cm and $\lambda = 13.9$ cm, in a try to focus the electron beam in both transverse directions, I explored more models with a higher number of periods. Figure 4.13 shows field gradient distribution in the longitudinal direction z for the models with $\lambda = 11.9$ and 13.9 cm and 2

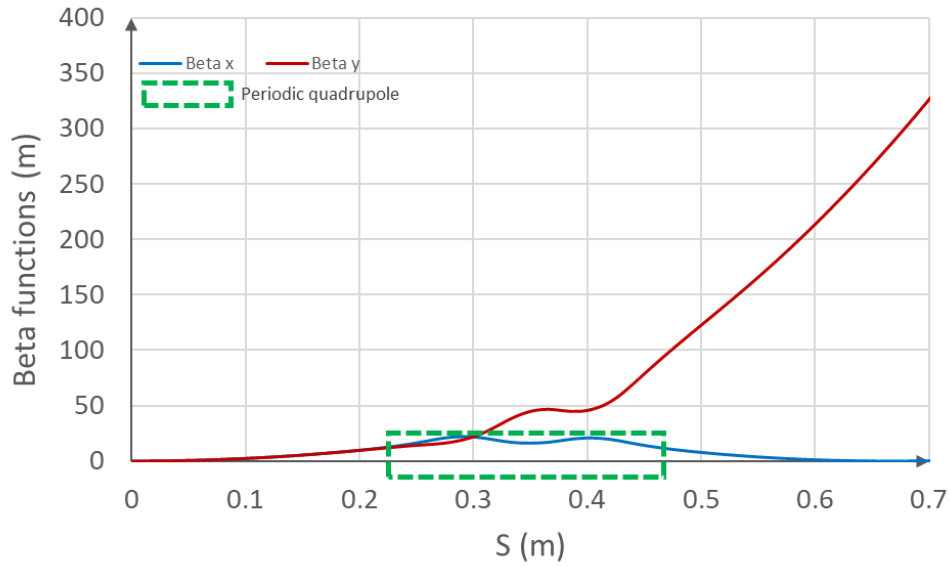


Figure 4.11.: Beta functions β_x and β_y along beam trajectory s , for 1.5-period model with $\lambda = 11.9$ cm at the energy of 260 MeV.

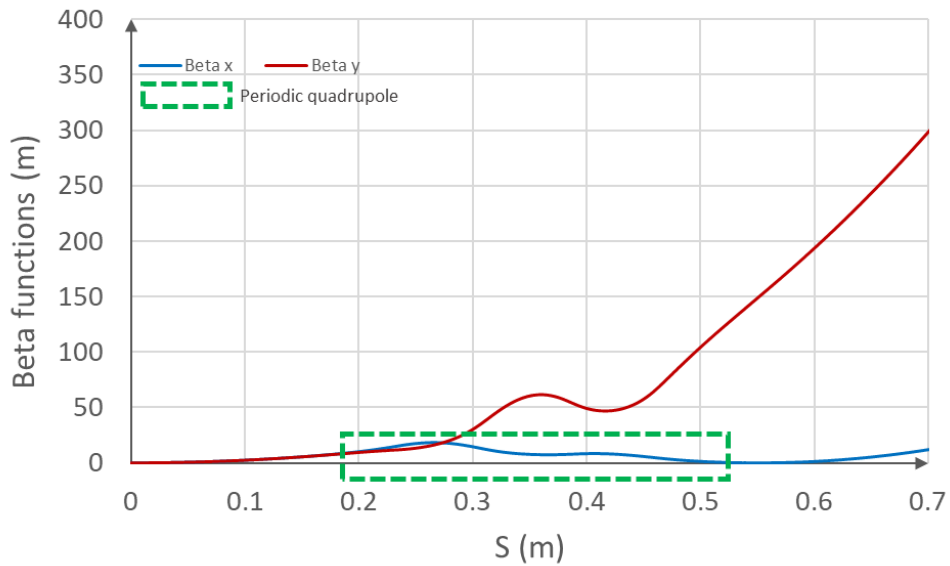


Figure 4.12.: Beta functions β_x and β_y along beam trajectory s , for 1.5-period model with $\lambda = 13.9$ cm at the energy of 260 MeV.

and 3 periods. These results are obtained from magneto-static simulations in CST. Employing these field gradients on the electron beams coming from the Laser Plasma accelerator (LPA), transverse beta functions are derived as in, Fig. 4.14. As it is shown, these 2 and 3-period models can collimate the

4. HTS iron-core transport line

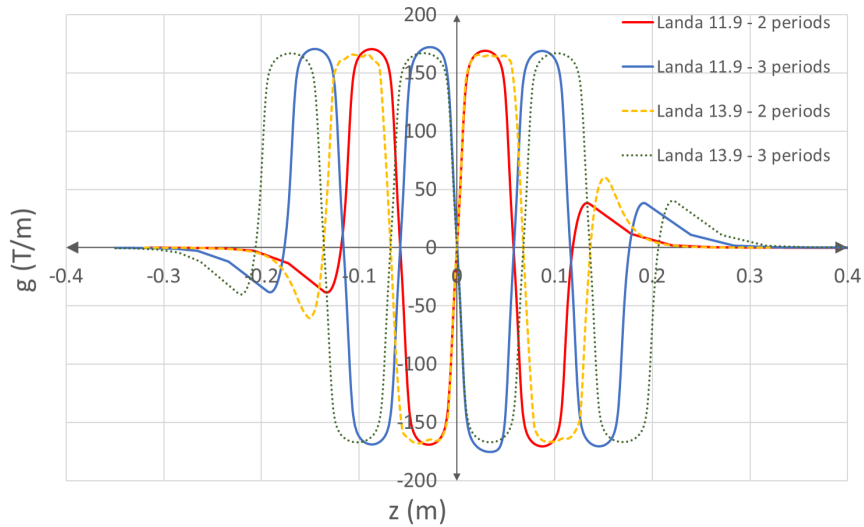


Figure 4.13.: Field gradient g versus longitudinal direction z for $\lambda = 11.9$ and 13.9 cm and different period numbers.

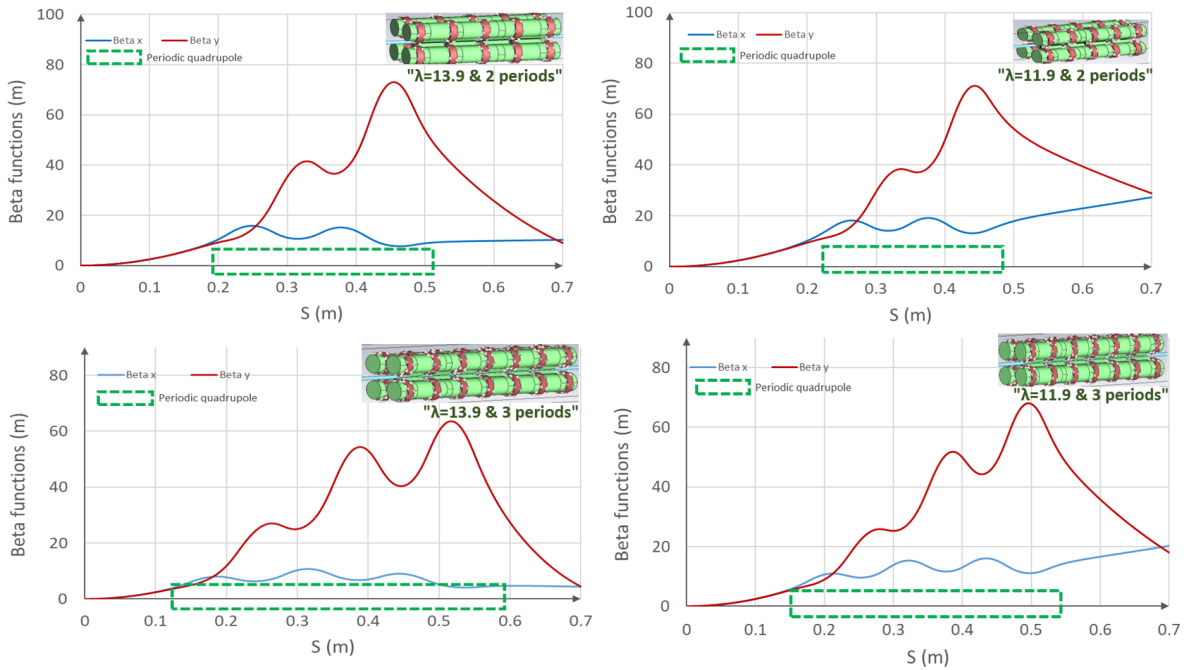


Figure 4.14.: Beta functions β_x and β_y along beam trajectory for models with $\lambda = 11.9$ and 13.9 cm and 2 and 3 periods.

electron beam quite well in both, x and y direction, especially for the cases $\lambda = 11.9$ cm with 3 periods and $\lambda = 13.9$ cm with 2 periods. Selecting these two geometries, in the next step, I extracted beta and alpha functions at the end of the periodic quadrupole and tried to design a dispersive section for

Table 4.3.: Magnet parameters for the periodic quadrupole with $\lambda = 11.9$ cm and 3 periods at 4.2 K.

Parameter	Unit	Value
Magnet Length	cm	39.00
Periodic length	cm	11.90
No. periods	-	3.00
Aperture radius	cm	0.70
Magnetic field gradient	T m ⁻¹	170
Current density	A mm ⁻²	2000

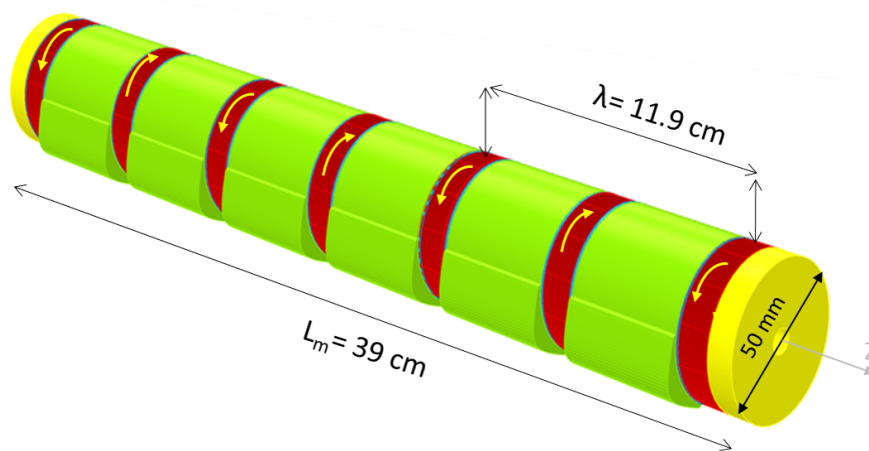


Figure 4.15.: One-fourth of the periodic quadrupole magnet with $\lambda = 11.9$ cm and 3 periods.

these models to provide the TGU with the required input parameters. In this try, after many iterations, it was deduced that the 3-period model can provide the dispersive section with better initial beam parameters leading to the TGU input parameters at the end of the transport line. Consequently, I chose the periodic quadrupole with $\lambda = 11.9$ cm and 3 periods as a substitution for the doublet/triplet section and proceeded to design the transport line which will be discussed in detail in the next section. Figure 4.15 depicts the designed magnet structure, and the magnet parameters are summed up in Table 4.3.

4.2. Transport line

Designing a beamline for the periodic quadrupole is somehow tricky since the periodic shape of the field on the beam path could not be substituted

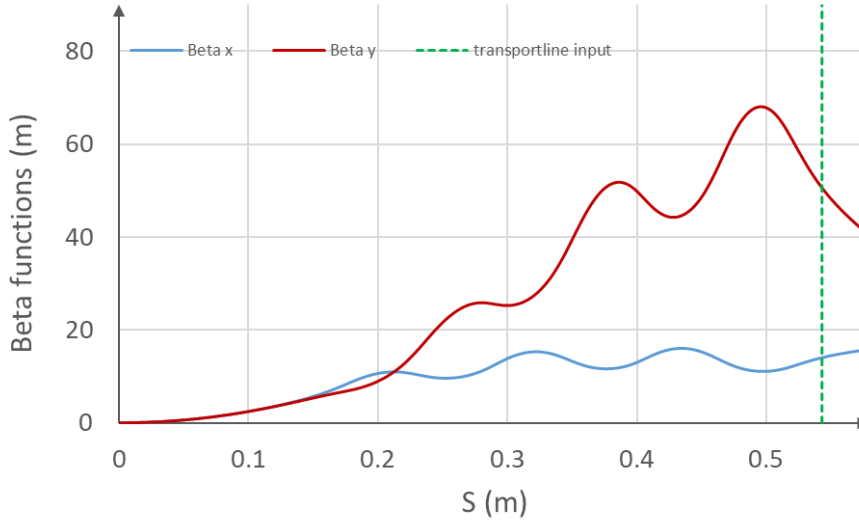


Figure 4.16.: Beam parameters versus beam trajectory from LPA to the end of the periodic quadrupole.

Table 4.4.: Beam optics parameters at the end of the periodic quadrupole at $S = 0.54$ m shown by a dotted green line in Fig. 4.16.

Parameter	Unit	Value
$\epsilon_{x,y}$	π nm rad	10.0
β_x	m	14.04
β_y	m	50.61
α_x	-	-33.72
α_y	-	182.3

with the individual pure quadrupole magnet fields and most of the common beam dynamics codes do not offer the possibility to investigate the beam behavior by inserting the field map. Therefore a combination of the beam dynamics codes, ASTRA and OPA, was used to design a transport line for this periodic focusing magnet.

As discussed before, I used ASTRA software and insert the field gradient distribution of the periodic quadrupole, with $\lambda = 11.9$ cm and 3 periods, to explore the magnet effect on the electron beams, Fig. 4.16. The resulting Twiss parameters at the end of the periodic quadrupole, which is shown by the dotted green line, were extracted and summarized in Table 4.4. The parameters in this table were then inserted into the OPA software to investigate the beam dynamics in the whole transport line at 260 MeV. I

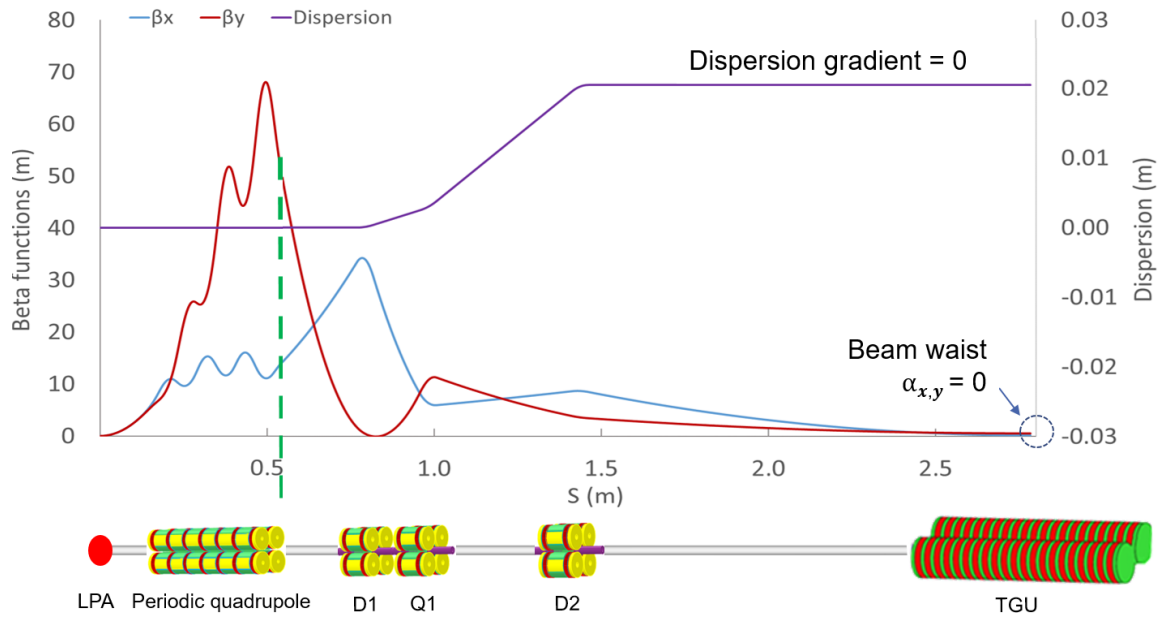


Figure 4.17.: Magnet layout and beam optic parameters along beam trajectory at 260 MeV.

Table 4.5.: Magnet specifications for the designed dispersive section at 260 MeV.

Magnet	position (m)	Length (m)	Defl.angle ($^{\circ}$)	k (m^{-2})
D_1	0.251	0.050	0.9	97.48
Q_1	0.439	0.050	-	-157.76
D_2	0.893	0.050	-0.9	22.92

used the built-in matching algorithm of OPA in a way to fulfill all the TGU input parameters as previously described in Section 3.1.1. In an iterative process a 0.9 m long dispersive section was successfully designed for the periodic quadrupole. Figure 4.17 shows the layout and the optical functions of the dispersive section.

As can be seen in Fig. 4.17, Table 4.5 and Table 4.7, after capturing and collimating the beam with the periodic quadrupole, electron beams go through a combined function dipole *i.e.* a dipole with a focusing quadrupolar component. This dipole magnet generates dispersion and focuses the beam in the horizontal direction x . After 0.138 m there is a pure defocusing quadrupole with quite a high field gradient of -136.72 T m^{-1} which reduces the beam size in the vertical direction, y . The last magnet is another dipole-quadrupole magnet which has the same dipolar field strength of 0.27 T as the

Table 4.6.: Beam optics parameters at the end of the transport line, center of the TGU.

Parameter	Unit	Value
β_x	m	0.2
β_y	m	0.6
α_x	-	0
α_y	-	0
Dispersion	m	0.020

first dipole but acts in the opposite direction. This magnet is located at 0.4 m after the pure quadrupole and has a 19.8 T m^{-1} focusing field gradient which compensates the defocusing effect of the pure quadrupole in x direction. The arrangements and strengths of the magnets are set in a way that the electron beam enters the TGU with a constant dispersion of 20 mm while at the center of TGU the alpha function tends to zero in both planes and beta functions fulfill the TGU requirements. Adding the 0.54 m long section from the LPA to the end of the periodic quadrupole, the whole transport line has a length of 1.44 m at the end of the second dipole. The beam parameters obtained at the end of the transport line are summarized in Table 4.6.

4.2.1. Magnets design

To design the magnets of the dispersive section the magnetic fields and field gradients were calculated from the deflecting angle, magnet length, and quadrupolar strength k , given in Table 4.5, for the design beam energy of 260 MeV. The resulting magnet specifications are summarized in Table 4.7. There are two combined function dipoles and one pure quadrupole, all having the same aperture radius of 7 mm and the same length of 50 mm. iron-core combined function dipoles are usually bending magnets with a non-uniform gap generating a quadrupole component. They produce

Table 4.7.: Magnet specifications at 260 MeV.

Magnet	D1	Q1	D2
Aperture radius (mm)	7	7	7
Magnetic field at the center (T)	0.27	0	-0.27
Magnetic field gradient (T m^{-1})	84.48	-136.72	19.86
Coils current density (A mm^{-2})	500	1000	180

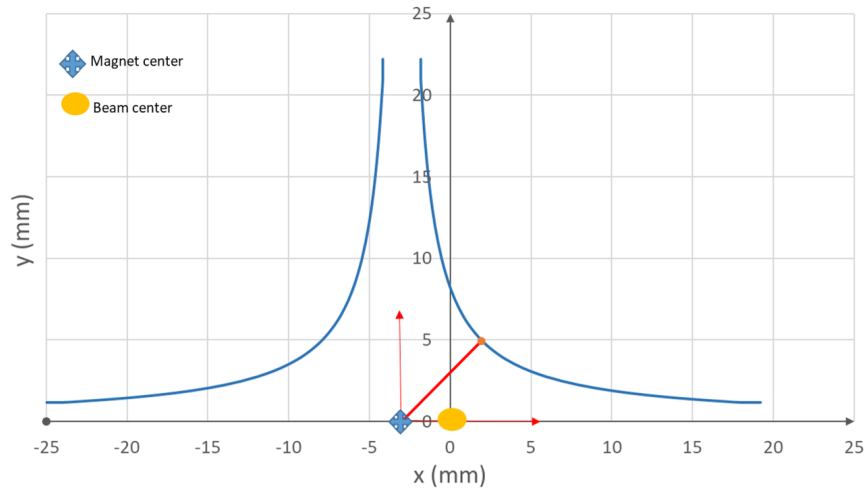


Figure 4.18.: Pole profiles of the combined dipole magnet, the blue rhombus sign shows the offset magnetic center.

a strong field and a weak gradient. Such magnets were built for several accelerators so far, see Section 2.2.5. But combined dipoles with low-field and high-gradient components can not profit from the common method of superimposing the required gradient in the pole shape. In these magnets, an offset quadrupole is usually used, like for the combined magnets at ESRF-EBS [87] and Diamond light source [88] upgrades. In fact, by moving the magnet center from $(0, 0, 0)$ to $(x_c, 0, 0)$ a dipolar field B_0 at the center of the beam, *i.e.* $(0, 0, 0)$, is generated and the field equation can be written as follows.

$$B_y(x) = gx + B_0 \quad (4.1)$$

In Eq. 4.1 B_0 is the dipolar field, g is the field gradient and x is the horizontal distance with respect to the magnet center. In this thesis, to take benefit from the simple coil shape of the periodic quadrupole, I decided to use the offset periodic quadrupole geometry to design combined function dipoles. In order to eliminate the periodic shape of the field in the longitudinal direction, I used half a period of the periodic quadrupole with an offset in the magnet center. As it is shown in Fig. 4.18 and Fig. 4.19, the magnet center of the periodic quadrupole is moved by 3 mm to the left with respect to the beam path to create a dipole field of 0.27 T at $x = 0$. The field and field gradient obtained from simulating this model in Opera [21] is given in Fig. 4.20. The obtained magnetic field has a linear slope in the transverse plane

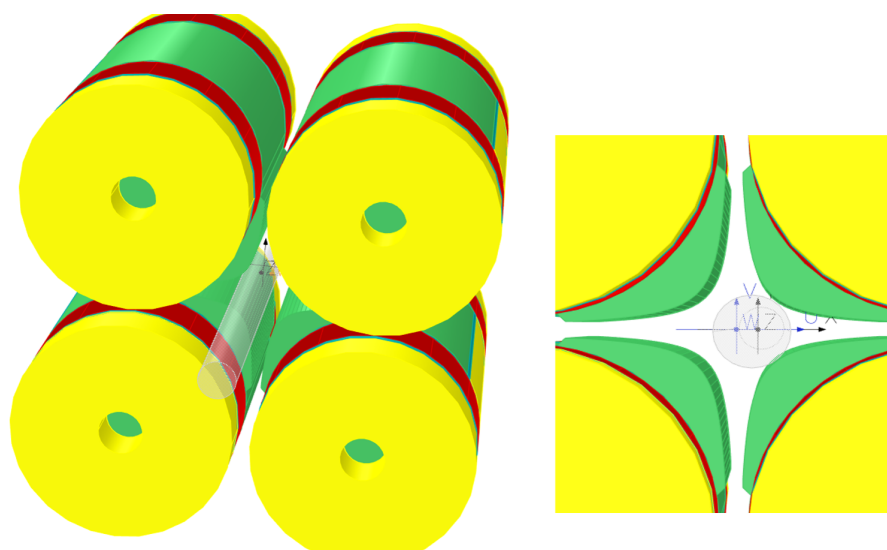


Figure 4.19.: Combined dipole magnet; half a period of the periodic quadrupole with offset magnetic center, X-Y-Z and U-V-W are beam and magnet coordinate systems respectively.

and crosses the $x = 0$ at $B_y = 0.27$ T. In the bottom of Fig. 4.20, the magnetic field as a function of longitudinal position z at $x = 0$ is plotted. It can be seen that there is a constant magnetic field at $x = 0$ for the longitudinal positions near the central part of the magnet but at the coil positions towards the two ends, unwanted fields up to $B_y = -0.3$ T are present. To remove the effect of the two unwanted end fields on the electron beam, high-magnetic permeability materials can be used as shielding around the beam chamber at the two ends, Fig. 4.21. Mu-metals, nickel-iron soft magnetic alloys, are the common shielding material. They have high magnetic permeability which causes the magnetic flux to concentrate in the material. As magnetic permeability is a temperature-dependence property and mu-metals are mainly developed for room-temperature applications, the permeability of these materials begins to drop below -40 °C, making them unsuitable in low-temperature applications. In these cases, applying special heat treatments, cryogenic shielding alloys are developed which are suitable for use at cryogenic temperatures, typically down to 4.2 K, like CRYOPHY® [89]. For this magnet geometry, the magnetic field distribution in the longitudinal direction, for both cases with and without magnetic shielding, is depicted in Fig. 4.22. It can be seen that after placing 4 mm thick shielding tubes at the two ends of the magnet around the beam chamber, the disturbing end fields are eliminated and the electron beam is affected only by the foreseen dipolar

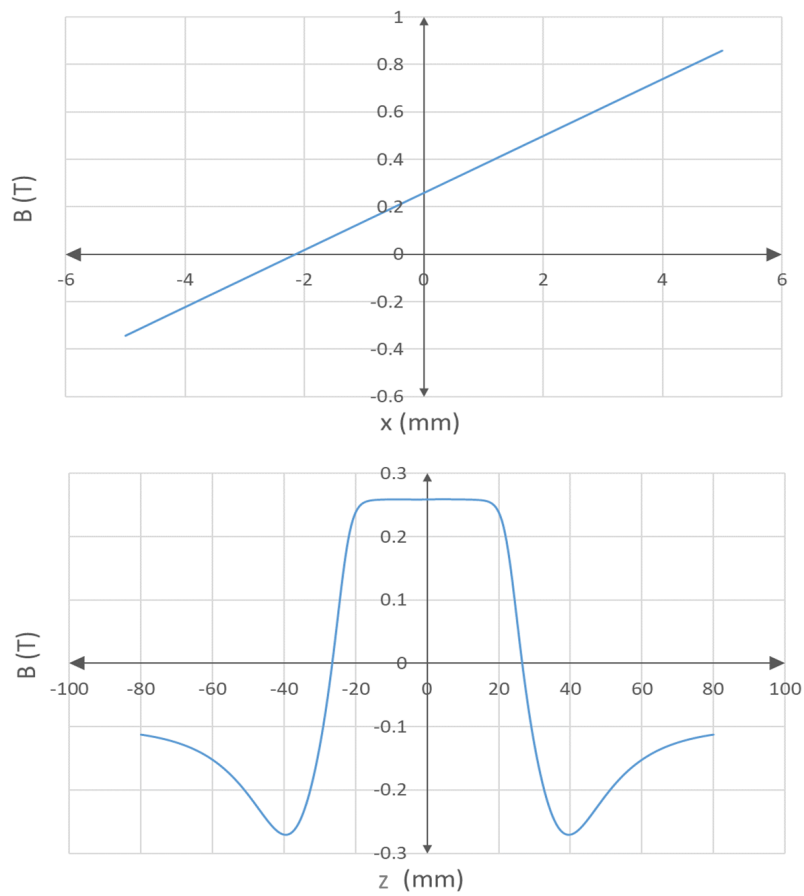


Figure 4.20.: Combined dipole field B_y versus; horizontal direction x at $y, z = 0$ (top) and longitudinal directions z at $x, y = 0$ (bottom).

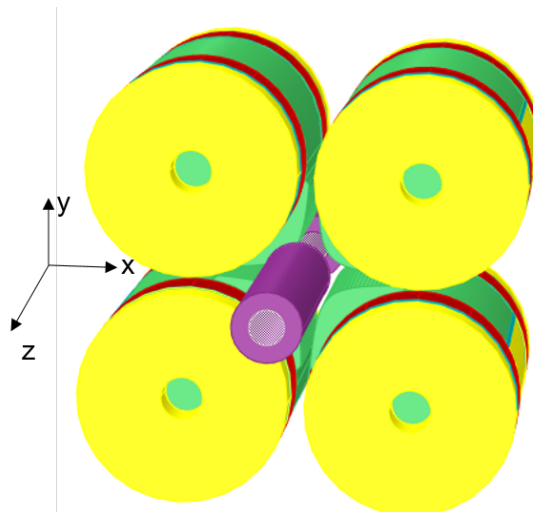


Figure 4.21.: Combined dipole magnet model with magnetic shielding tubes around the beam chamber, colored in violet.

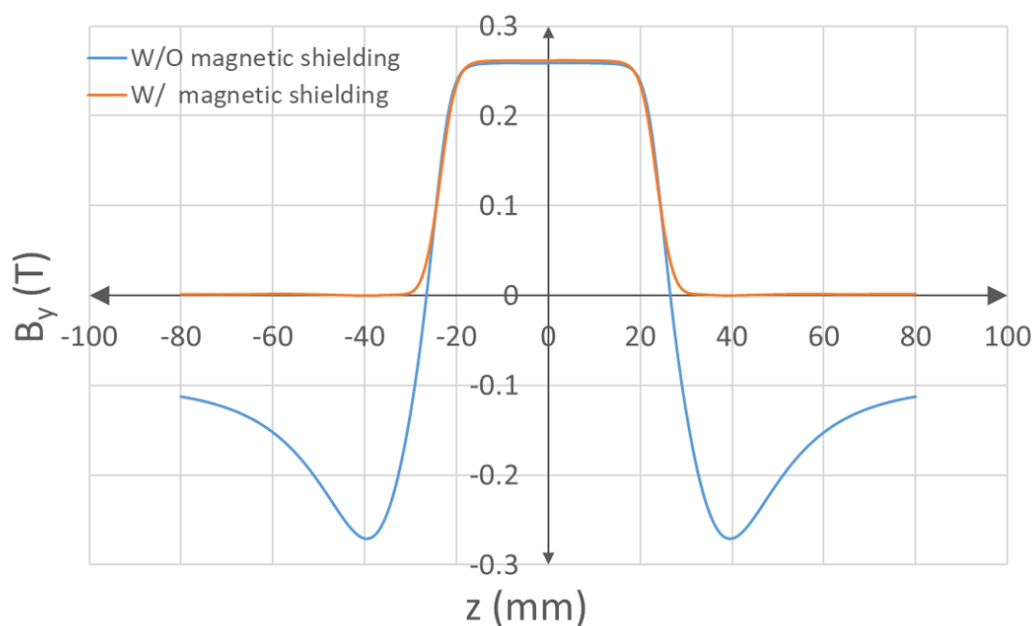


Figure 4.22.: Magnetic field profile in the longitudinal direction at $x, y = 0$, with and without magnetic shielding.

Table 4.8.: Field coefficients of the combined dipole D1, at 5 mm.

n	type	B_n (T)	$B_n / (B_1+B_2)$
1	<i>D</i>	0.27	-
2	<i>Q</i>	0.42	-
3	<i>D</i>	6.17×10^{-4}	8.58×10^{-4}
5	<i>D</i>	1.38×10^{-3}	1.98×10^{-3}
6	<i>Q</i>	-2.93×10^{-4}	-4.07×10^{-4}
7	<i>D</i>	-1.52×10^{-3}	-2.11×10^{-3}
9	<i>D</i>	-1.20×10^{-4}	-1.87×10^{-3}
10	<i>Q</i>	1.36×10^{-3}	1.88×10^{-3}

and quadrupolar fields when passing through the magnet. In addition, using Eq. 2.35, the main field coefficients for the dipole-quadrupole magnet at the normalization radius of 5 mm are calculated and summarized in Table 4.8. Now that a magnet design for the D1 magnet is successfully achieved, the second dipole D2 can be easily designed by decreasing the current density

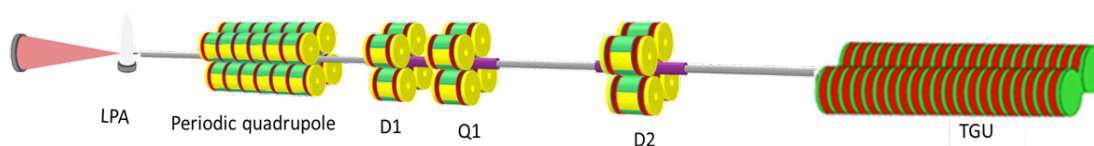


Figure 4.23.: Schematics of the HTS iron-core transport line.

of the coils and using the same design concept as for D1. Moreover, the pure quadrupole magnet in the dispersive section, Q1, will be a non-offset half-period model with the end fields shielded in the same way as in the case of D1 and D2, *i.e.* using mu-metal tubes at the two ends of the magnet around beam chamber, see Fig. 4.23.

4.3. Demonstrator fabrication

As discussed before, the periodic quadrupole geometry has a simple coil shape which eases the coil winding and fabrication process for miniature HTS-coated conductor coils. So the possibilities of prototyping half a period of the magnet in collaboration with Technik-Haus and ITEP at Karlsruhe Institute of Technology have been inspected and a prototype has been realized.

4.3.1. Winding body

In the first step, two optimized designs, A and B, were investigated which are shown in Fig. 4.24 and Fig. 4.25. Design A has the yoke and coil shape we already discussed in Section 4.1.1. It consists of pancake-shaped coils in 73 turns with an inner radius of 21 mm, and an outer radius of 25 mm, see 4.2. Design B has the same iron yoke shape but the coils consist of 1mm width ReBCo-coated disks. This design applies a novel HTS coil winding technique, the disc up-down assembly (DUDA), [90]. In this configuration, there is an opportunity to add more current-carrying disks and increase the magnet strength when desired. The fabrication of a demonstrator for geometry A was scheduled in the first phase and a demonstrator for geometry B is a future plan for this project.

As the protection of a magnet for the high current densities is an issue, it was decided to wind non-insulated (NI) ReBCO tapes on oxygen-free copper parts so that the current is able to bypass the normal zones with very low resistance in a quench event. The key idea of using NI coils is to intentionally eliminate turn-to-turn insulation in a pancake coil, thereby upon a quench, enabling current in the coil to automatically bypass the initial hot spot through turn-to-turn contacts.

To ensure, on the other hand, that the current is kept within the coil and copper bodies, ground electrical insulation is used, as is shown in Fig 4.26. G11 and G10 are usual insulation materials that work well in cryogenic conditions and due to the glass content have a low thermal contraction and high radiation resistance. PEEK is another kind of insulator that can alternatively be used in superconducting applications. It is a high-performance thermoplastic polymer and has a long life, high-temperature resistance, and excellent mechanical strength across a broad temperature range but is more expensive than G10/G11. These days using 3D printing

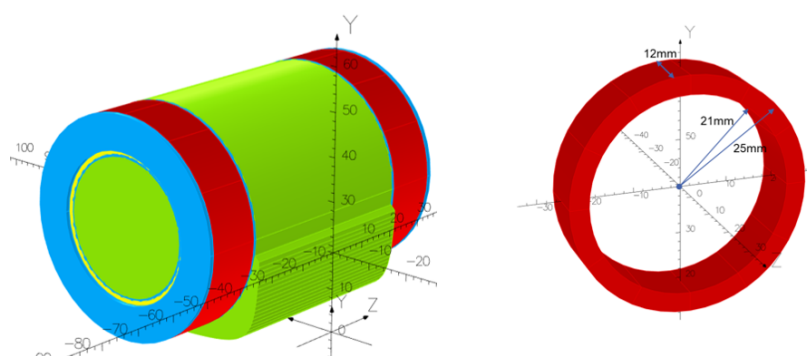


Figure 4.24.: Design A with two 12mm width pancake coils.

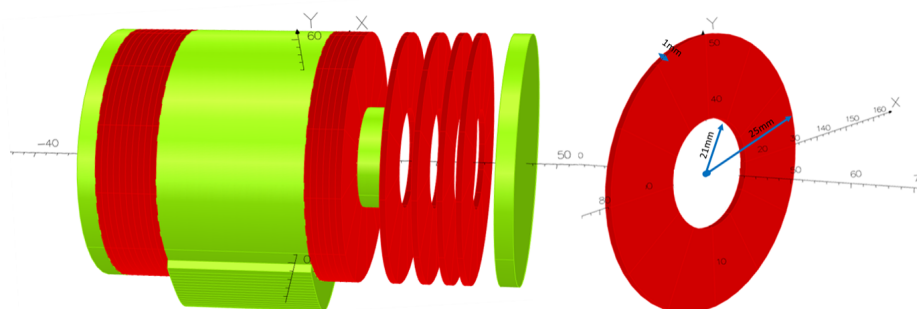


Figure 4.25.: Design B with coils consisting of 1 mm thick ReBCo coated disks.

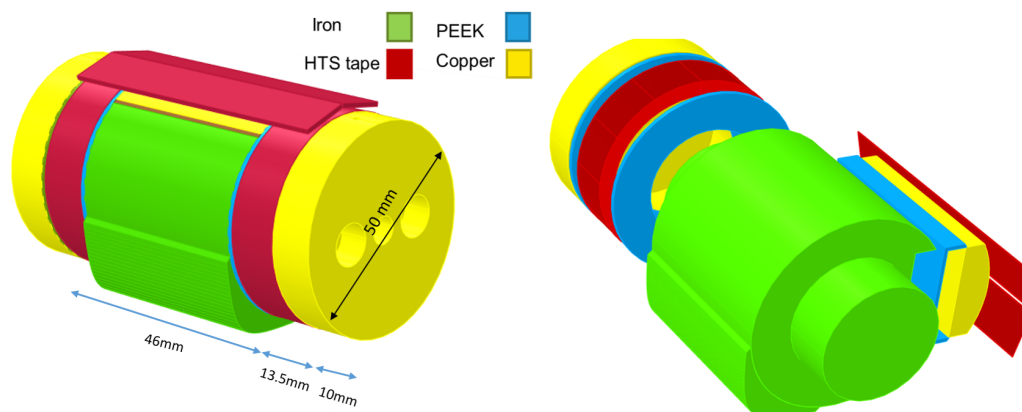


Figure 4.26.: Half a period model designed with Opera 3D, general view (left) and detailed view (right).

PEEK insulators are more commonly used [91], [83] and [92].

In this project, we used PEEK insulators due to the availability of this material during the demonstrator fabrication at Technik-Haus, KIT. As depicted in Fig. 4.26, the iron yoke is insulated from the coils and the copper parts using PEEK insulators and is fabricated using the available structural steel S355JR which shows good magnetic characteristics, close to the magnetization curve of magnetic material XC-06, during powering the coils and magnetic measurement test (see Section 4.3.6). Copper parts, including two end parts and a bridge, are placed on the PEEK insulators beneath the HTS coils and the coils are connected together employing two HTS tapes on the copper bridge in the back yoke. More details on the connection scheme and the winding body can be found in the mechanical drawings, A and Section 4.3.4.

As can be seen in Fig. 4.27 the copper ends are screwed to the iron yoke to support the coils against electromagnetic forces and keep them in their foreseen place.

Fig. 4.28 shows the winding body fabricated at Technik-Haus, KIT. The iron yoke in the front view includes the quadrupole pole profile which shapes the field lines and the back view includes the copper bridge placed on the PEEK insulator.

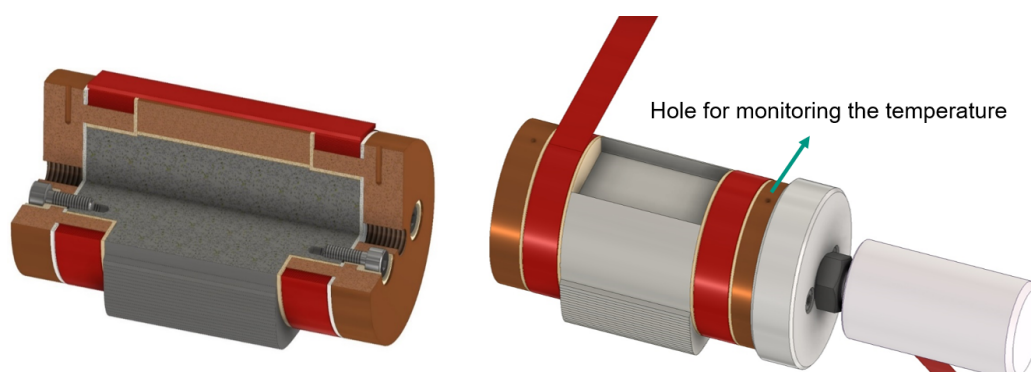


Figure 4.27.: Mechanical model; magnet cross-section (left), and coil winding (right), courtesy of Matthias Eisele, ITEP, KIT.

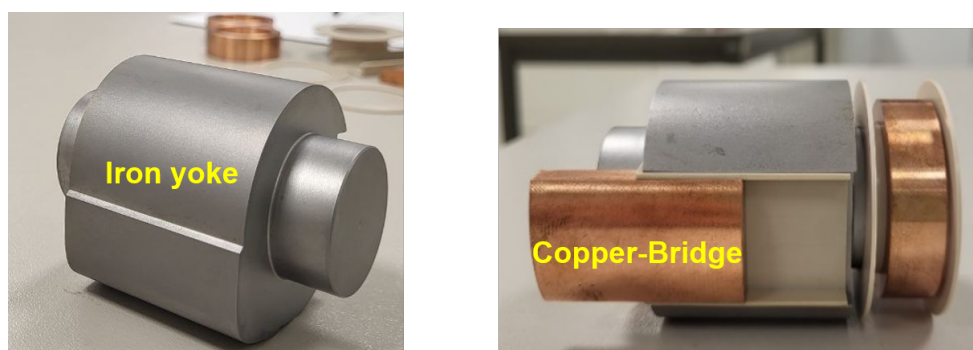


Figure 4.28.: Winding body demonstrator.

4.3.2. Electrical parameters

As discussed before, the demonstrator is half a period of the periodic quadrupole which is designed to work at 4.2 K with a current density of 2000 A mm^{-2} . For the first step, it was planned to power the coils at 77 K in which according to the tape characteristics, provided by the supplier, the critical current (I_c) has a value of 400 A at the self field which is the magnetic field created with a single tape. To find a proper value for the critical current at higher fields, I used the critical current database for different HTS wires and tapes from the website of the Victoria University of Wellington [93]. Considering the worst case of a field perpendicular to the tape face, I extracted the data for critical current per cm width versus applied magnetic field for Superpower tapes and calculated these data for a 12 mm wide tape, which is illustrated in Fig. 4.29 together with the load line derived from the Opera simulations. The intersection of these two graphs gives an estimate of the critical current which is around 135 A. At

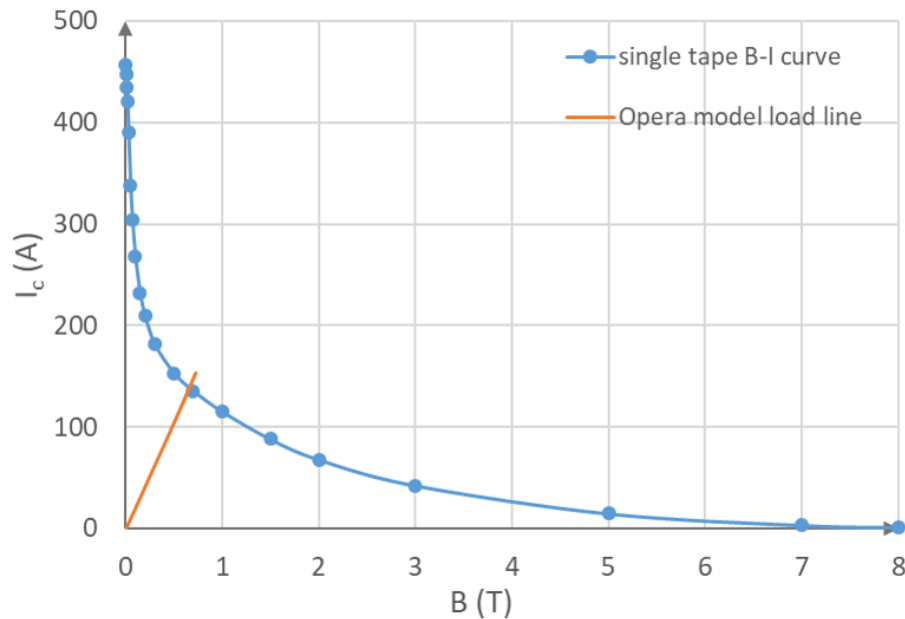


Figure 4.29.: Critical current I_c versus magnetic field B for 12 mm wide tape at $T = 77$ K, [93].

Table 4.9.: Electrical parameters for the demonstrator coils.

Parameter	Unit	Value at 4.2 K	Value at 77 K
Current per coil	A.t	96000.00	9771.84
No. turns	-	72.00	72.00
Current per turn	A	1330.00	135.72
Current density	$A\text{ mm}^{-2}$	2000.00	203.58

this point, using the current of 135.72 A per tape leads to a critical current density of 203.58 A mm^{-2} for the SCS12030-AP ReBCO tape with 12 mm width and 0.055 mm thickness. The coil specifications are already given in Table 4.2 and the electrical parameters for powering the coils at liquid nitrogen and liquid helium temperatures are summarized in Table 4.9.

4.3.3. Force calculation

To check the mechanical layout of the demonstrator, before fabrication and coil winding, the fields and forces were investigated on the coils as well as on the HTS bridge tapes. The force calculation is done using the magneto-static solver of the Opera simulation code. The simulated model is

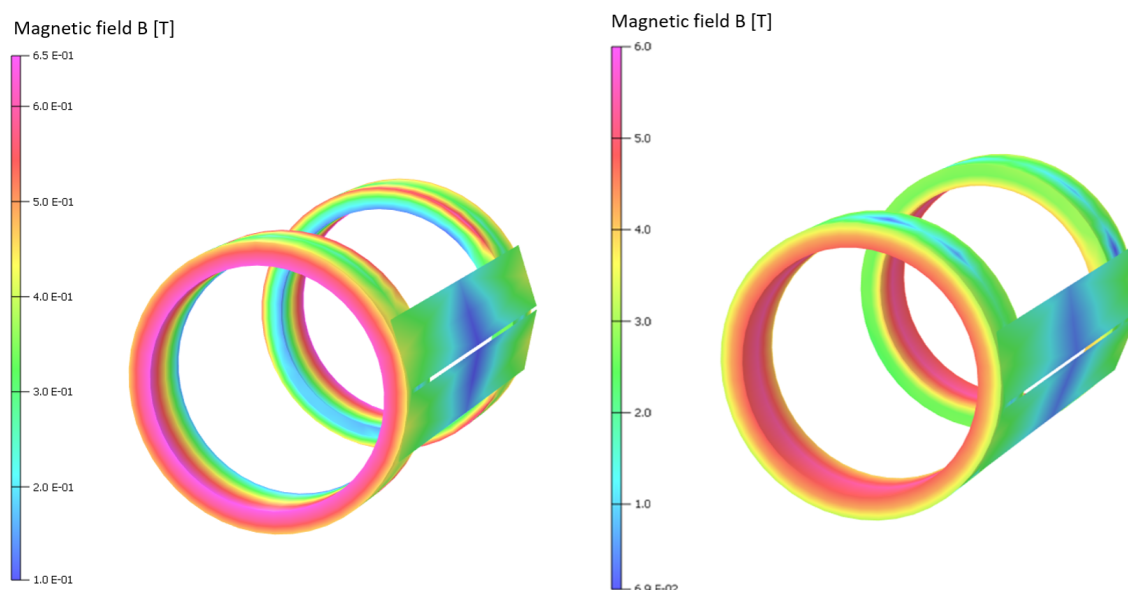


Figure 4.30.: Magnetic flux density on HTS bridge and coils at 77 K (left) and 4.2 K (right).

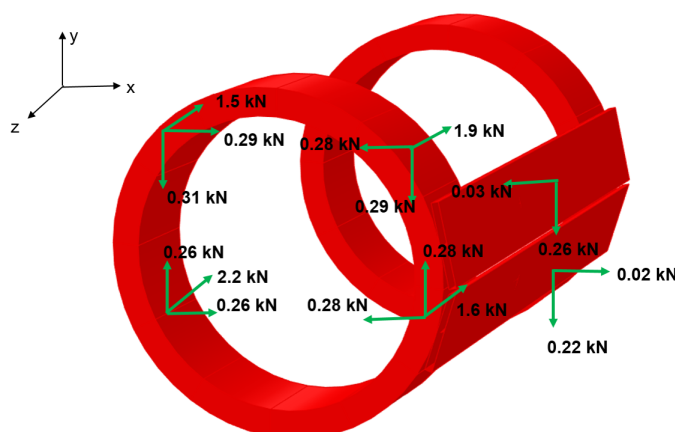


Figure 4.31.: Lorentz forces on coils and HTS bridge at 4.2 K.

one-fourth of half a period of the periodic quadrupole, the same geometry as the demonstrator. The calculations are done for 4.2 K and 77 K temperatures, using the currents given in Table 4.9, and the calculated magnetic field on the HTS coils and tapes are shown in Fig. 4.30. It can be seen that the computed magnetic field on the coils B_{cond} is less than 0.65 T and 6 T at 77 K and 4.2 K, respectively. Also as illustrated in Fig. 4.31 the maximum force to the coils is in the longitudinal direction, z , which in total is equal to 7.7 kN on each coil. These longitudinal forces are stopped in this model by the iron yoke and the two copper ends. For the HTS bridge tapes which connect the coils together, the forces in the longitudinal direction, F_z are nearly zero,

and the transverse forces, F_x and F_y , have the maximum value of 0.26 kN in the vertical direction which is small and can be neglected. Nonetheless, it was foreseen to fix the HTS bridge tapes to the copper bridge from the upper side with a Kapton tape that can work against the transverse forces.

4.3.4. Coil winding

To proceed with the demonstrator fabrication and winding the two coils, 22 m of the 12 mm-width SCS12030-AP ReBCO tape was procured from Superpower Inc. [39]. HTS coils were wound on the copper winding bodies with the superconducting layer faced up, *i.e.* the substrate side lays on the copper body. To fix the coils to the copper bodies and also to make the electrical connection between the HTS coils and the HTS tapes on the bridge, soldering was used. The inner turn of the HTS-coated conductor for each coil was soldered to the copper using Sn60Pb40 solder wire with a melting point of 183°C. Sn60Pb40 is a high-purity alloy that is composed of 60% tin and 40% lead alloy. To do the soldering, the copper body was first heated to a temperature higher than the melting point of the soldering wire. The heating process used two heating rods that can create a 400 W heating power in total. This heating structure was placed beside the copper body, on the winding machine, and increased the copper body temperature to more than 200°C in less than 10 minutes making it ready for the soldering. Then by applying the solder wire and flux, a smooth soldered face on the copper body was created, Fig. 4.32. The next steps were soldering the tape surface, placing the soldered face of the tape on the soldered copper body, heating them up, and finally cooling down such that the first-turn tape is well attached to the copper body, Fig. 4.33. After soldering the first turn to the copper body, the winding was continued till 72 turns were wound. The last step before dismounting the coils from the winding machine was the outer turn soldering using indium-based low-temperature soldering wire Sn50In50, Fig. 4.34. In this step, the middle part of the last turn was soldered to the penultimate turn and for this, the whole coil was heated up to the melting point of Sn50In50 which is 118°C. During the heating process, the temperature on the tapes was kept below 200°C to protect the HTS tape. In fact, at higher temperatures, the oxygen content in the superconducting layer is reduced, resulting in a degradation of the

superconducting properties [94]. Using the described procedure both coils were wound successfully. Figure 4.35 shows the two wound pancake coils assembled on the iron yoke. The final phase in winding the coils was connecting the two coils by soldering the end turn of each coil to the two HTS bridge tapes. To minimize the joint resistance on the soldering surface, the HTS face of the HTS bridge was soldered to the HTS face of the last turn tape. The first idea was to solder the HTS tapes to the copper bridge and then solder the two winding ends to these HTS tapes on the bridge. To do this a fixture to hold the copper bridge was fabricated but due to the curved shape of the copper bridge the tapes were not well soldered to it, see Fig. 4.36. Finally, the last winding turns were soldered to the two HTS bridges on a heating plate, and the HTS bridge tapes were fixed on

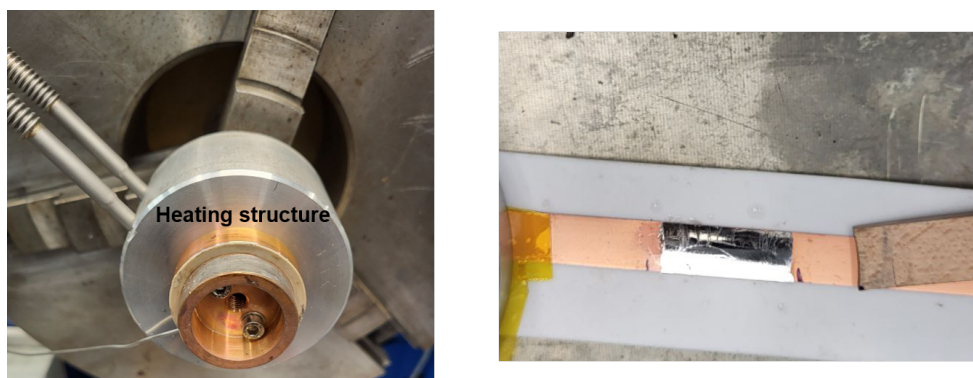


Figure 4.32.: Soldering the first turn of ReBCO tape on the copper body.

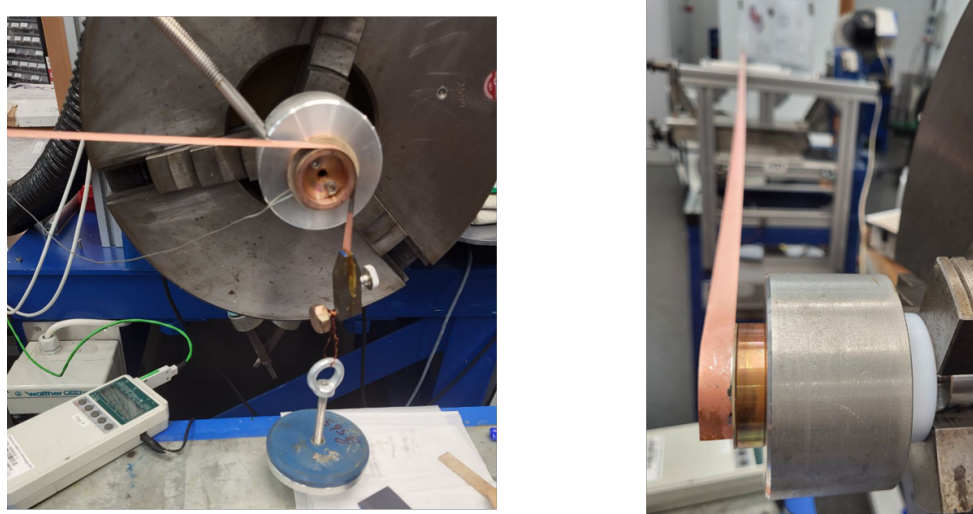


Figure 4.33.: Placing the soldered face of the tape on the soldered copper body.

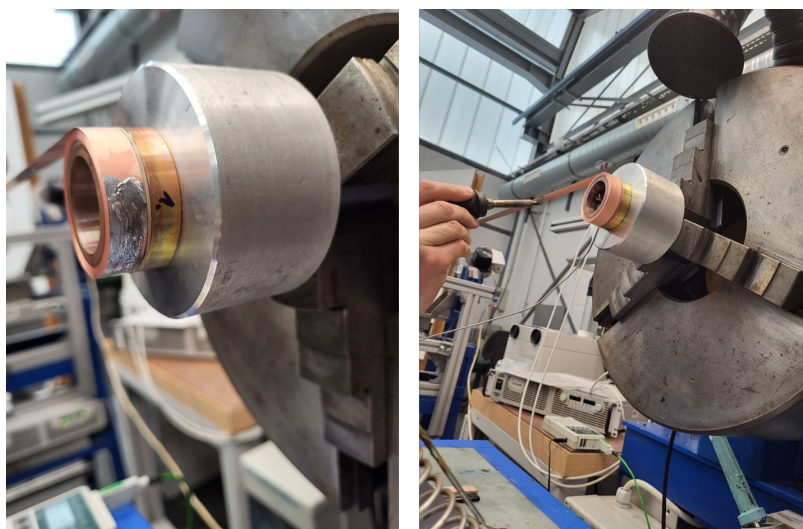


Figure 4.34.: Last turn soldering.

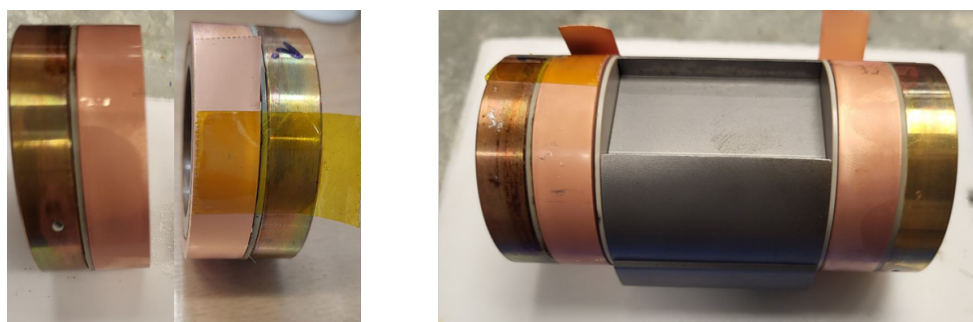


Figure 4.35.: Wound pancake coils.

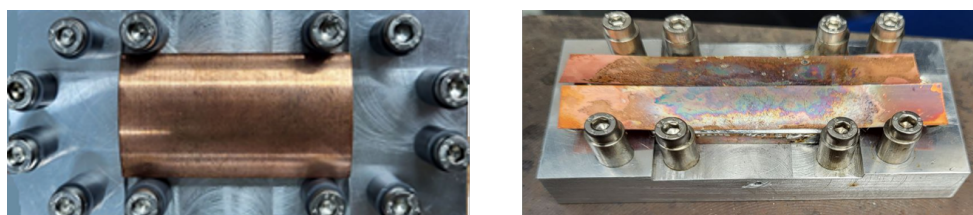


Figure 4.36.: Copper bridge (left) and HTS tapes on the copper bridge (right).

the copper bridge using Kapton tape instead of soldering, Fig. 4.37 and Fig. 4.38. Two copper wires as voltage taps (V-taps) are placed on each coil, as can be seen in Fig. 4.38, to measure the voltage during the powering test.

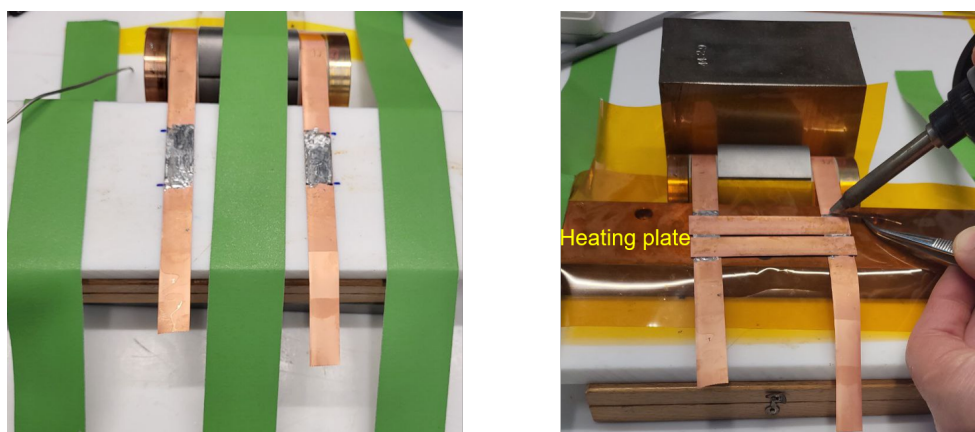


Figure 4.37.: Soldered end turns (left) and soldered HTS bridge tapes on Soldered end turns (right).

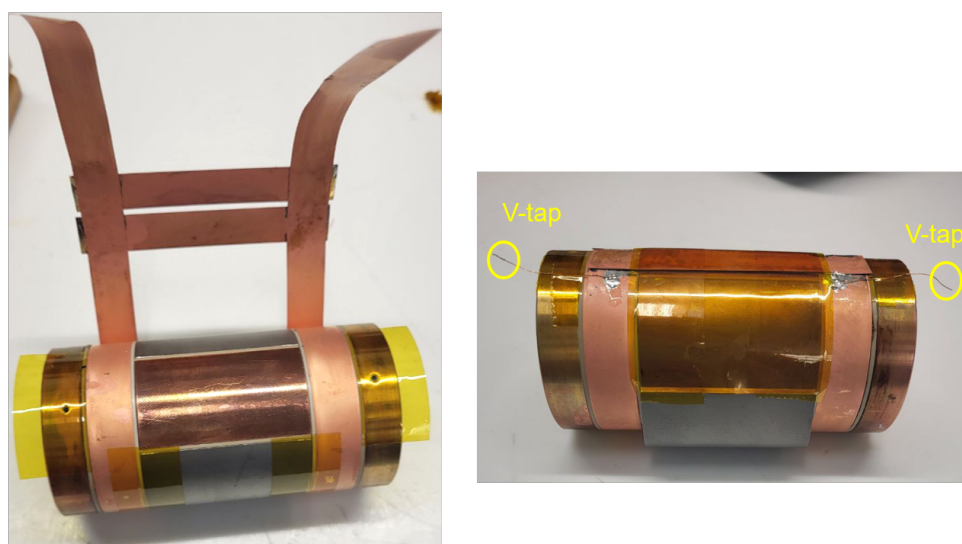


Figure 4.38.: Magnet demonstrator.

4.3.5. Powering of the coils

After completion of the winding process, the coils were powered and tested at $T = 77$ K inside an insulated box using the current leads of the CASPER I cryostat at KIT. To measure the voltage of the coils, the V-tap on each coil was soldered to a longer wire. Also, the voltage of two ends of the demonstrator was measured by clamping two wires between the current leads and copper ends. As is shown in Fig. 4.39, the pink and blue wires were connected to the most positive and most negative voltage ends, respectively, while the red and yellow-brown wires were connected to the positive coil and negative coil, sequentially. Using the four-channel voltage

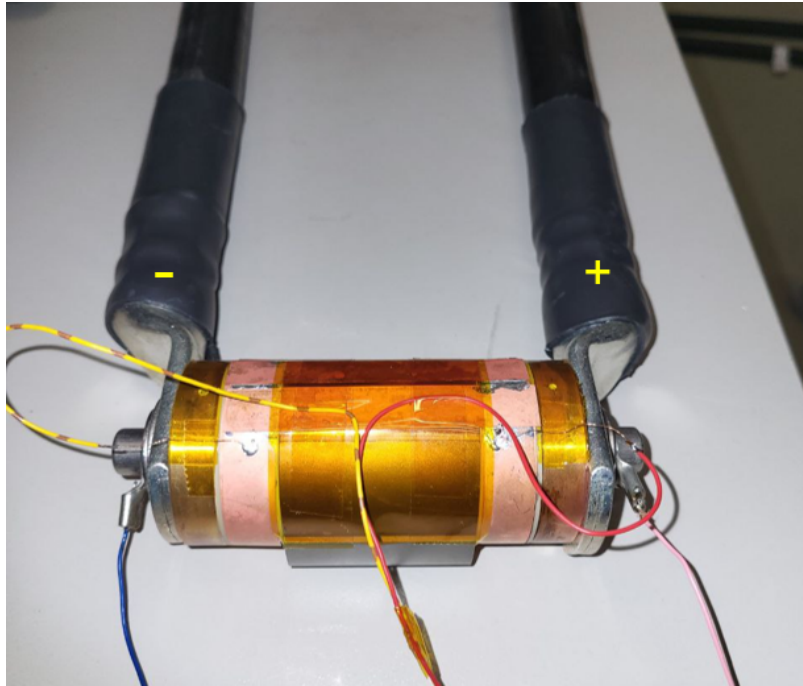


Figure 4.39.: Current leads (black arms) and voltage measurement wiring.

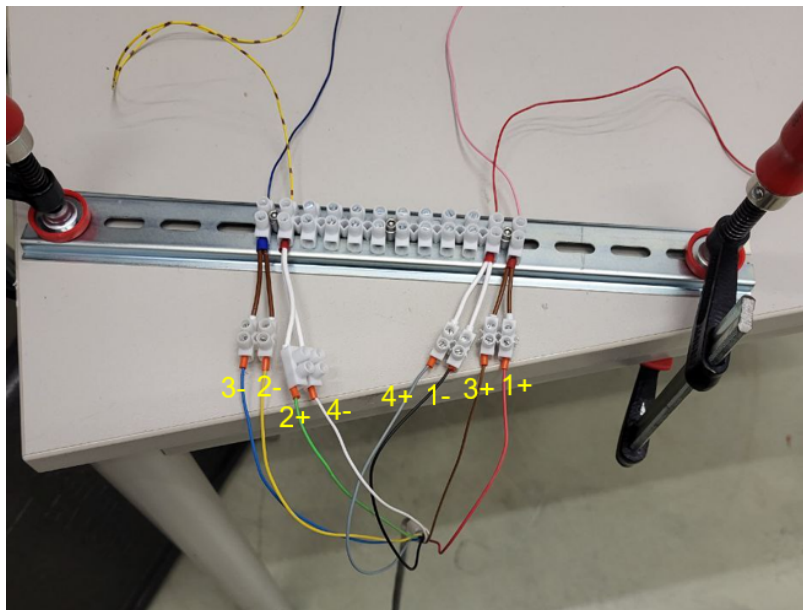


Figure 4.40.: Voltage measurement channels.

measurement as illustrated in Fig. 4.40, I could measure the voltage on channels one and two for coil I and coil II, respectively. Channel three was related to the two ends' voltage, and channel four was used for the bridge voltage measurement. After connecting the coils to the power supply and



Figure 4.41.: Powering setup.

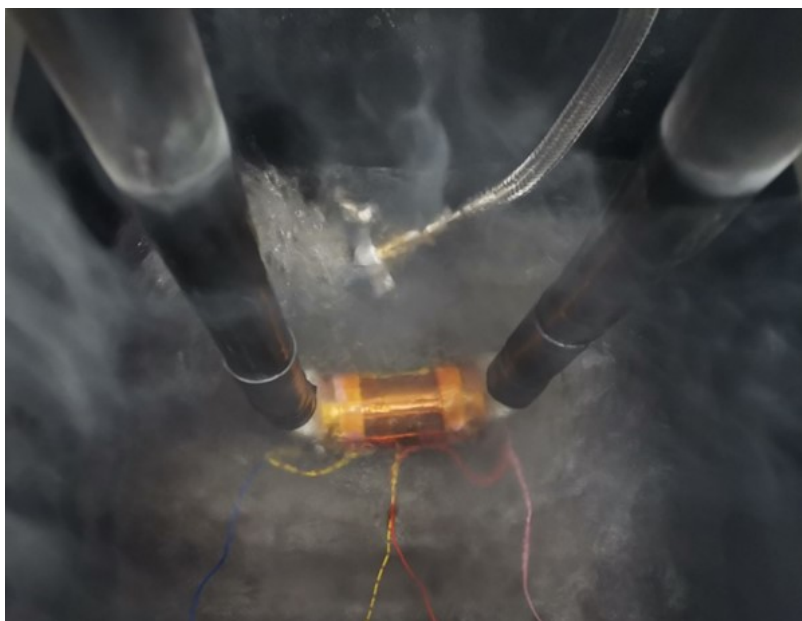


Figure 4.42.: Hanging the demonstrator in a box filled with LN_2 .

voltage measurement device, the final experimental setup was prepared. The demonstrator was hung in an insulated box using the CASPER I current leads. Then the box was filled with liquid nitrogen until the coils and the whole demonstrator were well-immersed, see Fig. 4.41. In Fig. 4.42 the experimental setup for powering the coils is shown. The black box is the

insulated box, containing liquid nitrogen and the demonstrator. On the right-hand side is the liquid nitrogen container which was used to fill in the black box whenever the coolant level is low. Also, the CASPER I cryostat can be seen on the left side, of which in this experiment we just used the power leads. After cooling down the coils in LN₂, the powering process was started at 77 K. The coils were powered to 150 A, using a current ramping rate of 10 A min⁻¹. In this experiment, as can be seen in Fig. 4.43, the voltage over each coil showed a linear dependence on the current up to 125 A and 122 A for coil I and coil II, respectively. This constant slope is pointing to the V-taps wires, end wires, and soldering resistances which are in total of the order of a few $\mu\Omega$ at 77 K for both coils. Also, it can be seen that these ohmic resistances are different for the two coils and coil II reaches its critical current a few amperes sooner than coil I, that is 122 A. This can be due to the different contact resistances between tapes in coil II with respect to coil I which is unwanted inaccuracy during the winding process. By subtracting the V-taps and wiring resistances and related voltage values, the measured voltage over coil I and coil II versus current is obtained as depicted in Fig. 4.44. By ramping up to the critical current values 125 A and 122 A, there is approximately zero resistance for the two coils. If the current is further increased a resistance appears. In fact, by increasing the current each turn reaches its critical current, and by filling up the turns the current flows radially within the non-insulated turns. In this powering test, in spite of having the radially flowing currents for current values higher than I_c , the coils were powered successfully up to 120% of the critical current, *i.e.* 150 A. After ceasing the current ramping, due to the non-insulated tape turns, the current needs time to exit the superconducting path and there would be a current/voltage decay, as can be seen in Fig. 4.43 at the $t = 926$ s. Also, to investigate the functionality of the demonstrator assembly for creating the desired magnetic field, a magnetic measurement was done which is discussed in the next section.

4.3.6. Magnetic measurements

To evaluate the coils functioning in generating the required magnetic field a magnetic measurement was performed. Since the demonstrator is one-fourth of a quadrupole, a valid measurement was to measure the pole tip

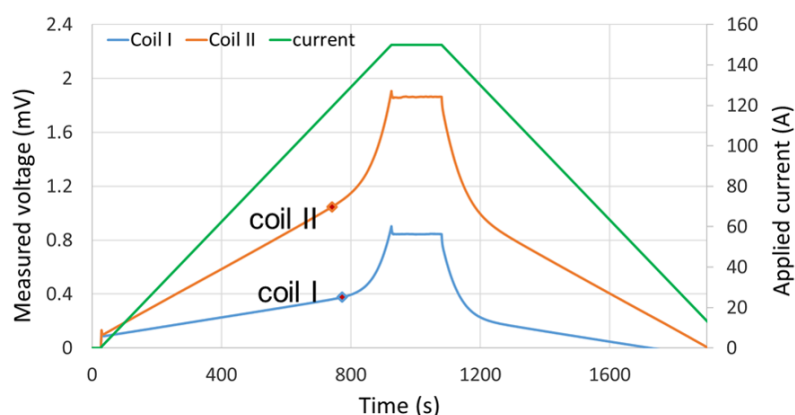


Figure 4.43.: Measured voltage and current over coil I and coil II, versus time.

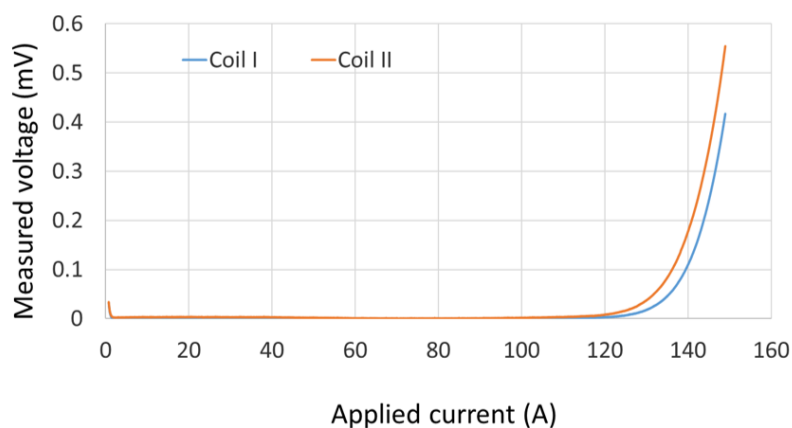


Figure 4.44.: Measured voltage over coil I and coil II versus current, values are corrected to the normal conducting parts' resistances.

field at the longitudinal center of the quadrupole, *i.e.* at $z = 0$. To do the magnetic measurement the following setup was arranged: as it is shown in Fig. 4.45, the demonstrator was fixed on a G10 plate at the two ends, by wrapping two fixing bands on the copper ends. On the central plane of the magnet, two screwed rods were placed on the two sides in which a small rectangular G10 plate could be moved up and down above the pole profile. A Hall probe was glued at the center of this plate which by moving the plate down to the pole profile, could measure the field on the pole tip. More information about the Hall probe structure and its functionality was described before and can be found in Section 2.4.1. After preparing the setup, the four electrodes of the Hall sensor were connected to four wires, two of which fed the hall sensor with a 10 mA current, and the other two were used for measuring the Hall voltage. The Hall probe used was a high

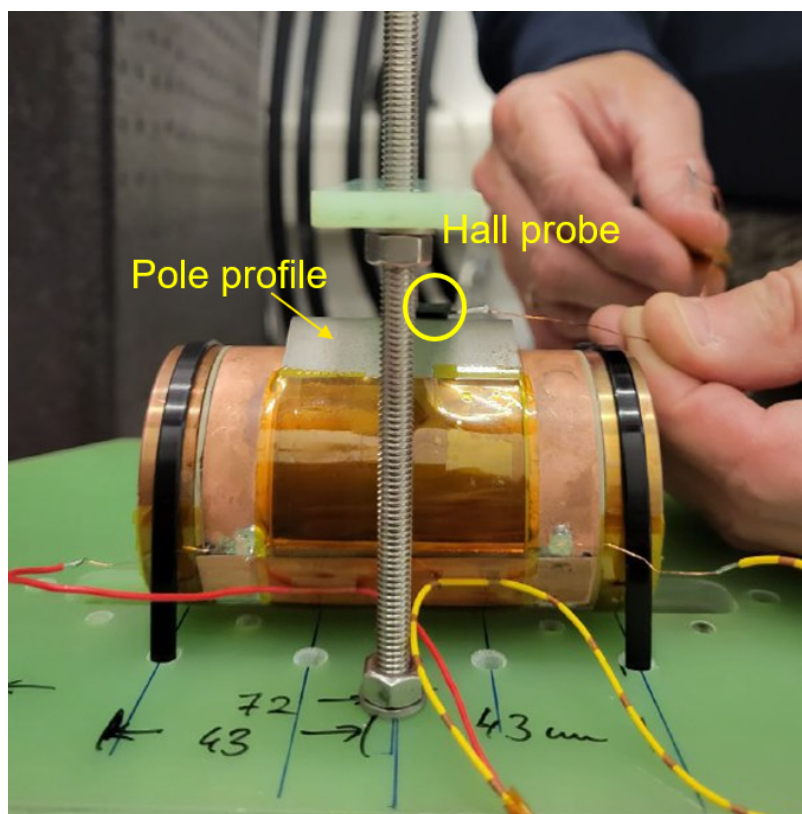


Figure 4.45.: Field measurement setup.

Table 4.10.: Hall probe specifications used for magnetic measurement.

Parameter	Unit	77 K	4.2 K
Nominal control current, I_n	mA	10	10
Sensitivity at I_n	mV T^{-1}	140.2	140.7
Offset voltage at I_n	μV	-393	-
Input resistance	Ω	73	-
Output resistance	Ω	63	-

linearity Hall probe for room and cryogenic temperatures, the HHP-VP model by Arepoc s.r.o., Bratislava, Slovakia, with an operating temperature range of 1.5-330 K, [95]. The Hall probe specifications at 77 K and 4.2 K are summarized in Table 4.10. To start the magnetic measurement, the whole sample was placed in the black insulated box which was filled with liquid nitrogen. Then the coils were ramped up with a ramp rate of 30 A min^{-1} in 15 A steps. Between every two steps, the current was kept constant for 200 s to have a stable Hall probe voltage, because of the non-insulated tapes which lead to a voltage decay. Figure 4.47 illustrates the applied current

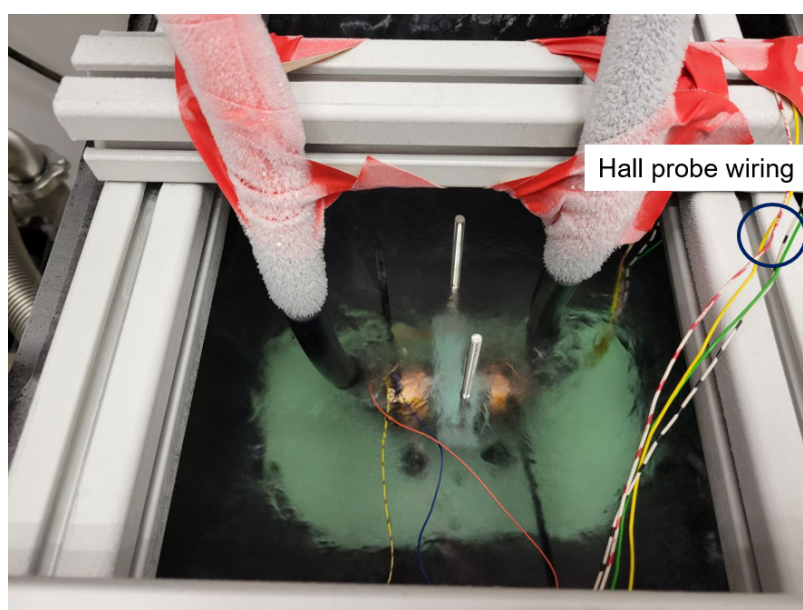


Figure 4.46.: Field measurement setup with the current leads and voltage measuring wires in liquid nitrogen.

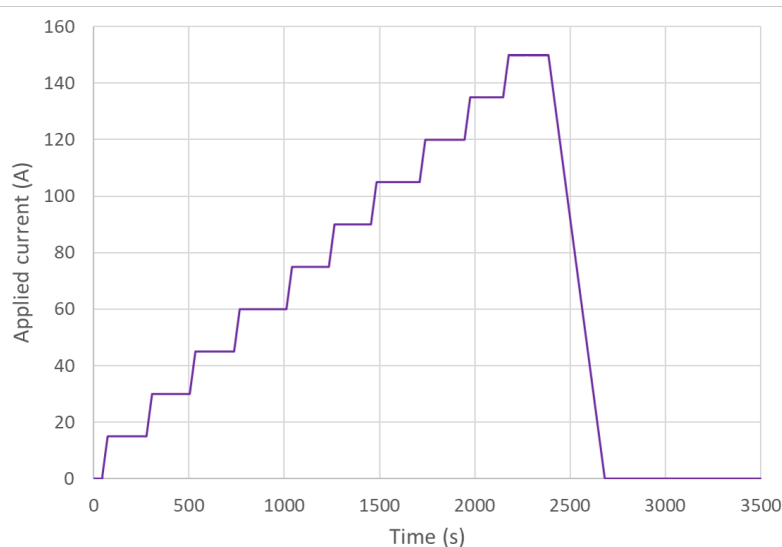


Figure 4.47.: Load current vs. time for Hall probe measurement.

versus time. During powering the coils, the Hall probe with a 10 mA current was placed perpendicular to the magnetic field generated by the coils and delivers an output voltage that is proportional to the magnitude of the magnetic field. For calculating the perpendicular magnetic field from the Hall voltage V_H , offset voltage V_{off} of the Hall probe should be determined at zero current. The offset voltage is generally due to imperfections of

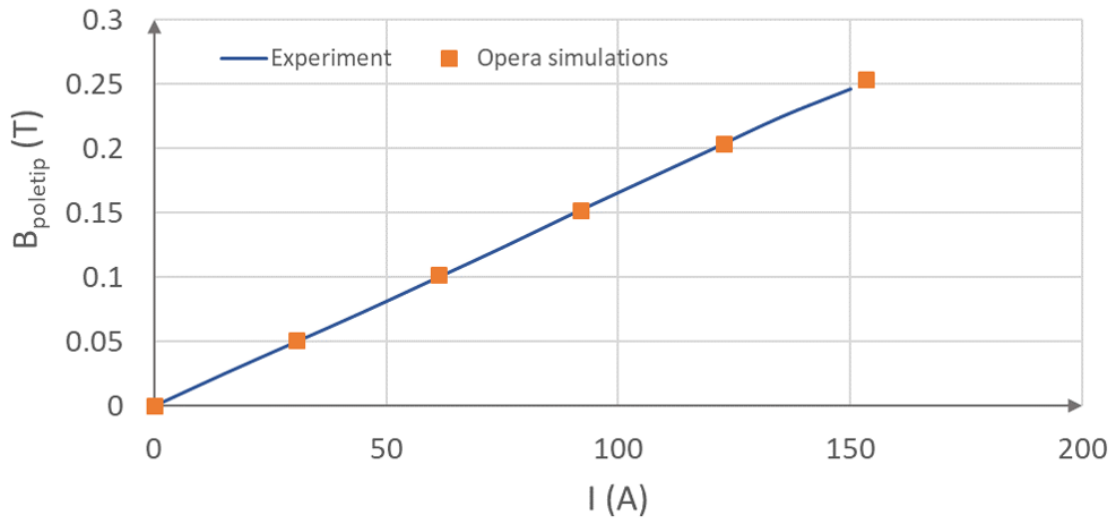


Figure 4.48.: Magnetic field on pole tip $B_{Poletip}$ vs. applied current, obtained by Hall-probe measurement and Opera simulation.

the manufacturing process, inhomogeneity of materials, misalignment, and asymmetry of the Hall probe contacts. In our experiment, the offset voltage V_{off} was obtained to be 1.7 mV. By subtracting the offset voltage from the measured voltage and dividing the obtained value by the Hall probe sensitivity at $T = 77$ K, see Table 4.10, the measured magnetic field was calculated. Also because of placing the whole setup well-immersed in the coolant, all the voltage leads and connections are kept at the same temperature and the thermo-electric voltages are negligible. According to the Hall probe data sheet which was provided by the manufacturer, the overall thickness of the hall sensor is 1.1 mm. Therefore, to compare the measurement with the simulation results, the Opera results were calculated at 0.55 mm distance from the pole tip of the magnet. Figure 4.48 shows a comparison of the measured and simulated magnetic field versus the applied current which shows a very good compatibility. In addition, the linearity error is up to 0.2% which is too small to affect the obtained results. Moreover, the next phase of the experiment which is not included in this thesis will be powering the coils and doing the magnetic measurement at liquid helium temperature in which the coils are planned to be located inside the CASPER I cryostat.

5. Fixed field alternating gradient transport line

Fixed Field Alternating Gradient (FFAG) accelerators are accelerating structures in which the magnetic fields are fixed with time and are not ramped up with energy. These accelerators were first conceived in 1950 to reduce the radius in circular accelerators and cyclotrons. To reduce the radius a field gradient was introduced in the dipole magnets but these dipoles with quadrupolar components focus the beam in one plane, say horizontally, and defocus in the vertical direction. To overcome this "alternate gradient focusing" was proposed. Therefore, the magnets in FFAGs create time-constant fields and are split up into focusing and defocusing elements. Some advantages of such accelerators are simple power supplies and no synchronization issues, the possibility to accelerate the particles as fast as the RF allows, and high repetition rates *i.e.* high average currents. In fact, the FFAG accelerator is a class of circular accelerators that combines properties of both the cyclotron and the synchrotron. It uses a magnetic field that is constant in time, a 'fixed field', together with an increased focusing strength achieved using the 'alternating-gradient' principle. The first FFAG accelerators were scaling ones in which the particles' orbit scales with the energy. Scaling and non-scaling designs are proposed for many applications: proton acceleration for cancer treatment like in the PAMELA project, [96], muon fast acceleration for a neutrino factory [97], and electron acceleration like the Electron Model of Many Applications (EMMA) which is a non-scaling ring [98]. Most of the FFAG accelerators are circular machines, although there are few projects in which the particles are guided in an FFAG-based transport line with no overall bending like the scaling FDDF (where F stands for horizontally focusing, D for horizontally defocusing) transport lines for proton beams presented by Machida and Fening in 2010 [99] and the FDF design proposed by Lagrange et al. in 2012 [100]. A straight FFAG section would be indeed an asset. The first

obvious application would be a straight beam line with a large momentum acceptance that relies on the energy separation in the transverse position and leads to the same optical behaviors for locally dispersed particles with different energies which is similar to what we have in the TGU.

In this part of the thesis, an investigation into the design of an FFAG transport section is presented in which this transport section is considered as a means of transportation of the large energy spread electron beams to a specific target while keeping the same optical parameters at the start and end of the section. Although the ultimate goal of this project would be to design a compact transport line with a high energy acceptance using the HTS FFAG concept that would be the next phase of this work.

Scaling FFAG A scaling fixed field alternating gradient (FFAG) accelerator has a large momentum acceptance despite the fact that magnetic guiding fields are constant in time and therefore can be a candidate to be used for LPA electron beams. Looking at Eq. 2.13, one can see that if the gradient g remains constant, the quadrupole strength, k will decrease as the energy of the particle increases. This will cause optics mismatch and can lead to beam loss. To prevent this problem we should have,

$$\begin{aligned}\frac{\delta\rho}{\delta p} &= 0 \\ \frac{\delta k}{\delta p} &= 0\end{aligned}\tag{5.1}$$

where ρ and P are particles' orbit radius and momentum, respectively. According to the above equations in scaling FFAGs the orbit shape should be the same for different energies and also k should be independent of the energy variations which means that the field gradient should be alternating. To satisfy the mentioned scaling optics in a beam transport line, special combined function magnets are required in which the vertical magnetic field, B_y , is a function of x^K , where x is the horizontal coordinate and K is the field index and is a measure of the momentum compaction. For the higher K values, the equilibrium orbits of particles with different energies are closer together, [99, 101].

$$B_y(x, z) = B_{y_0} \left(\frac{x + x_0}{x_0} \right)^K F(z)\tag{5.2}$$

The function $F(z)$ describes the longitudinal distribution of the field which is unity at the magnet center and tends to zero far from the magnets and is

Table 5.1.: Parameters of an FDDF cell, [99].

Parameter	Unit	Value
Reference radius, x_0	m	1E+6
Field index K	-	5E+6
B_{y_0} for F magnets	T	2.0
B_{y_0} for D magnets	T	3.0
C_1, C_2, C_3, C_4, C_5	-	0.1455, 2.2670, -0.6395, 1.1558, 0, 0
g	m	0.15

defined as follows

$$F(z) = \frac{1}{1 + \exp(\sum_{i=1}^5 C_i (z/g)^i)} \quad (5.3)$$

where C_i s are the Enge coefficients that determine the falloff function and g is a constant value. Also, for the beam transport lines as the reference radius x_0 is much bigger than the horizontal position x , equation 5.2 can be written as

$$B_y(x, z) = B_{y_0} \exp\left(K \frac{x}{x_0}\right) F(z). \quad (5.4)$$

So using scaling FFAG magnets that obey the above magnetic field equations, designing a transport line at reference energy of 500 MeV was investigated by Shinji Machida and Richard Fenning in 2010 [99]. In this work for an FDDF configuration of magnets, with the given parameters in Table 5.1, a transport line for proton beams with 50% energy spread as an alternative to the conventional beam transport lines with solenoids or quadrupoles was designed.

Looking at the results for different momentum orbits shown in Fig. 5.1, it can be seen that using FFAG magnets in a cell or multi-cell section, the large energy spread particle beams like the LPA generated beams can be transported in a distance to bring them to a specific target while the optical functions are identical at the beginning and end of this beam transport section. In other words, using periodical FFAG magnet cells, which are properly matched at both ends of each cell and can be potentially repeated any number of times, serves as a building block for a transport line over an arbitrary distance. In this final chapter of the thesis, I present a preliminary study on optimizing such a scaling linear transport line for electron beams that have much smaller mass and dispersion than protons. This investigation has been done using the CST particle in cell (PIC) solver [82]. To start,

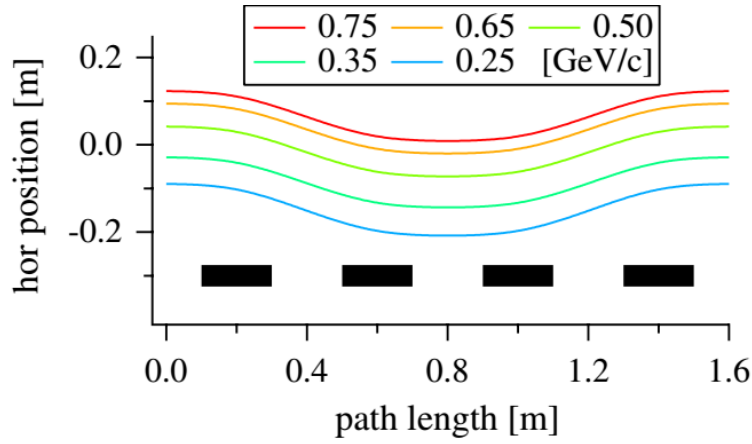


Figure 5.1.: Different momentum orbits in a unit cell, rectangles at the bottom show the position of FDDF magnets, [99].

Table 5.2.: Specifications of 5 electron sources considered for simulation.

No	Energy (MeV)	Hor. position (mm)
1	750	7
2	650	5
3	500	0
4	350	8
5	250	14

I used 5 electron sources with different energies and zero energy dispersion which are spatially dispersed around the reference particle with 500 MeV energy and an initial horizontal position $x = 0$. The particle specifications are compiled in Table 5.2. The electron sources emit electron bunches in Gaussian shape with $1 \mu\text{m}$ bunch length. These electron bunches pass through an FDF magnet structure as shown in Fig. 5.2. These focusing (F_1), defocusing (D), and focusing (F_2) magnets are located in the beam pass in longitudinal positions $z = 300, 700, \text{ and } 1100 \text{ mm}$, respectively. Figure 5.3 and 5.4 show the field shapes of these magnets in horizontal and longitudinal directions which obey the relation in Equation 5.2. For this FDF electron transport section, the magnetic field parameters are summarized in Table 5.3. By tracking the electrons passing through the FDF magnets in a 1 m long path in 5 n sec, different momentum orbits were obtained, Fig. 5.5. As can be seen the electron orbits for different energies have the same shape and the optical functions remained identical at the beginning and end of this beam transport section. This beam transport section can be placed within

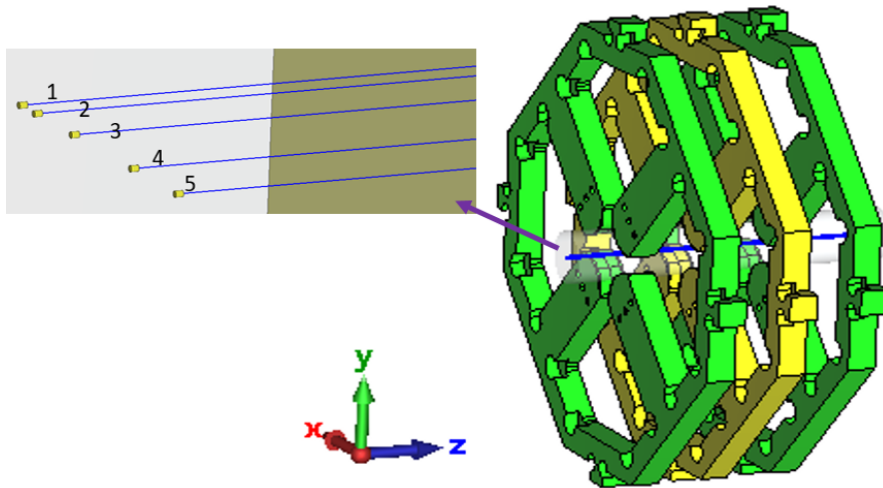


Figure 5.2.: Particle bunches with 5 different energies pass through the FDF magnets simulated in CST.

Table 5.3.: Parameters of an FDF cell.

Parameter	Unit	Value
Reference radius, x_0	m	1E+5
Field index K	-	5E+6
B_{y_0} for F magnets	T	0.32
B_{y_0} for D magnets	T	-0.34
C_1, C_2, C_3, C_4, C_5	-	0.1455, 2.2670, -0.6395, 1.1558, 0, 0
g	m	0.075

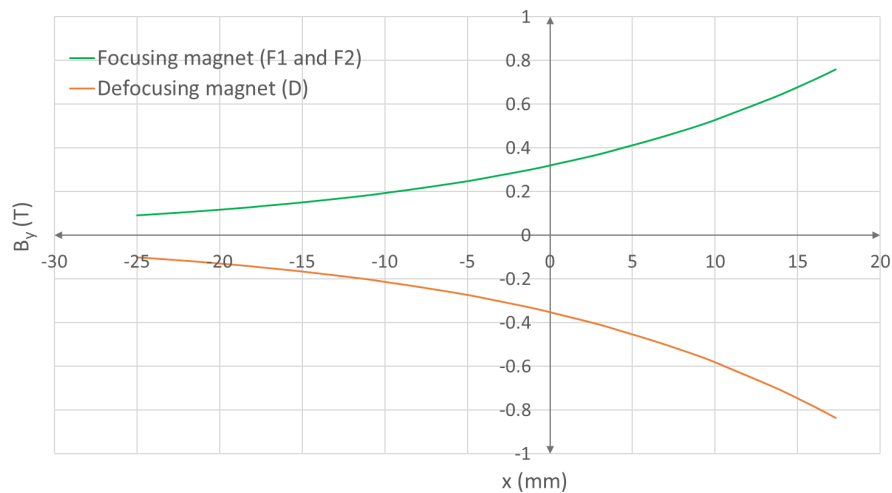


Figure 5.3.: Magnetic field profile B_y of the scaling FFAG magnets in the horizontal direction x .

5. Fixed field alternating gradient transport line

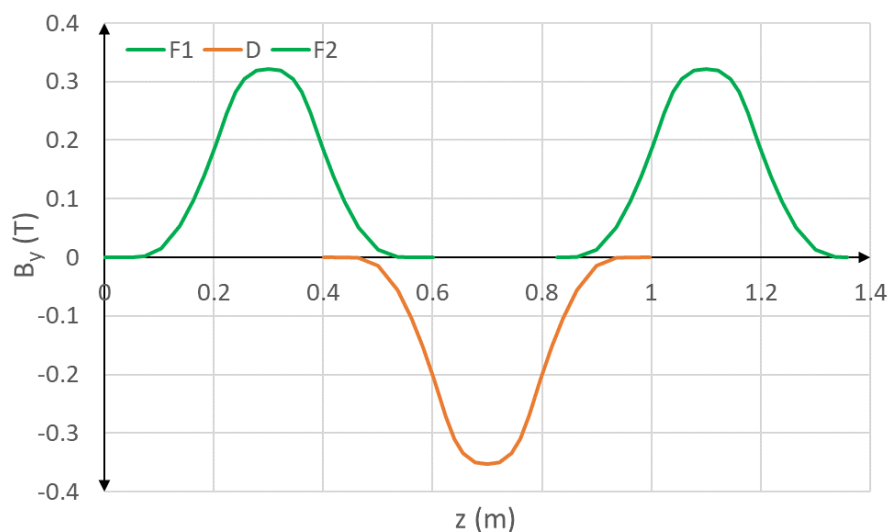


Figure 5.4.: Magnetic field profile B_y of the scaling FFAG magnets in longitudinal direction z .

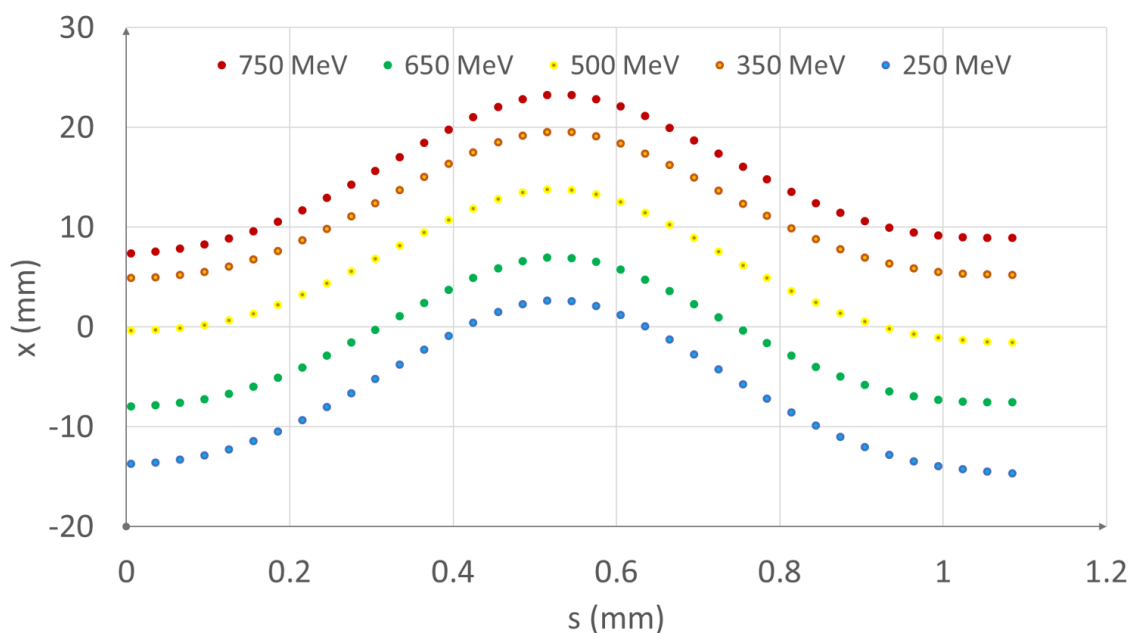


Figure 5.5.: Simulated different momentum orbits for an FFAG transport section.

any transport line that fulfills the defined energies and initial locations of the electron sources summarized in Table 5.2. As a future task on this project, one can cross-check these results with the codes which are written for FFAG-based accelerators, Zgoubi [102] and S-code [103]. Moreover, as a modification to these calculations, an investigation is currently being

carried out at LAS, KIT to explore the possibility of implanting such an FFAG transport section in the designed 700 MeV doublet transport line (see Section 3.1.2.2). In this research, the LPA electron bunches are collimated passing through a doublet section 350 mm after the doublet quadrupoles, the electron beams are affected by the magnetic field of the first combined function dipole and are locally dispersed. These electron beams enter the FFAG section and are transported in a finite length. Then the electron beams continue their path to the third quadrupole and second combined function dipole which in total match the beam optic parameters to the TGU input parameters. This work is planned to be presented at the 14th International Particle Accelerator Conference, IPAC 2023, [104].

Also, an upcoming task could be exploring the possibility of adopting the periodic quadrupole magnet (see Section 4.1) to be used in the FFAG transport cells instead of the periodic FDF/FDDF structures. This can be investigated by changing the pole profile of the periodic quadrupole in a way to create the combined magnetic fields of a scaling FFAG structure and tracking the electron beams going through the magnet using beam dynamics simulation codes.

6. Summary

In this thesis, it was shown that with HTS technology very compact and versatile beam transport lines are feasible. Designs for individual magnets, air-core, and iron-core, as well as for the complete beam transport lines have been developed and adapted to the example case of an LPA-driven TGU light source. Furthermore, the technical feasibility of one of the proposed magnet designs, a novel periodic quadrupole magnet, is proved by the manufacture and test of a demonstrator. In the very first phase of the thesis, several magnet designs for miniaturized HTS iron and coil-dominated magnets were proposed. For the different possible quadrupole geometries, the ones with the ability to generate the higher field gradients were selected *i.e.* a cos-theta air-core geometry and an iron-core periodic geometry which can generate field gradients up to 600 T m^{-1} and 200 T m^{-1} , respectively. These simulations were done at 4.2 K for a maximum current density of 2000 A mm^{-2} .

For the air-core cos-theta magnets two transport lines were designed a triplet-based and a doublet-based with the length of 1.67 m and 1.4 m, respectively. These compact transport lines collimate and guide the LPA electrons at 700 MeV up to 1% energy dispersion (which is in order of what LPAs offer these days), using linear beam optic elements. For the doublet-based design, all the magnets include pure quadrupoles and the combined function dipoles were simulated based on cos-theta geometry. The angular configuration of the sector coils was chosen in a way that leads to small higher-order harmonics and integrated field quality of the order of 10^{-3} . As the cos-theta coils have complicated geometry, it is difficult to wind such coils using ReBCO tapes. So the stress on the coil ends, as a result of the electromagnetic forces, at $T = 4.2 \text{ K}$ was investigated. The results show the Von Mises stress for both dipole and quadrupole coils below the report thresholds. In a try to simplify the HTS cos-theta coils, a novel iron-core quadrupole geometry named periodic quadrupole magnet was designed

and developed. This magnet has 3 periods and a periodic length of $\lambda = 11.9$ cm and has simple-shaped pancake coils. The periodic quadrupole can be well substituted in the doublet section. It collimates the 260 MeV electron beams to the dispersive section, including two combined function dipoles and a pure quadrupole. The whole transport line in a length of 1.4 m fulfills the TGU beam optic requirements at the end of the transport line.

Moreover, all the magnets in the dispersive section were also designed using half a period of the periodic quadrupole and the same quadrupolar cross-section. While an offset in the magnets' center was given for the combined dipoles and the unwanted end fields were shielded using a cryogenic shielding tube at the magnet ends.

To realize the periodic quadrupole magnet, a demonstrator was fabricated. The coils were successfully powered up to the 150 A, which was 120% of the critical current, in liquid nitrogen at $T = 77$ K. To evaluate the coils functioning to generate the magnetic field, the pole tip field using a Hall probe was measured at $T = 77$ K. The measurement results were compared to the Opera 3D simulation which showed very good consistency.

As the last part of the thesis, the possibility of transporting the LPA large energy spread electron beam using Fixed Field Alternating Gradient (FFAG) magnets was investigated and an FFAG FDF transport section for the large dispersed electron beams was designed. This transport section can be used to transport the electrons with different energies, in parallel orbits, to a specific target.

In conclusion, the work done in this thesis provides simulations and optimization of different iron-core and air-core miniature combined function magnets using HTS technology. In this work, a novel high-strength periodic quadrupole magnet was designed and developed which has simple pancake coils and eases the winding difficulties of the HTS coils. A demonstrator of this HTS magnet was fabricated and the coils were successfully powered and tested in liquid nitrogen which shows the feasibility of the magnet concept. It was also shown that by using half a period of this magnet and shielding the end fields, this simple-shaped magnet can work as a non-periodic pure magnet when needed.

Moreover, ultra-compact transport lines based on the designed cos-theta air-core and periodic iron-core magnets were developed. These transport lines can well handle the LPA-generated electrons in less than a 2-meter

length at the energies of 700 MeV and 260 MeV, respectively. Especially, the lab-scaled, 1.4 m length, air-core transport line which is able to collimate and guide the LPA electrons at 700 MeV up to 1% energy dispersion (which is in order of what LPAs offer these days), while using the linear combined beam optic elements.

The next steps for the different parts of this thesis would be as follow:

For the HTS iron-core transport line, testing the HTS periodic quadrupole in $T = 4.2$ K in the near future is planned, also the fabrication of the whole magnets in the iron-core transport line and testing the transport line in a laser-plasma accelerator facility is foreseen.

For the HTS air-core transport line, the possibility of fabrication of the designed cos-theta magnets using the ReBCO-coated conductors can be evaluated by manufacturing a demonstrator. In the case of a successful demonstrator, the whole transport line would be fabricated and tested in a laser-plasma accelerator facility.

Finally, a future step for the designed FFAG transport line would be investigating the possibility of using the HTS periodic quadrupole instead of the periodic FDF/FDDF structures. Also, implanting of the designed FFAG FDF transport section in the 700 MeV air-core transport line is under investigation.

Bibliography

- [1] H. Suk, C. B. Kim, G. H. Kim, J. U. Kim, KERI, I. S. Ko, J. C. Kim, S. J. Hahn, and W. B. Mori. "Overview of The Laser Wakefield Acceleration Research at KERI". In the Proceedings of LINAC2002: Gyeongju, Korea, pp. 591-595, (2002).
- [2] E. Esarey, P. Sprangle, J. Krall and A. Ting, "Overview of plasma-based accelerator concepts," in IEEE Transactions on Plasma Science, vol. 24, no. 2, pp. 252-288, (1996). <https://doi.org/10.1109/27.509991>
- [3] D. Umstadter. "Review of physics and applications of relativistic plasmas driven by ultra-intense lasers". Phys. Plasmas 8 (2001). <https://doi.org/10.1063/1.1364515>
- [4] P. Sprangle, E. Esarey, A. Ting, and G. Joyce. "Laser wakefield acceleration and relativistic optical guiding". Appl. Phys. Let. 53, 2146 (1988). <https://doi.org/10.1063/1.100300>
- [5] D.A Jaroszynski, R Bingham, E Brunetti, B Ersfeld, J Gallacher, B van der Geer, R Issac, S.P Jamison, D Jones, M de Loos, A Lyachev, V Pavlov, A Reitsma, Y Saveliev, G Vieux and S.M Wiggins. "Radiation sources based on laser-plasma interactions". Philosophical Transactions of the Royal Society A: Mathematical, Physical and Engineering Sciences, 364 (1840): 689–710 (2006). <https://doi.org/10.1098/rsta.2005.1732>
- [6] V. Afonso Rodriguez. "Electromagnetic Design, Implementation and Test of a Superconducting Undulator with a Transverse Gradient Field Amplitude". Ph.D. thesis, Karlsruhe Institute of Technology (KIT) (2015). <https://doi.org/10.5445/IR/1000050911>
- [7] C. Widmann. "Simulation and First Experimental Tests of an Electron Beam Transport System for a Laser Wakefield Accelerator". Ph.D.

- thesis, Karlsruhe Institute of Technology (KIT) (2015). <https://doi.org/10.5445/IR/1000055008>
- [8] M. Ning. "A new transport line for transverse gradient undulator experiments at the JETI laser-plasma accelerator in Jena". Master thesis, Karlsruhe Institute of Technology (KIT) (2021).
- [9] H. Wiedemann. "Particle Accelerator Physics". (3rd ed.). Springer, (2007). <http://link.springer.com/10.1007/978-3-540-49045-6>
- [10] C. Biscari. "Transverse beam dynamics". [lecture notes]. The Autonomous University of Barcelona, (2014-15). https://indico.cern.ch/event/528094/contributions/2213316/attachments/1322590/1984069/L3-4-5_-_Transverse_Beam_Dynamics.pdf.
- [11] J. R. Reitz, F. J. Milford, and R. W. Christy. "Foundations of Electromagnetic Theory". 4th Edition, Addison-Wesley, Reading, (1993).
- [12] Industeel Germany GmbH. <https://industeel.arcelormittal.com/fichier/ds-offshore-xc06/>
- [13] C. H. Chang, C. S. Hwang, W.P. Li, M. H. Huang, H. H. Chen, T. C. Fan, F. Y. Lin, Hui-Chia Su. "Conceptual design of magnet systems for the Taiwan photon source". In Proceedings of 2005 Particle Accelerator Conference (PAC05): Knoxville, Tennessee, pp. 3979-3981, (2005).
- [14] S. Fatehi, M. Jafarzadeh, and J. Rahighi. "ILSF Booster Magnets for the Low Emittance Lattice". In Proceedings of the 7th International Particle Accelerator Conference (IPAC2016): Busan, Korea, pp. 1104-1106, (2016).
- [15] S. Fatehi, R. Aslani, and M. R. Khabbazi. "ILSF Storage Ring Magnets". In Proceedings of the 3rd International Particle Accelerator Conference (IPAC2012): New Orleans, Louisiana, USA, pp. 3506-3508, (2012).
- [16] S. Fatehi and H. Ghasem. "ILSF Booster Magnets for the High Field Lattice". In Proceedings of the 5th International Particle Accelerator Conference (IPAC2014): Dresden, pp. 1244-1246, Germany, (2014).

- [17] J. Rahighi, H. Wiedemann, D. Einfeld, A. Wrulich, E. Weihreter, S.Fatehi et al. "ILSF Conceptual Design Report", (2012).
- [18] J. Tanabe. "Iron Dominated Electromagnets: Design, Fabrication, Assembly and Measurements". (1st ed), World Scientific Publishing (2005). <https://www.slac.stanford.edu/pubs/slacreports/reports16/slac-r-754.pdf>
- [19] Th. Zickler. "Basic design and engineering of normal conducting, iron dominated electromagnets". Bruges, Belgium, (2009). <https://cas.web.cern.ch/sites/default/files/lectures/bruges-2009/zickler-2-3.pdf>
- [20] ThyssenKrupp AG. <https://www.thyssenkrupp-steel.com/de/produkte/elektroband/elektroband-nicht-kornorientiert/elektroband-nicht-kornorientiert.html>
- [21] Dassault Systèmes. [Software] Opera (2022). <https://www.3ds.com/de/produkte-und-services/simulia/produkte/opera/>
- [22] Los Alamos National Laboratory.[Software] Poisson Superfish (7.20) (2020). https://laacg.lanl.gov/laacg/services/download_sf.phtml/sfregis.php
- [23] Finite Element Method Magnetics,[Software]. www.FEMM.info
- [24] G. E. Fischer. "Iron Dominated magnets". Stanford Linear Accelerator Center, Stanford University, Stanford, CA 94305, 1985. <https://inspirehep.net/files/251f6ac218f2e6d448fd99b1de3f1795>
- [25] D. Einfeld. "Magnet (warm) lecture". CAS, Frascati, (2008).<https://cas.web.cern.ch/sites/default/files/lectures/frascati-2008/einfeld.pdf>
- [26] S.Fatehi. "2nd ILSF school on Synchrotron radiation and its Applications". Tehran, Iran, (2012).
- [27] Radia [Software]. [www.esrf.fr/machine.groups/insertion_\\$devices/Codes/Radia/Radia](http://www.esrf.fr/machine.groups/insertion_$devices/Codes/Radia/Radia).

- [28] A.N. Dubrovin. "Mermaid code for 3D magnetic field calculations in accelerator design". Computational Accelerator Physics Conf., St. Petersburg, Russia, Jun. 29–Jul. 2, (2004).
- [29] E. Todesco. "Magnetic Design of Superconducting Magnets lecture". CAS, Erice, (2013). <https://cds.cern.ch/record/1974059/files/CERN-2014-005-p269.pdf>
- [30] I. I. Rabi. "A method of producing uniform magnetic fields". Rev. Sci. Instrum. Vol. 5, pp. 78–79, (1934). <https://doi.org/10.1063/1.1751780>
- [31] L. Rossi. "Superconducting Magnets for Particle Accelerators". Reviews of Accelerator Science and Technology, Vol. 5, pp.51–89, (2012). <https://doi.org/10.1142/S1793626812300034>
- [32] L. Bottura. "Field Measurements". In CERN Accelerator School on Superconductivity and Cryogenics for Particle Accelerators and Detectors, Erice, Sicily, (2002). <https://doi.org/10.5170/CERN-2004-008.118>
- [33] R.S. Popovic. "Hall effect devices". second edition. Series in Sensors, CRC Press, (2003).
- [34] S. Sanfilippo. "Hall probes: physics and application to magnetometry". In Proceedings of CERN Accelerator School on Magnets, Bruges, Belgium, pp.423-462, (2009).
- [35] K. H. Mess, P. Schmuser, and S. Wolff. "Superconducting accelerator magnets". World Scientific,(1996).
- [36] P. J. Lee. Applied Superconductivity Center, Florida State University and the National High Magnetic Field Laboratory. <http://fs.magnet.fsu.edu/~lee/plot/plot.htm>
- [37] M. Tanifuji. "Superconducting magnet generates world's highest magnetic field at 24T". National Institute for Materials Science. <https://phys.org/news/2011-09-superconducting-magnet-worlds-highest-magnetic.html>

- [38] S. Hahn, K. Kim, X. Hu, T. Painter, I. Dixon, S. Kim. "45.5-tesla direct-current magnetic field generated with a high-temperature superconducting magnet". *Nature* 570, pp. 496–499 (2019). <https://doi.org/10.1038/s41586-019-1293-1>
- [39] SuperPower Inc. <http://www.superpower-inc.com/>
- [40] L. Liu, Y. Li, X. Wu, G. Xiao and D. Xu. "Development of Long RE-BCO Coated Conductors by PLD-REBCO/Sputter-CeO₂/IBAD-MgO at SJTU and SSTC". In *IEEE Transactions on Applied Superconductivity*, vol. 25, no. 3, pp. 1-4,(2015). <https://doi.org/10.1109/TASC.2014.2385866>
- [41] R. Pratap, G. Majkic, E. Galstyan, G. Mohanasundaram, S. Chakradhar and V. Selvamanickam, "Growth of High-Performance Thick Film REBCO Tapes Using Advanced MOCVD". In *IEEE Transactions on Applied Superconductivity*, vol. 29, no. 5, pp. 1-5, (2019). <https://doi.org/10.1109/TASC.2019.2899244>
- [42] X. Xiong, S. Kim, K. Zdun, S. Sambandam, A. Rar et al., "Progress in High Throughput Processing of Long-Length, High Quality, and Low Cost IBAD MgO Buffer Tapes at SuperPower", *IEEE Transactions on Applied Superconductivity* Vol. 19 No. 3. (2009). <https://doi.org/10.1109/TASC.2009.2018816>
- [43] W. Prusseit, C. Hoffmann, R. Nemetschek, G. Sigl, J. Handke, et al. "Long length coated conductor fabrication by inclined substrate deposition and evaporation". *Journal of Physics: Conference Series* Vol. 43 No. 1 (2006). <https://doi.org/10.1088/1742-6596/43/1/054>
- [44] H. Kutami, T. Hayashida, S. Hanyu, C. Tashita, M. Igarashi, et al. "Progress in research and development on long length coated conductors in Fujikura". *Physica C: Superconductivity and its Applications* Vol. 469 No. 15 (2009). <https://doi.org/10.1016/j.physc.2009.05.135>
- [45] J. X. Jin, Y. Xin, Q. L. Wang, Y. S. He, C. B. Cai et al. "Enabling High-Temperature Superconducting Technologies Toward Practical applications". *IEEE Transactions on Applied Superconductivity* Vol. 24 No. 5 (2014). <https://doi.org/10.1109/TASC.2014.2346496>

- [46] S. Lee, V. Petrykin, A. Molodyk, S. Samoilenkov, A. Kaul et al. "Development and production of second generation high T_c superconducting tapes at SuperOx and first tests of model cables". *Superconductor Science and Technology* Vol. 27 No. 4 (2014). <https://doi.org/10.1088/0953-2048/27/4/044022>
- [47] S. C. Richter, D. Schoerling, S. I. Schlachter, B. Ringsdorf, A. Drechsler, A. Bernhard, A. -S. Müller. "Bending radius limits of different coated ReBCO conductor tapes – An experimental investigation with regard to HTS undulator". In *Proceedings of the 12th International Particle Accelerator Conference (IPAC21): Campinas, Brazil*, pp. 3837-3840, (2021). <https://doi.org/10.18429/JACoW-IPAC2021-THPAB042>
- [48] Der Roebelstab von Ludwig Roebel (1878-1934): <https://www.mannheim.de/de/wirtschaft-entwickeln/roebelstab-ludwig-roebel-1878-1934>
- [49] D. S. Beard, W. Klose, S. Shimamoto, G. Vescey. "The IEA Large Coil Task development of superconducting toroidal field magnets for fusion power". *Fusion Engineering and Design* 7, pp 1-230, (1988).
- [50] A.P. Verweij, L. Buchsbaum. "Experimental results of current distribution in Rutherford-type LHC cables". *Cryogenics*, Volume 40, Issues 8–10, pp. 663-670, (2000). [https://doi.org/10.1016/S0011-2275\(01\)00023-6](https://doi.org/10.1016/S0011-2275(01)00023-6)
- [51] V. Hussennether, M. Oomen, M. Leghissa, H.-W. Neumüller. "DC and AC properties of Bi-2223 cabled conductors designed for high-current applications". *Physica C: Superconductivity*, Volume 401, pp 135-139, (2004). <https://doi.org/10.1016/j.physc.2003.09.024>
- [52] M. Leghissa. "Method for producing a fully transposed high T_c composite superconductor and a superconductor produced by said method". Patent DE10223542 (B4), Siemens AG, the registration year 2002.
- [53] W. Goldacker. "Roebel Cable from Coated Conductors". CEC/ICMC Conf. Late breaking news talk, Keystone, CO, USA, (2005).
- [54] W. Goldacker, R. Nast, G. Kotzyba, S. I. Schlachter, A. Frank, B. Ringsdorf, C. Schmidt and P. Komarek. "High current DyBCO-ROEBEL

- Assembled Coated Conductor". J Phys. Conf. Ser. 43, pp 901-904. (2006). <https://doi.org/10.1088/1742-6596/43/1/220>
- [55] S. J. Otten. Characterization of REBCO Roebel cables. Karlsruhe: KIT Scientific Publishing. (2019). <https://doi.org/10.5445/KSP/1000091629>
- [56] G. Kirby, J. Nugteren, A. Ballarino, L. Bottura, N. Chouika, et al. "Accelerator-Quality HTS Dipole Magnet Demonstrator Designs for the EuCARD-2 5-T 40-mm Clear Aperture Magnet". IEEE Transactions on Applied Superconductivity Vol. 25 No. 3. (2015). <https://doi.org/10.1109/TASC.2014.2361933>
- [57] C. Lorin, M. Segreti, A. Ballarino, L. Bottura, M. Durante, et al. "Cos-theta Design of Dipole Inserts Made of REBCO-Roebel or BSCCO-Rutherford Cables". IEEE Transactions on Applied Superconductivity Vol. 25 No. 3 (2015). <https://doi.org/10.1109/TASC.2014.2360422>
- [58] T. Tajima and J. M. Dawson. "Laser electron accelerator". Phys. Rev. Lett.,43, pp. 267–270,(1979). <https://link.aps.org/doi/10.1103/PhysRevLett.43.267>
- [59] P. Chen, J. M. Dawson, Robert W. Huff, and T. Katsouleas. "Acceleration of Electrons by the Interaction of a Bunched Electron Beam with a Plasma". Phys. Rev. Lett. 54, pp. 693-696 (1985). <https://link.aps.org/doi/10.1103/PhysRevLett.54.693>
- [60] C. G. R. Geddes, C. Toth, J. van Tilborg, E. Esarey, C. B. Schroeder, D. Bruhwiler, C. Nieter, J. Cary and W. P. Leemans." High-quality electron beams from a laser wakefield accelerator using plasma-channel guiding". Nature, Vol 431, 30, (2004). <https://doi.org/10.1038/nature02939>
- [61] W. P. Leemans, B. Nagler, A. J. Gonsalves, CS. Toth, K. Nakamura, C. G. R. Geddes, E. Esarey, C. B. Schroeder and S. M. Hooker." GeV electron beams from a centimeter-scale accelerator". Nature Phys 2, pp. 696–699 (2006). <https://doi.org/10.1038/nphys418>
- [62] H. Kim, K. H. Pae, H. J. Cha, I. J. Kim, T. J. Yu, J. H. Sung, S. K. Lee, T. M. Jeong, and J. Lee."Enhancement of Electron Energy to

- the Multi-GeV Regime by a Dual-Stage Laser-Wakefield Accelerator Pumped by Petawatt Laser Pulses". *Phys. Rev. Lett.* 111, 165002, (2013). <https://doi.org/10.1103/PhysRevLett.111.165002>
- [63] W. P. Leemans, A. J. Gonsalves, H. -S. Mao, K. Nakamura, C. Benedetti, C. B. Schroeder, Cs. Tóth, J. Daniels, D. E. Mittelberger, S. S. Bulanov, J. -L. Vay, C. G. R. Geddes, and E. Esarey." Multi-GeV Electron Beams from Capillary-Discharge-Guided Subpetawatt Laser Pulses in the Self-Trapping Regime". *PRL* 113, 245002, (2014). <https://doi.org/10.1103/PhysRevLett.113.245002>
- [64] E. Esarey, C. B. Schroeder and W. P. Leemans. "Physics of laser-driven plasma-based electron accelerators". In: *Rev. Mod. Phys.* 81, pp. 1229–1285, (2009). <https://link.aps.org/doi/10.1103/RevModPhys.81.1229>
- [65] F. Albert, M. E. Couprie, A. Debus, M. C. Downer, J. Faure, A. Flacco, L. A Gizzi, T. Grismayer, A. Huebl, C. Joshi. "2020 roadmap on plasma accelerators". *New J. Phys.* 23 031101, (2021). <https://doi.org/10.1088/1367-2630/abcc62>
- [66] Wang, W., Feng, K., Ke, L. et al. "Free-electron lasing at 27 nanometres based on a laser wakefield accelerator". *Nature* 595, 516–520 (2021). <https://doi.org/10.1038/s41586-021-03678-x>
- [67] D. O. Espinos, A. Ghaith, A. Loulergue, T. André, C. Kitégi, et al. "COXINEL transport of laser plasma accelerated electrons". *Plasma Phys.Control.Fusion*, 62 (3), pp.034001, (2020). <https://doi.org/10.1088/1361-6587/ab5fec>
- [68] A. Streun. OPA (3.91d) [Software], (2021). <https://ados.web.psi.ch/opa/>
- [69] M. Borland. elegant (2021.4) [Software], (2021). <https://ops.aps.anl.gov/elegant.html>
- [70] K. Floettmann.[Software] Astra: A space charge tracking algorithm. Manual, 3, (2021). <https://www.desy.de/~mpyflo/>
- [71] M. Schnell, A. Sävert, B. Landgraf, M. Reuter, M. Nicolai, , O. Jäckel, C. Peth, T. Thiele, O. Jansen, A. Pukhov, O. Willi, M. C. Kaluza, and

- C. Spielmann. "Deducing the Electron-Beam Diameter in a Laser-Plasma Accelerator Using X-Ray Betatron Radiation". *Phys. Rev. Lett.*, 108, pp. 075001- 075005, (2012). <https://link.aps.org/doi/10.1103/PhysRevLett.108.075001>
- [72] S. Fritzler, E. Lefebvre, V. Malka, F. Burgy, A. E. Dangor, K. Krushelnick, S. P. D.Mangles, Z. Najmudin, J.-P. Rousseau, and B. Walton. "Emittance measurements of a laser-wakefield-accelerated electron beam". *Phys. Rev. Lett.*, 92:165006, (2004). <https://doi.org/10.1103/PhysRevLett.92.165006>
- [73] E. Brunetti, R. P. Shanks, G. G. Manahan, M. R. Islam, B. Ersfeld, M. P. Anania, S. Cipiccia, R. C. Issac, G. Raj, G. Vieux, G. H. Welsh, S. M. Wiggins, and D. A. Jaroszynski. "Low emittance, high brilliance relativistic electron beams from a laser-plasma accelerator". *Phys. Rev. Lett.*, 105:215007, Nov 2010. <https://link.aps.org/doi/10.1103/PhysRevLett.105.215007>
- [74] R. Weingartner, S. Raith, A. Popp, S. Chou, J. Wenz, K. Khrennikov, M. Heigoldt, A. R. Maier, N. Kajumba, M. Fuchs, B. Zeitler, F. Krausz, S. Karsch, and F. Grüner. "Ultralow emittance electron beams from a laser-wakefield accelerator". *Phys. Rev. ST Accel. Beams*, 15:111302, (2012). <https://link.aps.org/doi/10.1103/PhysRevSTAB.15.111302>
- [75] K. Damminsek. "Magnetic Characterization Studies of a Superconducting Transverse Gradient Undulator for a Compact LPA-based Free-Electron Laser". Ph.D. thesis, Karlsruhe Institute of Technology (KIT), (2022). <https://doi.org/10.5445/IR/1000153441>
- [76] M. Ning, S. Fatehi, A. Bernhard, R. Rossmanith and A. -S. Müller. "A new beam transport line for transverse gradient undulator at JETI in Jena". DPG-Frühjahrstagungen, (2022), Mainz, Germany.
- [77] C. Barth, G. Mondonico and C. Senatore. "Electro-mechanical properties of REBCO coated conductors from various industrial manufacturers at 77 K, self-field and 4.2 K, 19 T". *Superconductor Science and Technology* 28, (2015).

- [78] S. Fatehi, A. Bernhard and A. -S. Müller. "Miniature, High Strength Transport Line Design for Laser Plasma Accelerator-Driven FELs". In Proceedings of the 12th International Particle Accelerator Conference (IPAC21): Campinas, Brazil, pp. 561-563, (2021).
- [79] S. Fatehi, A. Bernhard and A. -S. Müller. "Miniature Transport-line Design for Laser Plasma accelerator-driven FELs using HTS Magnets". DPG-Frühjahrstagungen (2022), Mainz, Germany.
- [80] A. Bernhard, N. Braun, V. Afonso Rodríguez, P. Peiffer, Robert Rossmanith, C. Widmann and M. Scheer. "Radiation emitted by transverse-gradient undulators". Phys. Rev. Accel. Beams 19, 090704, (2016). <https://link.aps.org/doi/10.1103/PhysRevAccelBeams.19.090704>
- [81] A. Bernhard, E. Burkard, V. Afonso Rodríguez, C. Widmann, A.-S. Müller. "Transverse Gradient Undulator-based high-gain-FEL — a parameter study". In Proceedings of the 6th International Particle Accelerator Conference (IPAC2015): Richmond, VA, USA, pp. 1502-1505, (2015).
- [82] Dassault Systèmes. CST studio suite (2021) [Software]. Dassault Systèmes. <https://www.3ds.com/de/produkte-und-services/simulia/produkte/cst-studio-suite>
- [83] Anna Kario, Twente University, internal discussions.
- [84] Thibault Lecrevisse, CEA, internal discussions.
- [85] Dieter Einfeld, ILSF, internal discussions.
- [86] V. Kashikhin. "A Novel Design of Iron Dominated Superconducting Multipole Magnets With Circular Coils". IEEE Transactions on Applied Superconductivity, VOL. 20, NO. 3, (2010). <https://doi.org/10.1109/TASC.2009.2039706>
- [87] C. Benabderrahmane, J.C. Biasci, J.F. Bouteille, J. Chavanne, L. Farvacque, L. Goirand, G. Lebec, S.M. Luizzo, P. Raimondi, F. Villar. "Magnets for the ESRF-EBS project". In Proceedings of the 7th International Particle Accelerator Conference (IPAC2016): Busan, Korea, pp. 1096-1099, (2016).

- [88] A. Shahveh. "Magnet Design for Diamond-II Upgrade". ALERT Workshop, Ioannina, Greece. (2019).
- [89] Magneticshields. Inc. <https://magneticshields.co.uk/technical/material-technical-data>
- [90] T. Arndt, B. Holzapfel, M. Noe, R. Nast, F. Hornung, M. Kläser and A. Kudymow. "New coil configurations with 2G-HTS and benefits for applications". *Supercond. Sci. Technol.* 34 095006, (2021). <http://doi.org/10.1088/1361-6668/ac19f4>
- [91] M. Yazdani-Asrami, S. M. Seyyedbarzegar, M. Zhang, W. Yuan. "Insulation materials and systems for superconducting powertrain devices in future cryo-electrified aircraft: part I-material challenges and specifications, and device-level application". *IEEE Electrical Insulation Magazine*, 38(2), pp. 23-36, (2022). <https://doi.org/10.1109/MEI.2022.9716211>
- [92] G. Kirby, CERN, internal discussions.
- [93] HTS critical current database. <https://htsdb.wimbush.eu/dataset/4256624>
- [94] H. S. Kim, J. B. Song, N. Y. Kwon, K. L. Kim, H. G. Lee. "The influence of heat-treatment and oxygenation annealing on the superconducting properties of YBCO coated conductors". (2009). <http://doi.org/10.1088/0953-2048/22/12/125016>
- [95] AREPOC s.r.o., "Cryogenic Hall probe", <http://www.arepoc.sk/>, (2017).
- [96] K. Peach et al. "Pamela design report". Technical report, CONFORM, (2011).
- [97] D. Trbojevic, E. Courant, and A. Garren. "FFAG lattice without opposite bends". In *AIP Conf. Proc.*, (2000).
- [98] R. Edgecock et al. "Emma the world's first non-scaling FFAG". In *Proceedings of EPAC*, pp. 3380-3382, (2008).

- [99] S. Machida, R. Fenning. "Beam transport line with scaling fixed field alternating gradient type magnets". *Phys. Rev. ST Accel. Beams* 13, (2010). <http://dx.doi.org/10.1103/PhysRevSTAB.13.084001>
- [100] J.-B. Lagrange, T. Planche, et al. "Straight scaling FFAG beam line". *Nuclear Instruments and Methods in Physics Research Section A: Accelerators, Spectrometers, Detectors and Associated Equipment*, Volume 691, (2012), pp. 55-63, ISSN 0168-9002, <https://doi.org/10.1016/j.nima.2012.06.058>
- [101] R. Fenning. "Novel FFAG Gantry and Transport Line Designs for Charged Particle Therapy". Ph.D. thesis, Brunel University (2011).
- [102] F. Meot and S. Valero. *Zgoubi User's Guide*, 4.3 edition [Software], March 2008.
- [103] S. Machida, *ICFA Beam Dynamics Newsletter*, edited by C. R. Prior (2007), Vol. 43, p. 54 <http://icfa-usa.jlab.org/archive/newsletter.shtml/>.
- [104] M. Ning, S. Fatehi, A. Bernhard, A-S. Müller, "Scaling fixed-field alternating gradient-type magnets for transportation of laser-plasma accelerator electron beams". To be published in *Proceedings of the 14th International Particle Accelerator Conference (IPAC2023): Venice, Italy*, (2023).

List of Figures

2.1.	Curvilinear coordinate system of beam dynamics.	7
2.2.	Particle trajectories, reference path s and individual particle trajectory s_i with different bending radii.	7
2.3.	Phase-space ellipse in the two-dimensional transverse phase space $x - x'$	11
2.4.	XC-06 magnetic steel magnetization curve using the data from [12], the author permission is granted.	13
2.5.	Dipole magnet cross-section (left) and magnetic field distribution in the horizontal direction (right).	17
2.6.	Standard shapes of dipole magnet; H shape (left), C-shape (center) and O-shape (right). The green color represents the iron yoke, and the blue/red color is used to show the current carrying coils.	17
2.7.	Integration path in a dipole magnet.	18
2.8.	Quadrupole magnet cross-section (left) and magnetic field distribution in the horizontal direction (right).	19
2.9.	Standard (left), Collin (center), and Panofsky (right) quadrupoles. The green color represents the iron yoke, and the blue/red color is used to show the current carrying coils.	20
2.10.	Integration path in a quadrupole magnet.	20
2.11.	Sextupole magnet cross-section (left) and magnetic field distribution in the horizontal direction (right).	21
2.12.	Integration path in a sextupole magnet.	22
2.13.	Designed pole profiles for; combined function dipole with the dipole field of $B = 1.42$ T and two different quadrupole components (top) [15] and combined function quadrupole with sextupole component (bottom) [16], both these designs were done by S. Fatehi for the ILSF magnets.	23

2.14. Sextupoles magnet with superimposed dipolar and quadrupolar fields.	24
2.15. Field lines inside a combined function sextupole, when the sextupole coils are off and horizontal correction (left), vertical correction (center), and skew quadrupole coils are on. In Steering coils, green and orange represent, the positive and negative current flux in each coil respectively, this design is developed by S. Fatehi and published in ILSF conceptual design report [17].	24
2.16. Schematic view of magnetic length.	25
2.17. Schematic view of the magnet design procedure.	26
2.18. Schematic of the shimming process according to the explanations in [24].	28
2.19. Pole profile and shim shapes designed by FEMM for combined function dipole (left), quadrupole (center) and sextupole (right) magnets [26], designs were done by S. Fatehi.	28
2.20. Chamfers on H-type dipole magnet (left) and quadrupole magnets (right).	29
2.21. Magnetic field generated in z by an infinitely thin current line placed at z_0 , geometric plane represented by complex plane.	30
2.22. Two overlapping cylinders with current density J , the center points C_1 and C_2 separated in x direction by a distance t	31
2.23. Sector coil dipole (left), and quadrupole (right).	33
2.24. Layout of dipolar coils, one-layer with one wedge (right) and two-layer with no wedges (left).	35
2.25. Sketch of a Hall generator, consists of a thin semiconductor plate of length l , width w , and thickness t	39
2.26. Meissner effect: the expulsion of the magnetic flux inside a superconductor due to the induced surface current at $T < T_c$ and non-changing external field.	41
2.27. Superconductors Type I (left) and Type II (right).	43

2.28. Superconductors type II critical surface given by critical magnetic field B_c , critical temperature T_c , and the critical current I_c forms the limit between the superconducting and normal phases.	43
2.29. Comparison of the critical surfaces of Nb-Ti and Nb ₃ Sn, both LTS conductors and ReBCO, HTS conductor [29].	44
2.30. Current carrying capacity of some practical superconductors vs. magnetic field published by P. Lee [36], the author's permission is granted.	45
2.31. A schematic of the critical current (I_c) dependency to the relative direction of the magnetic field B with respect to the tape face in an HTS tape; field direction has an angle α with the tape face normal (top), perpendicular field (B_{\perp}) to the tape face (bottom-left), and parallel field (B_{\parallel}) with the tape (bottom-right).	46
2.32. Multi-layer structure of a ReBCO coated- superconducting tape developed by Superpower Inc. [39].	47
2.33. Roebel cable geometrical parameters of the punched meandering pattern.	49
2.34. Schematic sketch of an LPA acceleration process.	50
3.1. Transverse Gradient Undulator (TGU) [6].	55
3.2. Magnet layout and beam optic parameters along beam trajectory at 300 MeV for the normal conducting transport line, [8].	56
3.3. Magnet layout and beam optic parameters along beam trajectory at 700 MeV for the triplet-based HTS transport line design.	59
3.4. Magnet layout and beam optic parameters along beam trajectory at 700 MeV for the doublet-based HTS transport.	61
3.5. Momentum deviation $\Delta P/P$ versus transverse positions x in mm (left) and divergence x' in mrad (right).	61
3.6. β functions, in x (left) and y (right) planes for different energies up to $\pm 1\%$	62
3.7. Phase-space distribution for different energies for $\pm 1\%$ energy spread.	63

3.8.	β functions, in x (left) and y (right) planes for different energies up to $\pm 5\%$	63
3.9.	Schematic of the HTS air-core transport line.	64
3.10.	Geometry layout and coil configuration of the quadrupole magnets.	65
3.11.	2D (left) and 3D (right) models of the quadrupole magnet including the beam tube with $r = 5$ mm.	66
3.12.	Air-core HTS quadrupoles with (right) and without (left) coil-end design.	67
3.13.	Magnetic field versus longitudinal direction for the coils; with (blue) and without (orange) saddle coil end design. . .	68
3.14.	Quadrupole magnet modeled in Opera software.	68
3.15.	Vertical magnetic field B_y versus horizontal direction at $y, z = 0$	69
3.16.	Field gradient versus longitudinal direction on the beam path i.e. $x, y = 0$	69
3.17.	Field gradient quality versus horizontal direction for $y, z = 0$	70
3.18.	Integrated field gradient quality versus horizontal direction for $y = 0$	70
3.19.	Effective length variation in the horizontal good field region.	71
3.20.	Coil configuration of the combined function dipole magnets, blue coils indicates the dipolar coils red coils create the quadrupole field.	73
3.21.	3D models of the combined dipole magnet including the beam tube with $r = 7$ mm.	74
3.22.	Combined dipole magnet with end coil design, dipole coils (right-top), and quadrupole coils (right-bottom).	74
3.23.	Vertical magnetic field B_y versus horizontal direction at $y, z = 0$	75
3.24.	Field gradient versus horizontal direction at $y, z = 0$	75
3.25.	Field quality versus horizontal direction at $y, z = 0$	76
3.26.	Field gradient quality versus horizontal direction at $y, z = 0$	76
3.27.	Integrated field gradient quality versus horizontal direction at $y = 0$	77
3.28.	One-fourth of the simulated quadrupole coils with mesh lines.	79
3.29.	One-half of the simulated dipole coils with mesh lines.	79

3.30. Von Mises stress on one-fourth of the quadrupole HTS coil at 4.2 K.	80
3.31. Von Mises stress on one-half of the dipole HTS coil at 4.2 K.	80
4.1. Iron-core quadrupole designs: shell coil geometry (left) and periodic geometry (right).	83
4.2. Shell coil geometry yoke design (left) and coils with current direction (right).	84
4.3. Vertical magnetic field B_y versus horizontal direction at $y, z = 0$ (left) and longitudinal magnetic field B_z versus longitudinal direction at $x, y = 0$ (right).	84
4.4. Periodic quadrupole; pancake coil dimensions (right) and whole geometry with periodic length λ (left), green and red represent iron yoke and current carrying coils respectively.	85
4.5. Shape of the designed pole profile for the periodic quadrupole, the green part on the top right shows the pole profile and the pole root of the magnet modeled in Opera.	86
4.6. Magnetic field B_y versus horizontal direction x at $y, z = 0$	87
4.7. Magnetic field quality versus horizontal direction x at $y, z = 0$	87
4.8. Magnetic field gradient g along the longitudinal direction z for a 1.5-period model at $y = 0$	88
4.9. Beta functions β_x and β_y along beam trajectory S , for 1.5-period model with $\lambda = 5.9$ cm at the energy of 260 MeV.	89
4.10. Field gradient g versus longitudinal direction z for 1.5-periods model and different periodic length.	90
4.11. Beta functions β_x and β_y along beam trajectory s , for 1.5-period model with $\lambda = 11.9$ cm at the energy of 260 MeV.	91
4.12. Beta functions β_x and β_y along beam trajectory s , for 1.5-period model with $\lambda = 13.9$ cm at the energy of 260 MeV.	91
4.13. Field gradient g versus longitudinal direction z for $\lambda = 11.9$ and 13.9 cm and different period numbers.	92
4.14. Beta functions β_x and β_y along beam trajectory for models with $\lambda = 11.9$ and 13.9 cm and 2 and 3 periods.	92
4.15. One-fourth of the periodic quadrupole magnet with $\lambda = 11.9$ cm and 3 periods.	93

4.16. Beam parameters versus beam trajectory from LPA to the end of the periodic quadrupole.	94
4.17. Magnet layout and beam optic parameters along beam trajectory at 260 MeV.	95
4.18. Pole profiles of the combined dipole magnet, the blue rhombus sign shows the offset magnetic center.	97
4.19. Combined dipole magnet; half a period of the periodic quadrupole with offset magnetic center, X-Y-Z and U-V-W are beam and magnet coordinate systems respectively.	98
4.20. Combined dipole field B_y versus; horizontal direction x at $y, z = 0$ (top) and longitudinal directions z at $x, y = 0$ (bottom).	99
4.21. Combined dipole magnet model with magnetic shielding tubes around the beam chamber, colored in violet.	99
4.22. Magnetic field profile in the longitudinal direction at $x, y = 0$, with and without magnetic shielding.	100
4.23. Schematics of the HTS iron-core transport line.	101
4.24. Design A with two 12mm width pancake coils.	102
4.25. Design B with coils consisting of 1 mm thick ReBCo coated disks.	102
4.26. Half a period model designed with Opera 3D, general view (left) and detailed view (right).	103
4.27. Mechanical model; magnet cross-section (left), and coil winding (right), courtesy of Matthias Eisele, ITEP, KIT.	104
4.28. Winding body demonstrator.	104
4.29. Critical current I_c versus magnetic field B for 12 mm wide tape at $T = 77$ K, [93].	105
4.30. Magnetic flux density on HTS bridge and coils at 77 K (left) and 4.2 K (right).	106
4.31. Lorentz forces on coils and HTS bridge at 4.2 K.	106
4.32. Soldering the first turn of ReBCO tape on the copper body.	108
4.33. Placing the soldered face of the tape on the soldered copper body.	108
4.34. Last turn soldering.	109
4.35. Wound pancake coils.	109
4.36. Copper bridge (left) and HTS tapes on the copper bridge (right).	109

4.37. Soldered end turns (left) and soldered HTS bridge tapes on Soldered end turns (right).	110
4.38. Magnet demonstrator.	110
4.39. Current leads (black arms) and voltage measurement wiring.	111
4.40. Voltage measurement channels.	111
4.41. Powering setup.	112
4.42. Hanging the demonstrator in a box filled with LN ₂	112
4.43. Measured voltage and current over coil I and coil II, versus time.	114
4.44. Measured voltage over coil I and coil II versus current, values are corrected to the normal conducting parts' resistances.	114
4.45. Field measurement setup.	115
4.46. Field measurement setup with the current leads and voltage measuring wires in liquid nitrogen.	116
4.47. Load current vs. time for Hall probe measurement.	116
4.48. Magnetic field on pole tip $B_{Poletip}$ vs. applied current, obtained by Hall-probe measurement and Opera simulation.	117
5.1. Different momentum orbits in a unit cell, rectangles at the bottom show the position of FDDF magnets, [99].	122
5.2. Particle bunches with 5 different energies pass through the FDF magnets simulated in CST.	123
5.3. Magnetic field profile B_y of the scaling FFAG magnets in the horizontal direction x	123
5.4. Magnetic field profile B_y of the scaling FFAG magnets in longitudinal direction z	124
5.5. Simulated different momentum orbits for an FFAG transport section.	124

List of Tables

2.1.	Upright multipole fields.	16
2.2.	Pole profile equation for the common combined-function magnets.	23
2.3.	Different angular layouts for air-core dipole, canceling the first allowed harmonics.	36
2.4.	Different angular layouts for air-core quadrupole, canceling the first allowed harmonics.	38
2.5.	Critical temperatures for Various Superconductors.	40
2.6.	Tested samples at 77 K and their parameters, measured critical current I_c , and measured minimum bending radius R_{min} . The minimum bending radius is defined as the smallest radius for which the critical current degrades less than 5%, [47].	48
3.1.	Start parameters for the beam transport line design.	54
3.2.	Magnet specifications for the triplet-based transport line at 700 MeV.	58
3.3.	Magnet specifications for the doublet-based transport line at 700 MeV.	60
3.4.	Quadrupole magnets specification at 700 MeV.	65
3.5.	Quadrupole Coil properties for the air-core transport line.	66
3.6.	Quadrupole field coefficients in central plane at $x = 5$ mm.	72
3.7.	Dipole magnets specification at 700 MeV.	72
3.8.	Combined dipoles coil parameters.	73
3.9.	Combined dipole D1 field coefficients in the central plane at 5 mm.	78
4.1.	Pole profile coordinates of the periodic quadrupole.	86
4.2.	Coil specifications for the periodic quadrupole magnet.	90

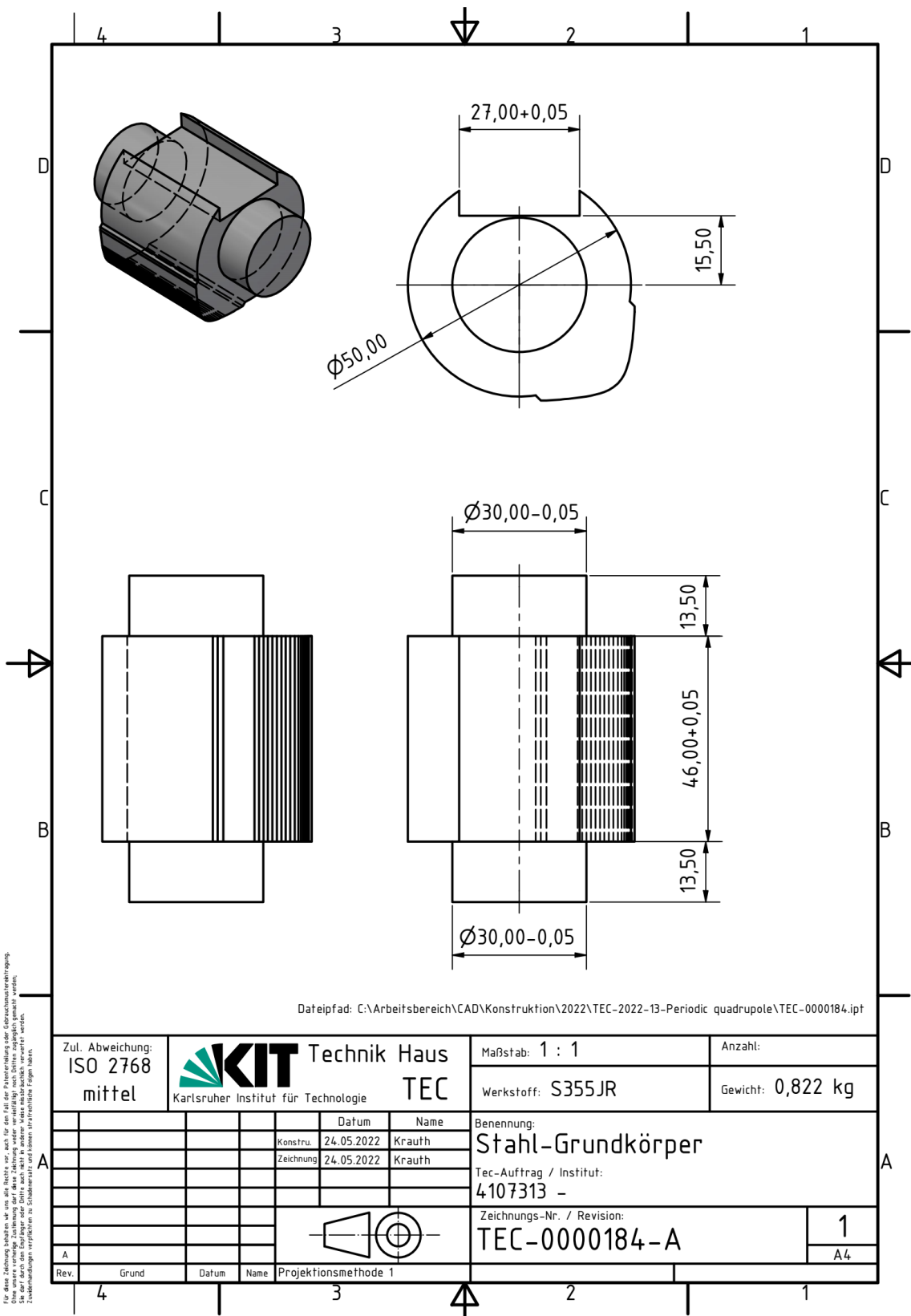
4.3.	Magnet parameters for the periodic quadrupole with $\lambda = 11.9$ cm and 3 periods at 4.2 K.	93
4.4.	Beam optics parameters at the end of the periodic quadrupole at $S = 0.54$ m shown by a dotted green line in Fig. 4.16. . . .	94
4.5.	Magnet specifications for the designed dispersive section at 260 MeV.	95
4.6.	Beam optics parameters at the end of the transport line, center of the TGU.	96
4.7.	Magnet specifications at 260 MeV.	96
4.8.	Field coefficients of the combined dipole D1, at 5 mm.	100
4.9.	Electrical parameters for the demonstrator coils.	105
4.10.	Hall probe specifications used for magnetic measurement.	115
5.1.	Parameters of an FDDF cell, [99].	121
5.2.	Specifications of 5 electron sources considered for simulation.	122
5.3.	Parameters of an FDF cell.	123

List of Abbreviations


Abbreviation	Description
FEL	Free Electron Laser
LPA	Laser Plasma Accelerator
LWFA	Laser Wakefield Accelerator
PWFA	Particle Wakefield Accelerator
RF	Radio Frequency
TGU	Transverse Gradient Undulator
KIT	Karlsruhe Institute of Technology
LAS	Laboratory for Applications of Synchrotron Radiation
ITEP	Institute of Technical Physics
HTS	High Temperature Superconductor
LTS	Low Temperature Superconductor
ReBCO	Rare earth Barium Copper Oxide
BSCCO	Bismuth Strontium Calcium Copper Oxide
EuCARD-2	European Coordination for Accelerator Research
ILSF	Iranian Light Source Facility
TPS	Taiwan Photon Source
ESRF	European Synchrotron Radiation Facility
ESRF-EBS	ESRF-Extremely Brilliant Source
FFAG	Fixed Field Alternating Gradient
FDF	Focusing-Defocusing-Focusing

A. Appendix

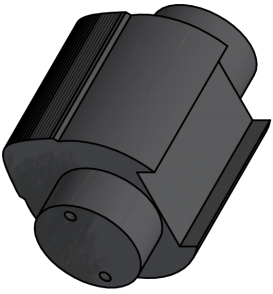
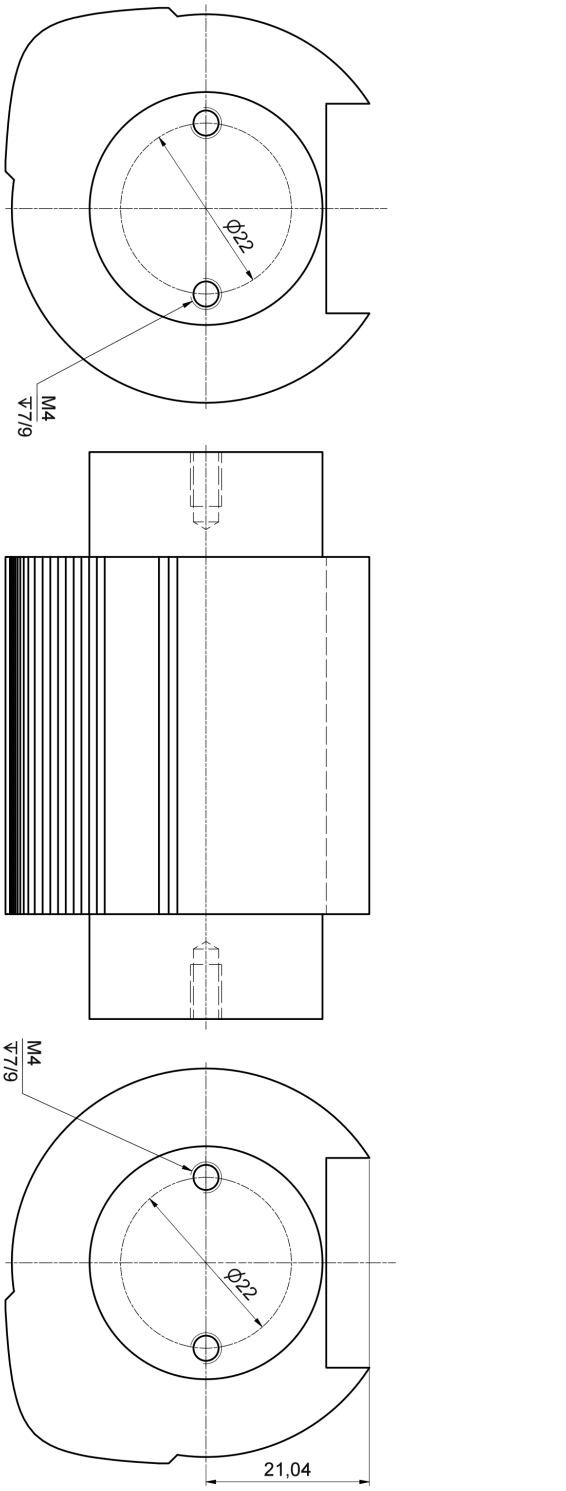
Periodic Quadrupole-Drawings



Dateipfad: C:\Arbeitsbereich\CAD\Konstruktion\2022\TEC-2022-13-Periodic quadrupole\TEC-0000184.ipt

Zul. Abweichung: ISO 2768 mittel		 Technik Haus Karlsruhe Institut für Technologie	TEC		Maßstab: 1 : 1	Anzahl:
					Werkstoff: S355JR	Gewicht: 0,822 kg
				Benennung: Stahl-Grundkörper		
				Tec-Auftrag / Institut: 4107313 -		
				Zeichnungs-Nr. / Revision: TEC-0000184-A		
				1		
				A4		
Rev.	Grund	Datum	Name	Projektionsmethode 1		

Für diese Zeichnung behalten wir uns alle Rechte vor. Nach der Freigabe der Zeichnung durch den Zeichner ist die Zeichnung für die Fertigung freigegeben. Die Fertigung ist für die Fertigung freigegeben. Die Fertigung ist für die Fertigung freigegeben.



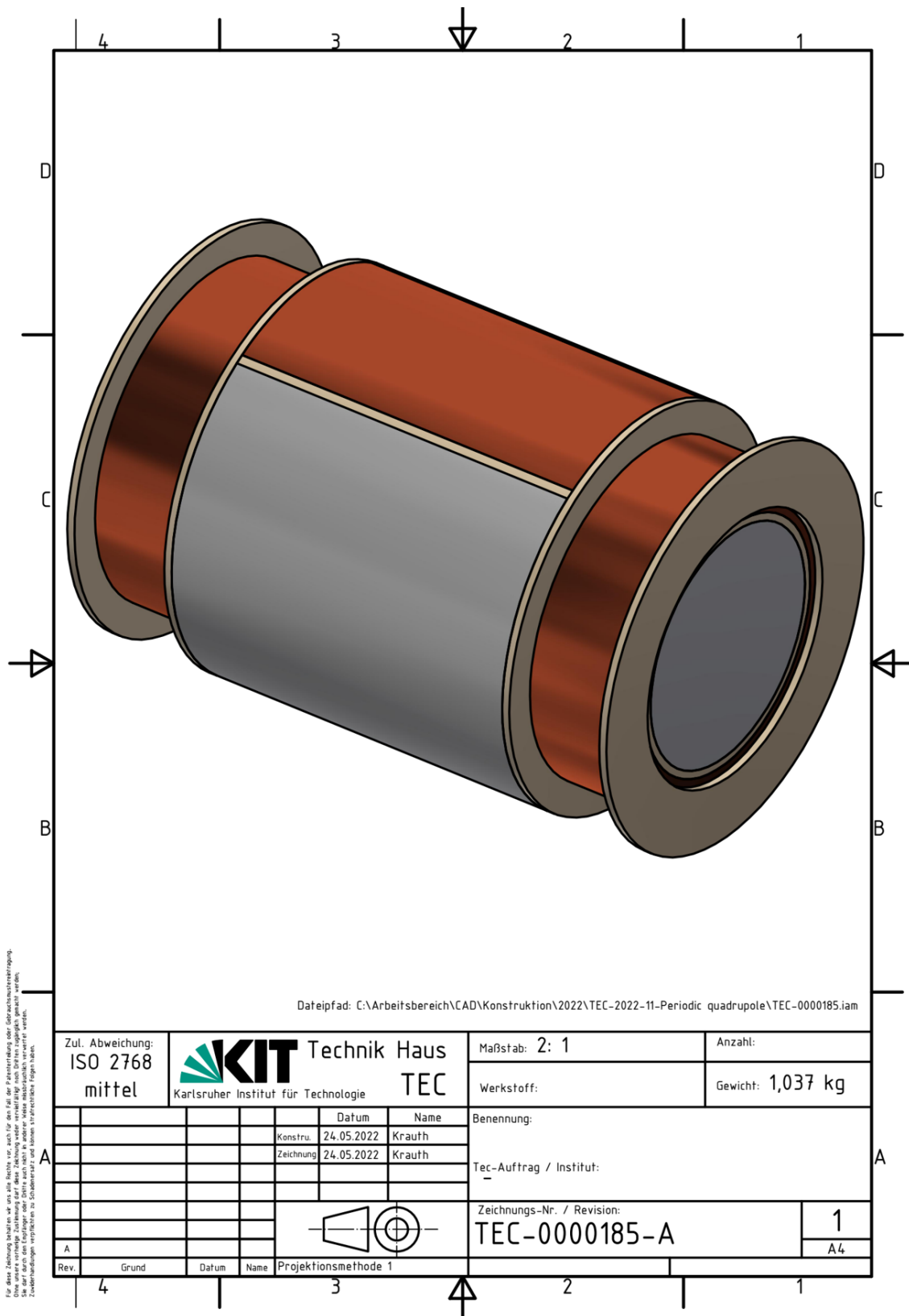
Nacharbeit

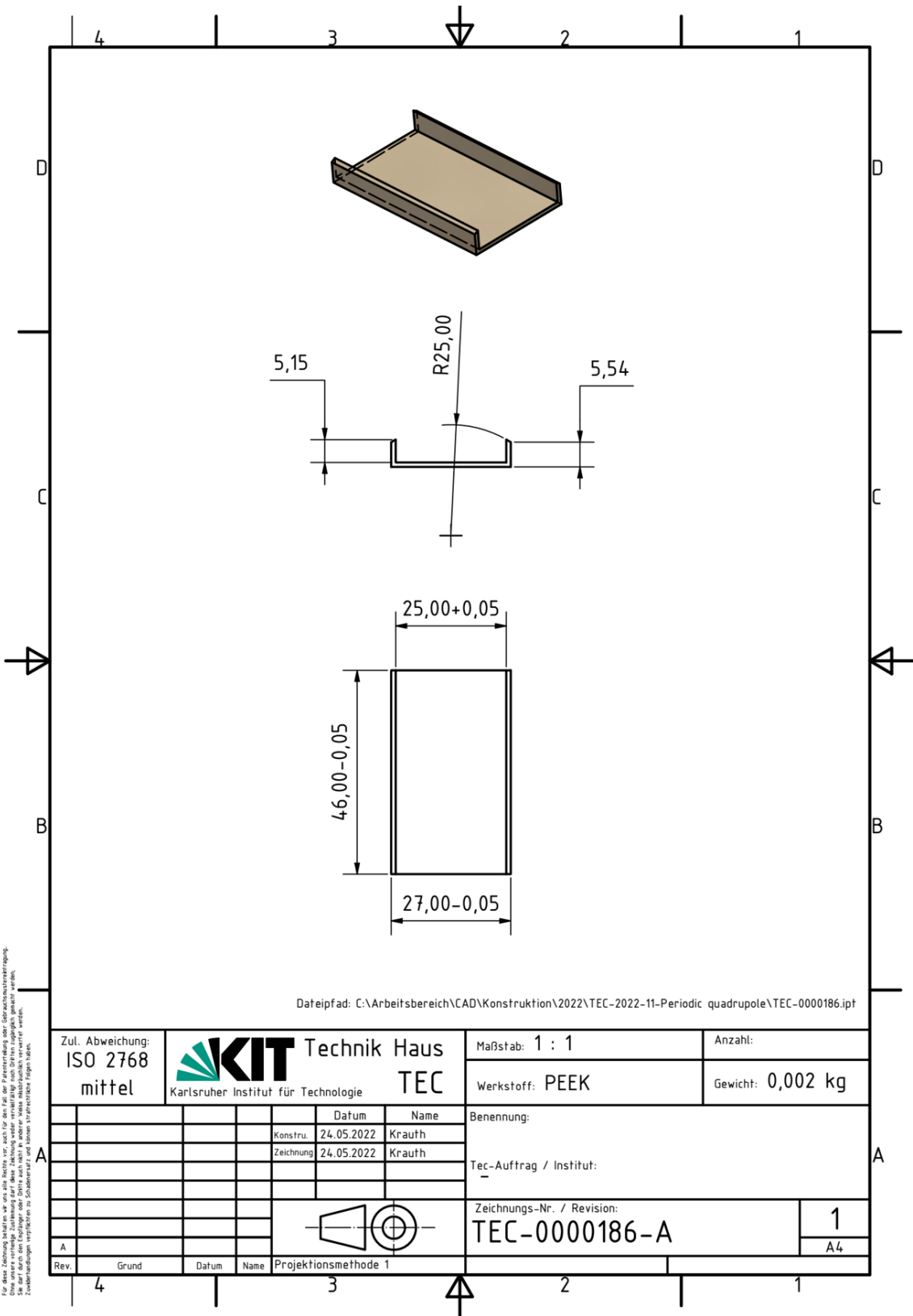
Zustellungswahl	Zustellungswahl	Zustellungswahl	Zustellungswahl	Zustellungswahl	Zustellungswahl	Zustellungswahl	Zustellungswahl	Zustellungswahl	Zustellungswahl	Zustellungswahl	Zustellungswahl
aktuell	aktuell	aktuell	aktuell	aktuell	aktuell	aktuell	aktuell	aktuell	aktuell	aktuell	aktuell
Messstab	Messstab	Messstab	Messstab	Messstab	Messstab	Messstab	Messstab	Messstab	Messstab	Messstab	Messstab
2:1	2:1	2:1	2:1	2:1	2:1	2:1	2:1	2:1	2:1	2:1	2:1
Zust.	Anordnung	Datum	Name	Werkstoff	Tap	Name	Zeichnungs-Nr.	<p>KT Karlsruher Institut für Technologie Institut für Technische Physik</p> <p>Eisenjoch Periodic quadrupole</p> <p>ITEP_205783_3</p>			
								<p>Sonderprojekte / Periodic quadrupole / 205783</p>			
								<p>Auflage</p>			

Für diese Zeichnung bestehen wir aus Holz oder aus Holzwerkstoffen, welche unter der Aufsicht einer geeigneten Person gefertigt wurden. Wir übernehmen keine Haftung für Schäden oder Verluste, die aus dem Gebrauch dieser Zeichnung resultieren. Diese Zeichnung wurde mit AutoCAD erstellt.


Musterdruck KRUMHÖR 25.10.2022 - 11:16 - EISJE

A. Appendix



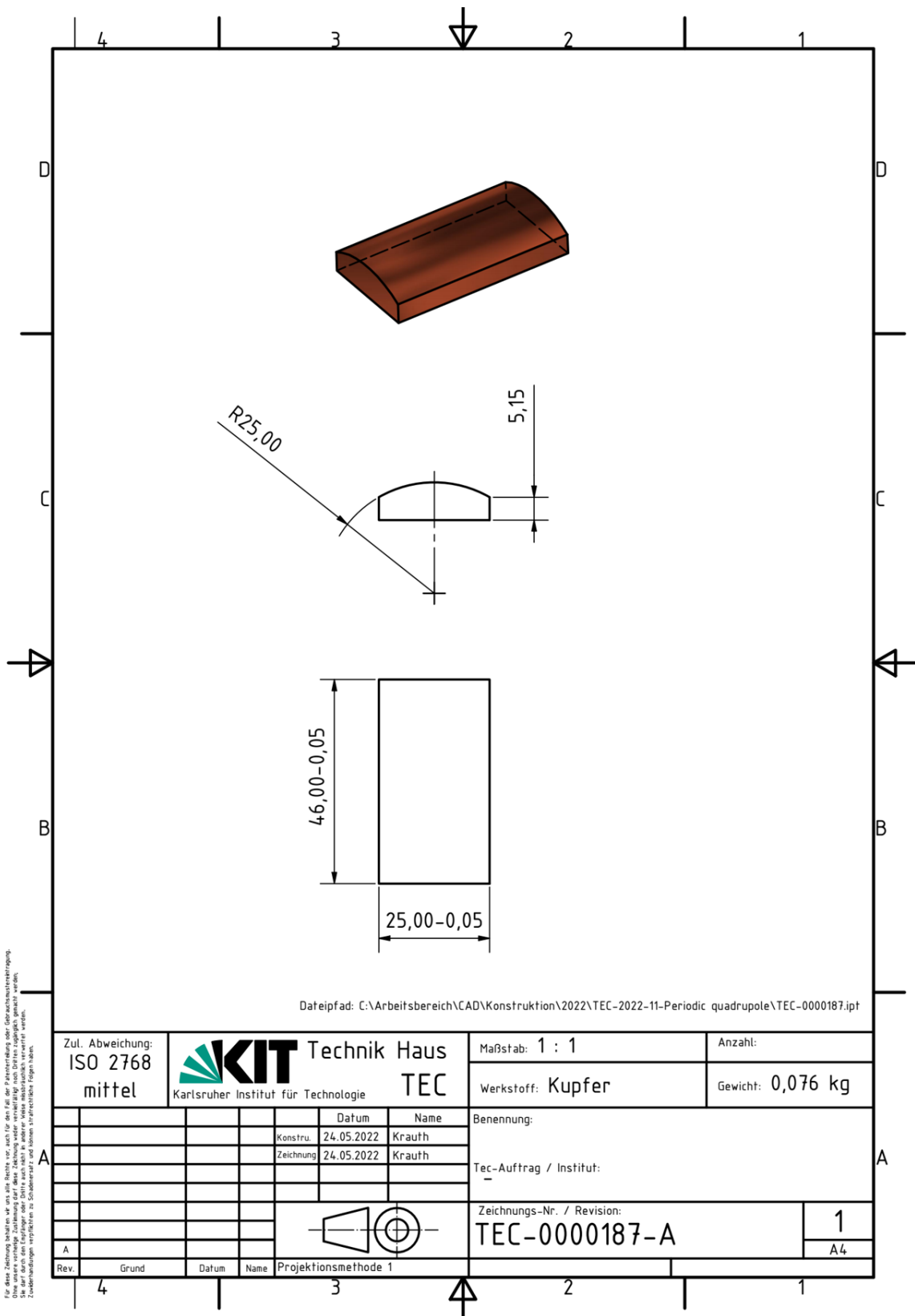


Dateipfad: C:\Arbeitsbereich\CAD\Konstruktion\2022\TEC-2022-11-Periodic quadrupole\TEC-0000186.ipt

Zul. Abweichung: ISO 2768 mittel		 Technik Haus TEC Karlsruher Institut für Technologie	Maßstab: 1 : 1	Anzahl:
			Werkstoff: PEEK	Gewicht: 0,002 kg
		Datum	Name	
		Konstru.	24.05.2022 Krauth	
		Zeichnung	24.05.2022 Krauth	
		Benennung:		
		Tec-Auftrag / Institut:		
		Zeichnungs-Nr. / Revision:		
		TEC-0000186-A		1
				A4
Rev.	Grund	Datum	Name	Projektionsmethode 1



Für diese Zeichnung gelten die Regeln der ISO 2768-mittel. Die Fertigungstoleranzen sind in der Zeichnung angegeben. Die Fertigungstoleranzen sind in der Zeichnung angegeben. Die Fertigungstoleranzen sind in der Zeichnung angegeben.

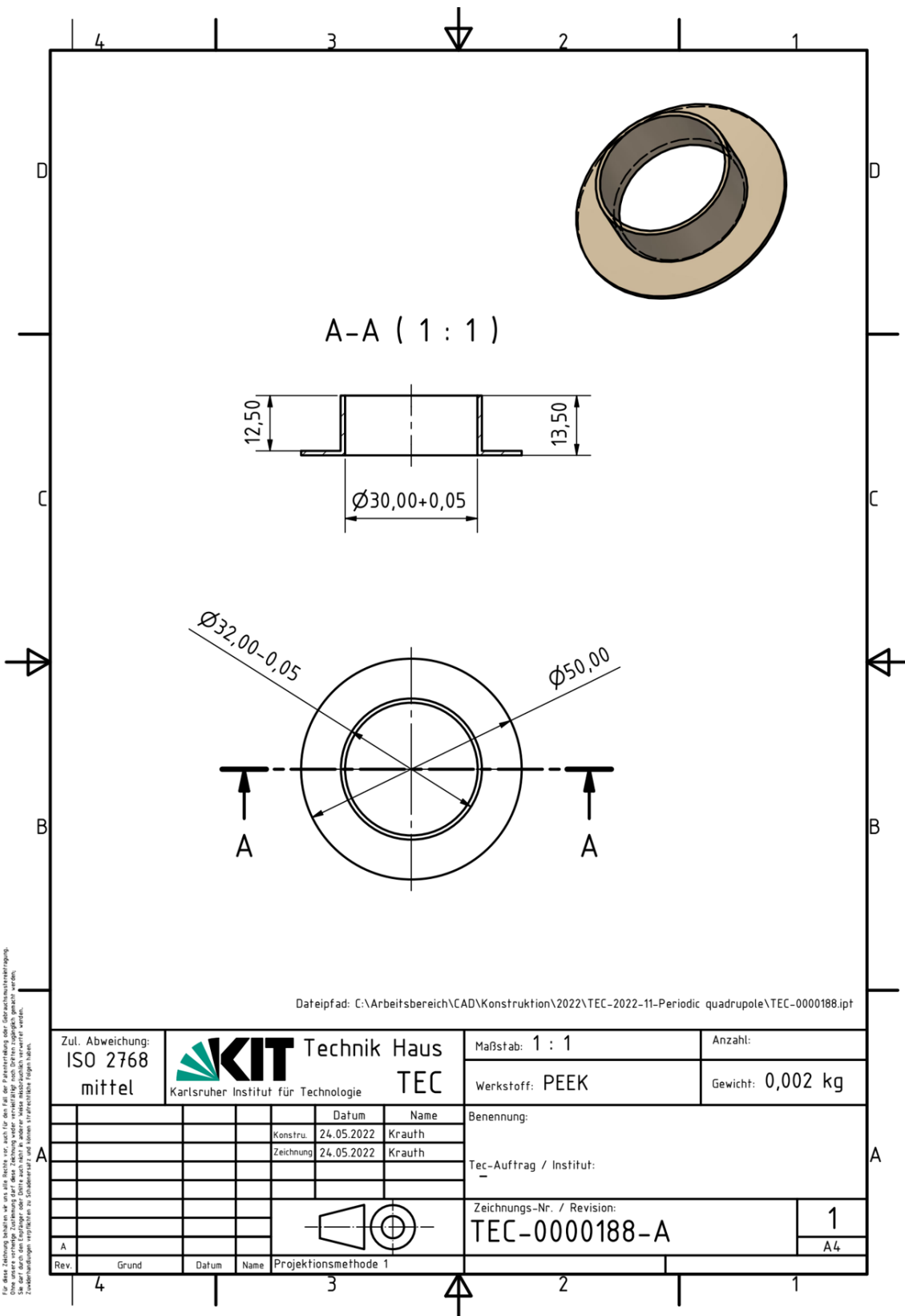
A. Appendix



Dateipfad: C:\Arbeitsbereich\CAD\Konstruktion\2022\TEC-2022-11-Periodic quadrupole\TEC-0000187.ipt


Für diese Zeichnung gelten die Regeln der Projektionsmethode 1 (1. Blickwinkel).
 Eine entsprechende Zeichnung darf diese Zeichnung nicht ersetzen.
 Die Zeichnung ist nur für den Zweck der Darstellung der Form und der Dimensionen zu verwenden.
 Sie darf nicht für die Fertigung oder die Montage verwendet werden.
 Änderungen sind nur durch eine Änderung der Zeichnung möglich.

Zul. Abweichung: ISO 2768 mittel		 Technik Haus TEC Karlsruher Institut für Technologie	Maßstab: 1 : 1		Anzahl:
			Werkstoff: Kupfer		Gewicht: 0,076 kg
		Datum Name Konstru. 24.05.2022 Krauth Zeichnung 24.05.2022 Krauth		Benennung:	
				Tec-Auftrag / Institut:	
		 Projektionsmethode 1		Zeichnungs-Nr. / Revision:	
				TEC-0000187-A	
Rev.	Grund	Datum	Name		

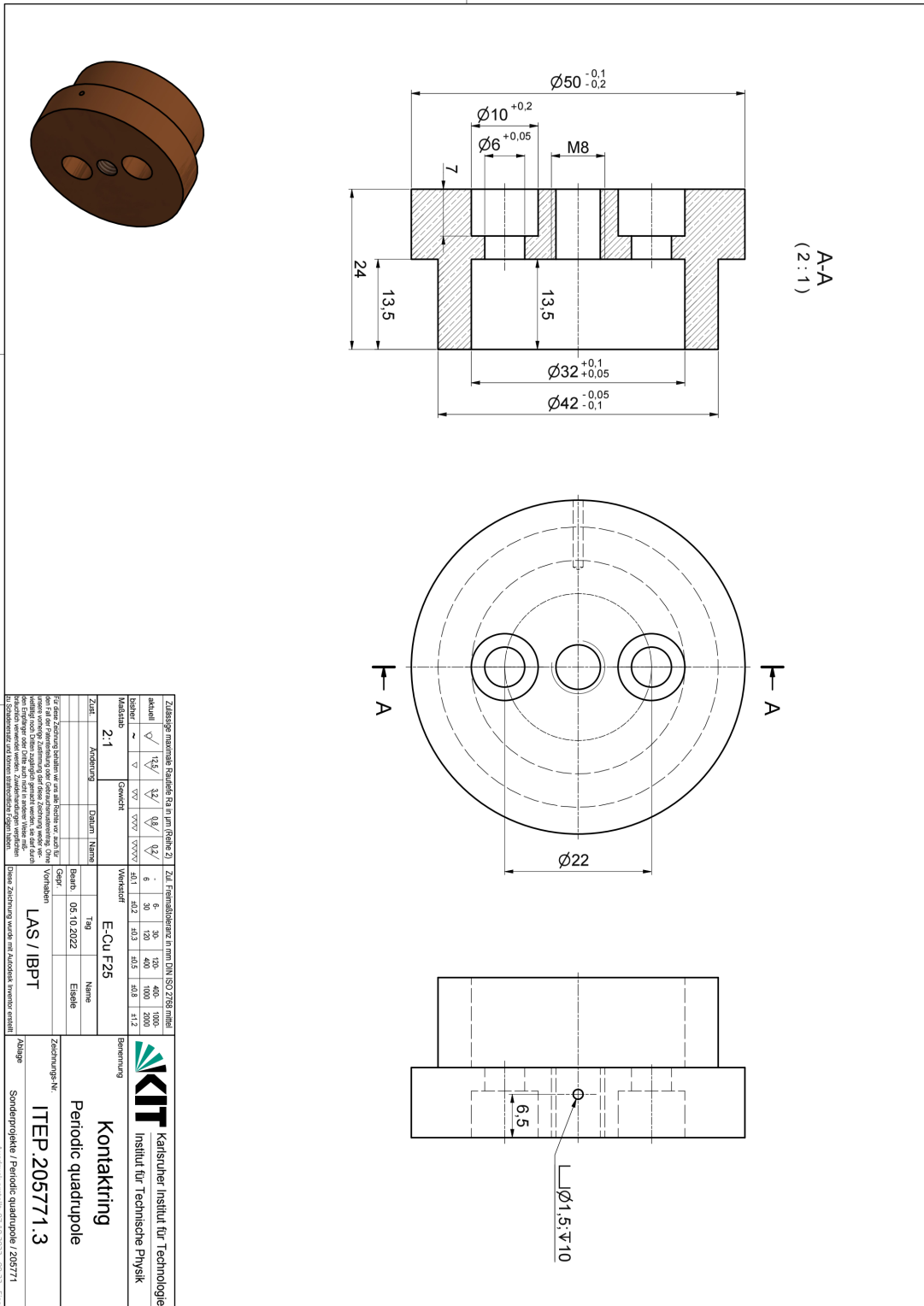


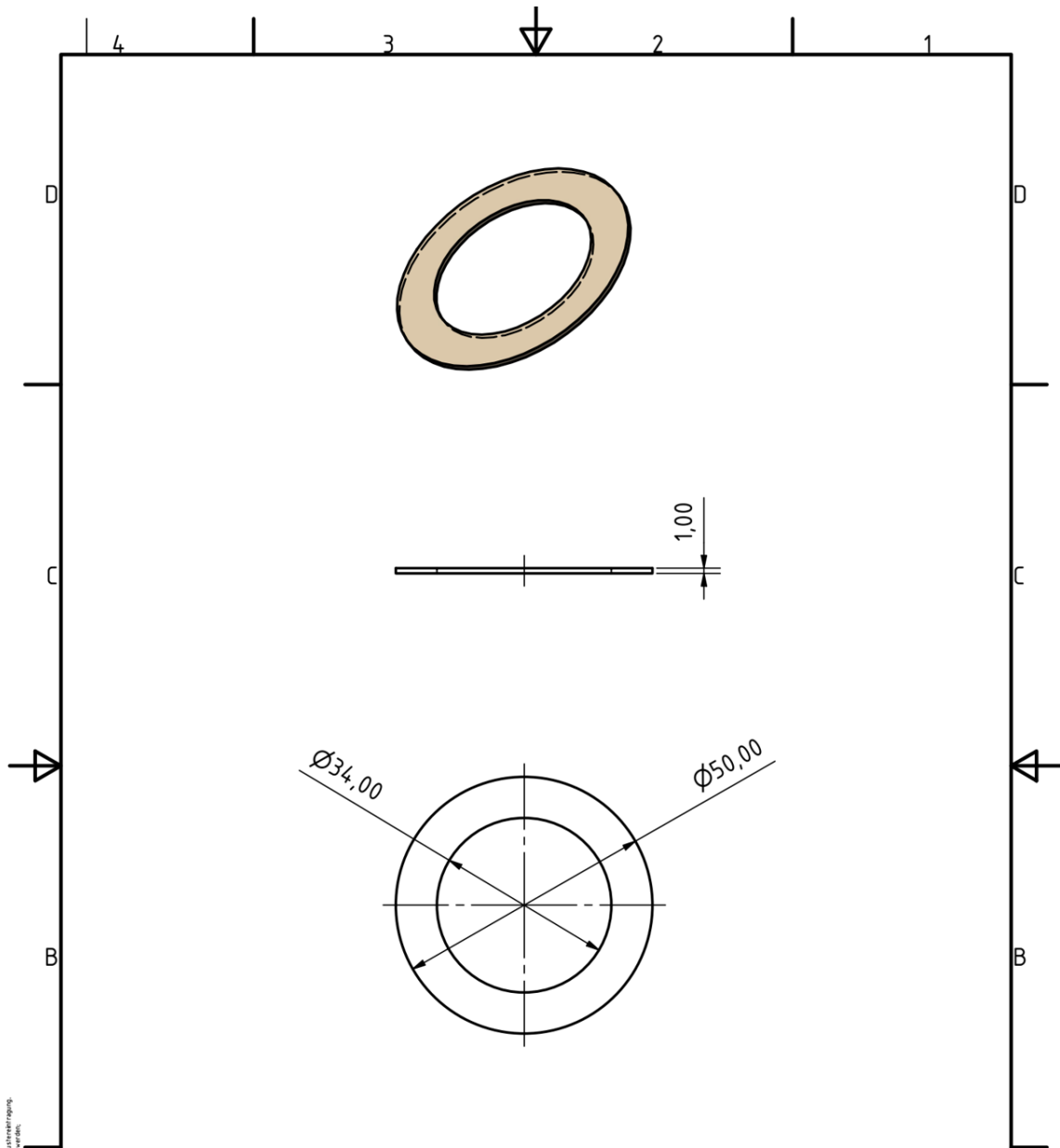
Dateipfad: C:\Arbeitsbereich\CAD\Konstruktion\2022\TEC-2022-11-Periodic quadrupole\TEC-0000188.ipt

Für diese Zeichnung behalten wir uns alle Rechte vor, auch für den Fall der Patentverletzung oder Gebrauchsmachungsverletzung.
 Diese unsere vorstehende Zustimmung darf diese Zeichnung weder vervielfältigt noch Dritten zugänglich gemacht werden.
 Zuwiderhandlungen verpflichten zu Schadenersatz und können strafrechtliche Folgen haben.

Zul. Abweichung: ISO 2768 mittel		 Technik Haus TEC Karlsruher Institut für Technologie	Maßstab: 1 : 1	Anzahl:									
			Werkstoff: PEEK	Gewicht: 0,002 kg									
		<table border="1"> <thead> <tr> <th></th> <th>Datum</th> <th>Name</th> </tr> </thead> <tbody> <tr> <td>Konstru.</td> <td>24.05.2022</td> <td>Krauth</td> </tr> <tr> <td>Zeichnung</td> <td>24.05.2022</td> <td>Krauth</td> </tr> </tbody> </table>		Datum	Name	Konstru.	24.05.2022	Krauth	Zeichnung	24.05.2022	Krauth	Benennung:	
	Datum	Name											
Konstru.	24.05.2022	Krauth											
Zeichnung	24.05.2022	Krauth											
			Tec-Auftrag / Institut:										
			Zeichnungs-Nr. / Revision:										
			TEC-0000188-A										
			1										
			A4										
Rev.	Grund	Datum	Name	Projektionsmethode 1									






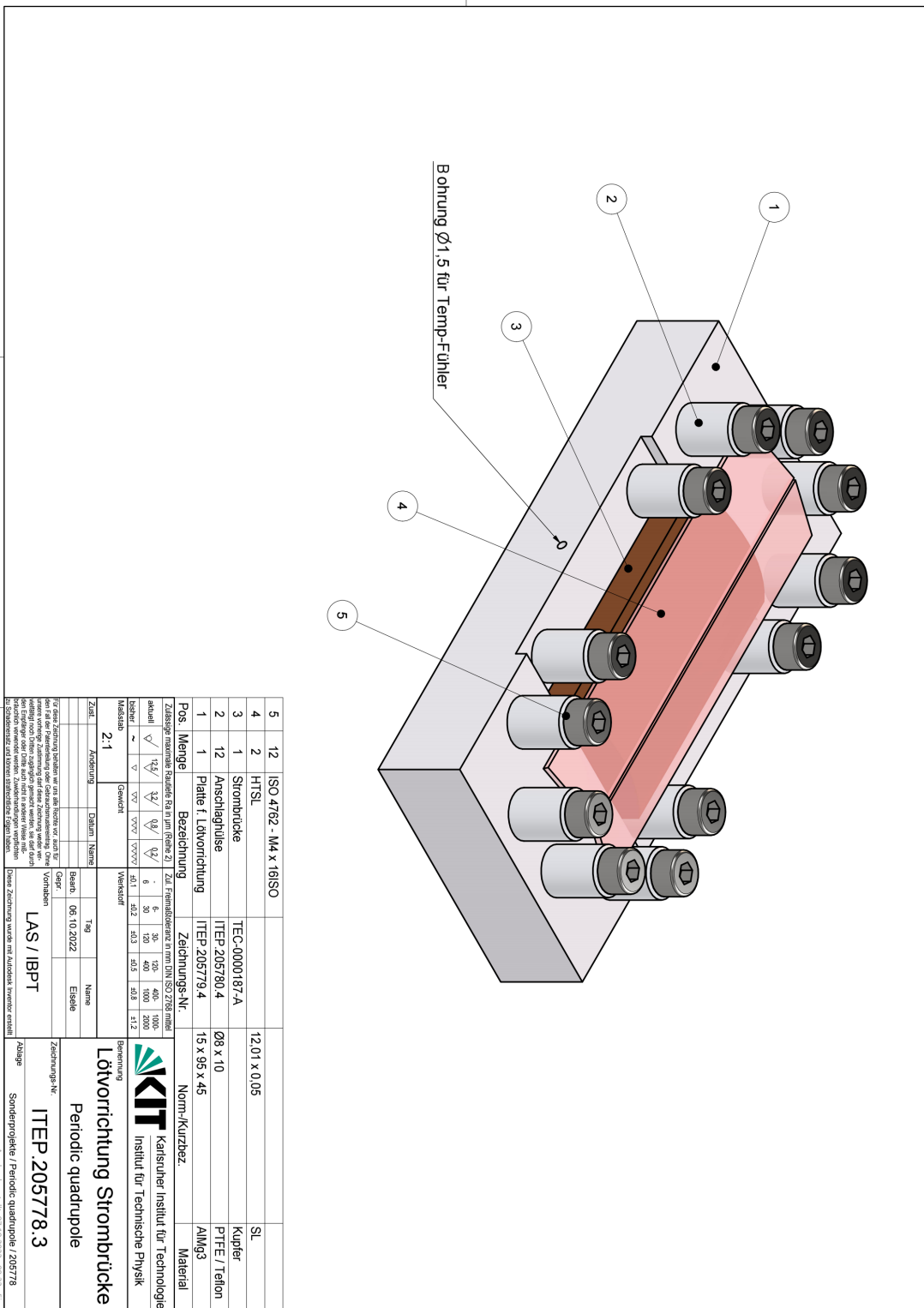


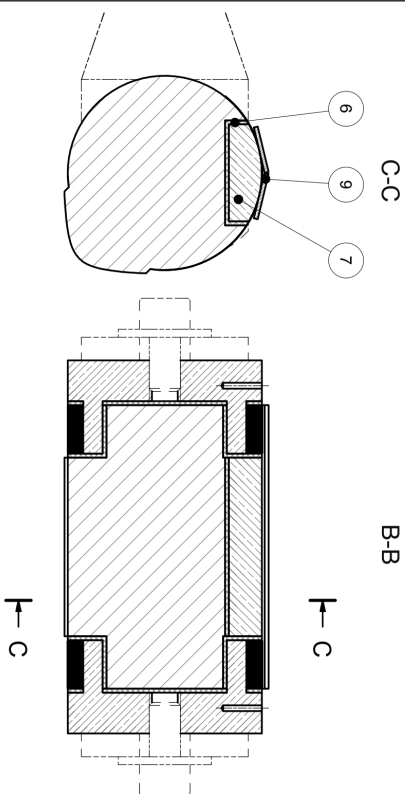
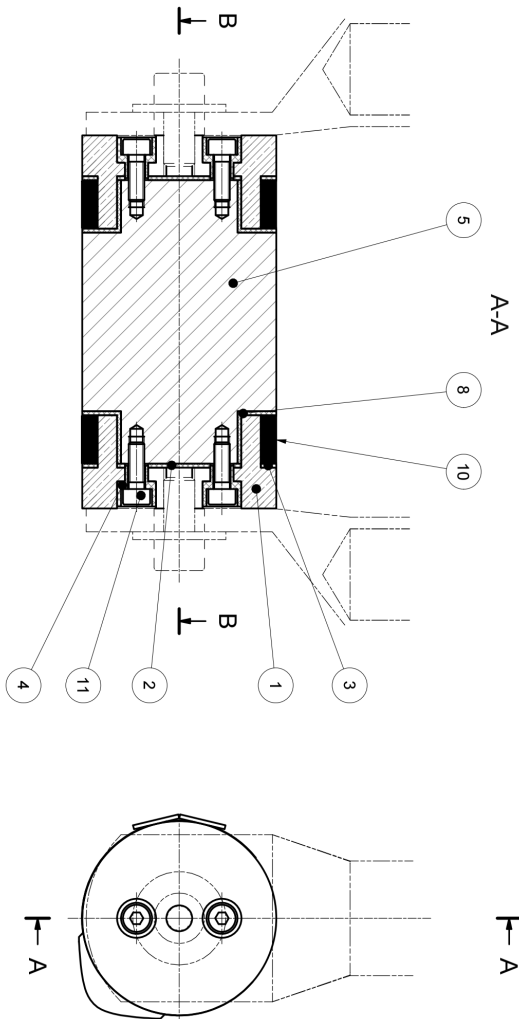
Dateipfad: C:\Arbeitsbereich\CAD\Konstruktion\2022\TEC-2022-11-Periodic quadrupole\TEC-0000190.ipt

Für diese Zeichnung behält sie alle Rechte vor, auch für den Fall der Patentverletzung oder Gebrauchstreueverletzung.
 Sie darf nicht ohne schriftliche Genehmigung des Karlsruher Instituts für Technologie (KIT) weitergegeben werden.
 Sie darf nicht zum Kopieren oder Zitieren in anderen Medien (einschließlich elektronischer Medien) verwendet werden.
 Zweifelsfälle sind dem Institut für Technologie (KIT) zu melden.

Zul. Abweichung: ISO 2768 mittel		 Technik Haus TEC Karlsruher Institut für Technologie	Maßstab: 1 : 1	Anzahl:
			Werkstoff: PEEK	Gewicht: 0,001 kg
		Benennung: Tec-Auftrag / Institut:		
		Zeichnungs-Nr. / Revision: TEC-0000190-A		1
A	Rev.	Grund	Datum	Name
				Projektionsmethode 1







Wickel- und Lötprozess siehe PowerPoint-Folien OFF-000203.pptx

Pos.	Menge	Bezeichnung	Zeichnungs-Nr.	Material
11	4	ISO 4762 - M4 x 12ISO		SL
10	2	HTSL Wicklung	12.01 x 0.065 - 73 Wdg.	SL
9	2	HTSL	12.01 x 0.065	SL
8	2	Isolierteil	TEC-0000188-A	PEEK
7	1	Strombrücke	TEC-0000187-A	Kupfer
6	1	Isolierung Strombrücke	TEC-0000186-A	PEEK
5	1	Eisenloch	ITEP 205783.3	S235 JR
4	4	Isolierhülse	ITEP 205774.4	PEEK
3	2	Isolierscheibe	ITEP 205773.4	PEEK
2	2	Isolierscheibe	ITEP 205772.4	PEEK
1	2	Kontaktring	ITEP 205771.3	E-Cu F25

Zust.	Änderung	Datum	Name
1	1		

Zust.	Änderung	Datum	Name
1	1		

Zust.	Änderung	Datum	Name
1	1		

Zust.	Änderung	Datum	Name
1	1		

Zust.	Änderung	Datum	Name
1	1		

Zust.	Änderung	Datum	Name
1	1		

Zust.	Änderung	Datum	Name
1	1		

Zust.	Änderung	Datum	Name
1	1		

Maschinenkennlinie: 12.10.2022 - 09:58 - E:\HW

B. Conference and publications

- 1] S. Fatehi, A. Bernhard and A. -S. Müller. "Miniature, High Strength Transport Line Design for Laser Plasma Accelerator-Driven FELs". In Proceedings of the 12th International Particle Accelerator Conference (IPAC21): Campinas, Brazil, pp. 561-563, (2021).
- 2] S. Fatehi, M. Ning, A. Bernhard, K. Damminsek, and A. -S. Müller. "Miniature transport-line design and experimental investigations of the superconducting transverse gradient undulator source for laser-plasma accelerator-driven FELs". DPG-Frühjahrstagungen, Dortmund, Germany, (2021).
- 3] G. D'Auria, N. Thompson, J. Clarke, S. Fatehi, A. Bernhard et al. "XLS - Conceptual Design Report of the CompactLight X-ray FEL (Version v1)". Zenodo, (2021). <https://doi.org/10.5281/zenodo.6375645>
- 4] F. Nguyen, M. Carpanese, A. Petralia, A. Bernhard, J. Arnsberg, S. Fatehi, J. Gethmann, S. Grohmann et al. "Undulators and Light Production with the XLS-CompactLight Design Study". Moscow University Physics Bulletin, 77 (2), pp. 241–244, (2022). <https://doi.org/10.3103/S0027134922020710>
- 5] M. Ning, S. Fatehi, A. Bernhard, R. Rossmanith and A. -S. Müller. "A new beam transport line for transverse gradient undulator at JETI in Jena". DPG-Frühjahrstagungen, Mainz, Germany, (2022).
- 6] S. Fatehi, A. Bernhard and A. -S. Müller. "A Miniature Transport-line Design for Laser Plasma accelerator-driven FELs using HTS Magnets". DPG-Frühjahrstagungen, Mainz, Germany, (2022).
- 7] S. Fatehi, A. Bernhard, S. C. Richter, M. Eisele, F. Hornung, T. Arndt, A.-S. Müller. "Validating a HTS miniature, periodic quadrupole driving a short-length transport line for laser-plasma accelerators". Applied Superconductivity Conference (ASC22), (2022).
- 8] S. Fatehi, A. Bernhard and A. -S. Müller. "A short-length transport line for laser-plasma accelerators using HTS periodic magnets". To be published in Proceedings of the 14th International Particle Accelerator Conference (IPAC2023): Venice, Italy, (2023).

9] M. Ning, S. Fatehi, A. Bernhard, A. -S. Müller." Design, fabrication, and measurement of a normal conducting quadrupole for a laser-plasma accelerator-based beam transport line". To be published in Proceedings of the 14th International Particle Accelerator Conference (IPAC2023): Venice, Italy, (2023).

10] M. Ning, S. Fatehi, A. Bernhard, A-S. Müller, "Scaling fixed-field alternating gradient-type magnets for transportation of laser-plasma accelerator electron beams". To be published in Proceedings of the 14th International Particle Accelerator Conference (IPAC2023): Venice, Italy, (2023).

C. Supervised Master Thesis

1] M. Ning. "A new transport line for transverse gradient undulator experiments at the JETI laser-plasma accelerator in Jena". Master thesis, Karlsruhe Institute of Technology (KIT), (2021).